JAGIELLONIAN UNIVERSITY
MARIAN SMOLUCHOWSKI INSTITUTE OF PHYSICS
NUCLEAR PHYSICS DEPARTMENT

Ph.D. Thesis

**The Neutron Electric Dipole Moment Experiment:
Research and Development for the New Spectrometer**

MARCIN KUŹNIAK

Promotor:
prof. dr hab. Kazimierz Bodek

Kraków, 2008

Abstract

This work describes the search for novel storage materials towards an improved neutron electric dipole moment experiment (nEDM) and the measurement of neutron - mirror neutron oscillations.

A measurement of the nEDM, using Ramsey's method of separated oscillatory fields, is in preparation at the new high intensity source of ultracold neutrons (UCN) at the Paul Scherrer Institute, Villigen, Switzerland (PSI). The existence of a non-zero nEDM result would violate both parity and time reversal symmetry and, given the CPT theorem, might lead to the discovery of new CP violating mechanisms. Already the current upper limit for the nEDM ($|d_n| < 2.9 \times 10^{-26}\,e\,\mathrm{cm}$) constrains some extensions of the Standard Model.

Experiments using UCN stored in traps also provide the possibility of searching the neutron - mirror neutron oscillations and, thus, testing the mirror matter hypothesis. The first direct measurement investigating that phenomena was performed at the Institut Laue-Langevin (ILL) and a lower limit for the neutron - mirror neutron oscillation time was obtained, $\tau_{\mathrm{nn'}} > 103\,\mathrm{s}$ (95% C.L.).

Presently, both type of experiments are limited mostly by statistics, therefore increasing the number of neutrons available, becomes of much interest. The nEDM experiment at PSI aims at a two orders of magnitude reduction of the experimental uncertainty, to be achieved mainly by (1) the higher UCN flux provided by the new PSI source and better storage materials, (2) better control over systematic effects. The Monte Carlo simulations performed in this work show that moving the existing nEDM apparatus equipped with a quartz UCN trap from the ILL, where it is located, to the new PSI source will result in a factor of $\sim$20 gain in UCN counts and another factor of 1.5, when a material with a Fermi potential similar to deuterated polystyrene (DPS, $V_F \approx 162\,\mathrm{neV}$) is used instead of quartz ($V_F \approx 90\,\mathrm{neV}$).

High electrical resistivity and dielectric strength are additionally required for the storage chamber wall material, in order to reach maximum HV operation. After an extensive experimental study including several other materials (e.g. Si_3N_4 and diamond), polystyrene was selected as the best insulator material, while DPS and deuterated polyethylene (DPE) turned out to be suitable for its UCN-reflecting inner coating. The measured values for the Fermi potentials are $161 \pm 10\,\mathrm{neV}$ for DPS and $214 \pm 10\,\mathrm{neV}$ for DPE. The new chamber was produced and successfully tested in the nEDM apparatus at ILL, yielding about 50% gain in the number of UCN, as compared to the quartz chamber, which had been used so far.

Streszczenie

Celem niniejszej pracy jest wybór nowych materiałów do wykorzystania w eksperymencie mierzącym elektryczny moment dipolowy neutronu (nEDM) oraz w pomiarach oscylacji neutron - neutron lustrzany.

W Instytucie Paula Scherrera (PSI, Villigen, Szwajcaria), przy nowym intensywnym źródle ultra-zimnych neutronów (UCN), przygotowywany jest pomiar elektrycznego momentu dipolowego neutronu metodą odseparowanych oscylujących pól Ramsey'a. Zmierzenie niezerowej wartości nEDM wskazywałoby na łamanie fundamentalnych symetrii $\mathcal{P}$ i $\mathcal{T}$ oraz, zakładając zachowanie $\mathcal{CPT}$, byłoby równoznaczne z odkryciem nieznanego dotychczas mechanizmu łamania $\mathcal{CP}$. Już obecnie doświadczalna górna granica na nEDM ($|d_n| < 2.9 \times 10^{-26}\, e\,\mathrm{cm}$) wyklucza niektóre z rozszerzeń Modelu Standardowego (SM).

Eksperymenty polegające na pułapkowaniu UCN pozwalają również na poszukiwanie oscylacji neutron - neutron lustrzany i tym samym na doświadczalne sprawdzenie hipotezy o istnieniu materii lustrzanej. Pierwszy bezpośredni pomiar tego rodzaju został przeprowadzony w Instytucie Laue-Langevin (ILL, Grenoble, Francja) dostarczając dolnej granicy na czas oscylacji neutron - neutron lustrzany, $\tau_{\mathrm{nn'}} > 103\,\mathrm{s}$ (95% C.L.).

W chwili obecnej dokładność obu eksperymentów jest ograniczona przez błędy statystyczne, pożądane jest zatem istotne zwiększenie ilości rejestrowanych zdarzeń. Celem eksperymentu w PSI jest poprawienie dokładności o dwa rzędy wielkości, co zostanie osiągnięte dzięki (1) wyższemu strumieniowi neutronów dostarczanych przez nowe źródło w PSI, (2) użyciu materiałów o lepszych właściwościach oraz (3) większej kontroli nad efektami systematycznymi. Symulacje Monte Carlo zaprezentowane w pracy wskazują, że przeniesienie istniejącego spektrometru nEDM, wyposażonego w kwarcową ($V_F \approx 90\,\mathrm{neV}$) pułapkę UCN, z ILL – gdzie się on obecnie znajduje – do nowego źródła w PSI zaowocuje 20-krotnym zwiększeniem ilości zliczeń. Dodatkowy czynnik, około 1.5, zostanie uzyskany jeśli zamiast kwarcu zastosowany będzie materiał o potencjale Fermiego zbliżonym do deuterowanego polistyrenu (DPS, $V_F \approx 162\,\mathrm{neV}$).

Aby osiągnąć niezbędną w eksperymencie wartość pola elektrycznego, dodatkowo wymagana jest wysoka oporność i wytrzymałość na przebicie elektryczne ściany komory, w której przechowywane są neutrony. W efekcie rozbudowanego doświadczalnego studium porównawczego, uwzględniającego m.in. Si_3N_4 i diament, jako najlepszy materiał na komorę (izolator) wybrano polistyren, podczas gdy DPS i deuterowany polietylen (DPE) okazały się najlepszymi kandydatami na jej wewnętrzną, odbijającą UCN powłokę. Zmierzony został potencjał Fermiego obu materiałów: $161 \pm 10\,\mathrm{neV}$ dla DPS i $214 \pm 10\,\mathrm{neV}$ dla DPE. Ostatecznie, nowa komora UCN została wykonana i przetestowana. Osiągnięto sukces, uzyskując w spektrometrze nEDM w ILL o 50% więcej UCN niż z używaną dotychczas komorą kwarcową.

Contents

List of Symbols

$\mathcal{V}$ Volume

η UCN loss probability per wall reflection

γ Gyromagnetic ratio

μ Magnetic permeability

$\mu(E)$ Energy dependent UCN loss probability

μ_A Reduced mass for the neutron – nucleus system

μ_n Neutron magnetic dipole moment

ν Frequency

ω Angular frequency

ρ (Volume) resistivity

ρ_s Surface resistivity

σ Total cross section

$\tau_{\mathrm{nn'}}$ Neutron - mirror neutron oscillation time

θ_{EB} Angle between electric and magnetic field vectors

ε Dielectric constant

ϱ Density

a Scattering length

b Bound coherent scattering length

C Capacitance

d_n Neutron Electric Dipole Moment

E Kinetic energy

F Force

g	Earth's gravitational acceleration
H	Height
$h, \hbar$	Planck's constant
I	Current
l	Length
M	Molar mass
m_n	Neutron mass
N	Scattering center density
N_A	Avogadro constant
R	Electrical resistance
S, A	Area
T	Temperature
t_f	Free UCN flight time between two wall collisions
U	Voltage
U_{br}	Breakdown voltage
U_{fl}	Flashover voltage
V	Potential energy
V_F	Fermi pseudo-potential
v_F	Critical velocity
V_g	Gravitational potential
$\mathbf{B}$	Magnetic field
$\mathbf{E}$	Electric field
$\mathbf{S}$	Spin

List of Acronyms

BAU Baryon Asymmetry of the Universe

BOE Buffer Oxide Etcher

CKM Cabibbo-Kobayashi-Maskawa (matrix)

CNR Cold Neutron Reflectometry

CTE Coefficient of Thermal Expansion

CVD Chemical Vapour Deposition

DAQ Data Aquisition

DC Direct Current

DLC Diamond-like Carbon

DPE Deuterated Polyethylene

DPS Deuterated Polystyrene

EELS Electron Energy Loss Spectroscopy

EDM Electric Dipole Moment

EDX Energy Dispersive X-Ray Spectroscopy

ERDA Elastic Recoil Detection Analysis

ETH Eidgenössische Technische Hochschule

FEM Finite Elements Method

GID Grazing Incidence X-Ray Diffraction

GZK Greisen-Zatespin-Kuzmin (cutoff)

HDPE High Density Polyethylene

HFCVD Hot Filament Chemical Vapour Deposition

HV High Voltage

ILL Institut Laue-Langevin

IPA Isopropanol

LDPE Low Density Polyethylene

MWCVD Microwave Chemical Vapour Deposition

MSSM Minimal Supersymmetric Standard Model

nEDM Neutron Electric Dipole Moment

ORNL Oak Ridge National Laboratory

PC Polycarbonat

PE Polyethylene

PMMA Polymethyl methacrylate

PMT Photomultiplier tube

PNPI Petersburg Nuclear Physics Institute

PSI Paul Scherrer Institut

PS Polystyrene

PTFE Polytetrafluoroethylene

PVC Polyvinyl Chloride

QCD Quantum Chromodynamics

RAL Rutherford Appleton Laboratory

RF Radio Frequency

SEM Scanning Electron Microscopy

SM Standard Model

SNS Spallation Neutron Source

SS Stainless Steel

TEM Transmission Electron Microscopy

UCN Ultracold Neutron

UHCR Ultra-High Energy Cosmic Rays

UVFS Ultraviolet Grade Fused Silica

UV Ultraviolet (light)

VCN Very Cold Neutron

WIMP Weakly Interacting Massive Particle

XRD X-Ray Diffraction

Chapter 1

Introduction

The main focus of this work was the search for novel materials for the storage of ultracold neutrons (UCN) in the context of the new generation neutron electric dipole moment experiment (nEDM) and the measurement of neutron - mirror neutron (nn') oscillations. Both experiments test fundamental symmetries of nature.

In terms of neutron storage, the most important material properties are the Fermi potential and the loss probability per wall reflection. In addition, due to specific features of the setup, the materials investigated had to show some additional properties, such as e.g. high electrical resistivity, good high-voltage performance, non-magnetic character and compatibility with other subsystems of the experimental apparatus.

After a brief theoretical introduction regarding fundamental properties of the neutron and its interaction with matter, simulations are presented, which optimize the material selection and the geometrical configuration for the nEDM apparatus.

Starting from this point, the practical aspect of the problem becomes the main scope of the thesis. Experimental techniques applied for the search of suitable materials and their theoretical background – when necessary – are described. Material tests and their results are discussed and, based on that, the final candidate for the storage chamber material is selected.

A new method to produce UCN reflecting deuterated polymer coatings is proposed and its succesful application for the storage of UCN is demonstrated. The coating technique is explained in detail in Sec. 5.4, together with the data, which has been obtained with the nEDM spectrometer using the new polymer coated storage chamber.

Finally, a physics result limiting the nn' oscillation time, obtained during test measurements, is presented.

1.1 Motivation

This work focusses on the nEDM experiment and on the nn' oscillation search. This type of research will greatly benefit from the new source of ultracold neutrons, which is being built at Paul Scherrer Institut (PSI) [1] and is expected to deliver $\sim 10^3\,\mathrm{UCN\cdot cm^{-3}}$ to the experiments. The up to two orders of magnitude improvement in the UCN density, as compared to the presently most intense source at the

Institut Laue-Langevin (ILL, Grenoble, France) [2], allows to substantially increase the experimental accuracy and to achieve interesting physics results. Naturally, this also applies to all other experiments which are currently limited by UCN statistics, e.g. the neutron lifetime measurement [3] and the determination of the correlation coefficients in β decay of free neutron [4].

1.1.1 Search for the neutron Electric Dipole Moment

Theoretical background   Although all the experiments conducted so far measured a value consistent with zero, there are still strong reasons to suspect that the neutron has a non-vanishing electric dipole moment, significantly larger than predicted by the Standard Model (SM).

In general, the existence of particles with an EDM would violate both parity ($\mathcal{P}$) and time reversal symmmetries ($\mathcal{T}$), as demonstrated in Fig. 1.1. Parity inverts the location of both electric charge centers, while time inversion changes the direction of the magnetic moment (and spin). The outcome differs from the initial state, which shows the violation of either symmetry. Some diatomic molecules like NaCl, HF
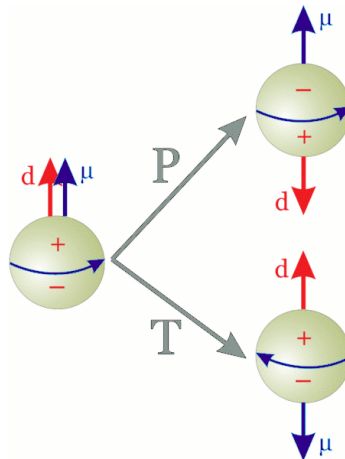

Figure 1.1: $\mathcal{P}$ and $\mathcal{T}$ violation. The dipole moments of a particle are shown, with a hypothetical non-zero electric dipole moment included. The states produced under the parity ($\mathcal{P}$) or the time reversal ($\mathcal{T}$) transformation are different from the initial state [5].

and CO show large EDMs, but as they are induced (the species have degenerate groundstates of opposite parity), they do not violate $\mathcal{P}$ and $\mathcal{T}$. So, the main object of the EDM search are elementary particles such as leptons (electrons [6], muons [7]), as well as are more complex objects like the neutron, proton [8] or even atoms (e.g. Hg [9]) and molecules. Measuring a non-zero value at a level above the SM expectation would be a clear sign of new physics.

Both mentioned symmetries plus additionally the charge conjugation symmetry $\mathcal{C}$ can be combined in the fundamental $\mathcal{CPT}$ symmetry. As formulated in the famous $\mathcal{CPT}$ theorem, all renormalizable quantum field theories conserve this symmetry [10].

Assuming $\mathcal{CPT}$ conservation, $\mathcal{T}$ violation is thus equivalent to $\mathcal{CP}$ violation. Contrary to the $\mathcal{P}$ violation, which is maximally violated in weak interaction, a tiny admixture of $\mathcal{CP}$ breaking processes has been so far observed only in decays of K^0 and B^0 mesons [11]. This mechanism was built into the SM with the δ_{KM} phase in the Cabibbo-Kobayashi-Maskawa (CKM) mixing matrix and tuned such that it explains the observed symmetry non-conservation. However, the SM does not give satisfactory answers to some questions, which probably require more $\mathcal{CP}$-odd processes.

Additional unknown sources of $\mathcal{CP}$ violation are of high interest as a possible explanation of one of the biggest puzzle in modern physics, the so called Baryon Asymmetry of the Universe (BAU). As known from astronomical observations, the baryons in the Universe are overwhelmingly matter and not anti-matter. It is impossible to explain this fact within the Standard Model and the standard model of cosmology. The observed BAU asymmetry, defined as the ratio of the difference between baryonic and anti-baryonic matter to radiation (the number of photons), $\eta_{\mathrm{BAU}} = (\eta_B - \eta_{\bar{B}})/\eta_\gamma$, is of the order of 10^{-10}, while the SM prediction is more than eight orders of magnitude lower. In other words, according to the SM, the excess of radiation over the baryonic matter should be so large, that stars and galaxies could not be even formed in the Universe. According to theoretical considerations, already at an early stage ($T \geq 40$ MeV) the universe possessed that asymmetry of unkown origin.

As suggested by Sakharov [12], a baryon asymmetry could dynamically arise from an initial state with baryon number equal zero if the following conditions hold: (i) baryon number non-conservation, (ii) both $\mathcal{C}$ and $\mathcal{CP}$ violating processes (iii) occuring in a non-equilibrium state at an early epoch. Discovery of the nEDM, as a clear indication of a new source of $\mathcal{CP}$ violation, could help to unravel the problem.

Another puzzling question is related to the so called *strong $\mathcal{CP}$ problem*. Experiments do not indicate any $\mathcal{CP}$ breaking in the strong sector of particle physics. However, the Lagrangian of quantum chromodynamics (QCD) contains a symmetry violating θ term, experimentally accessible via a derived parameter $\tilde{\theta}$. Since, there is is no clearly theoretically motivated limitations in QCD for the size of $\tilde{\theta}$, from naive dimensional analysis one would expect it to be not far from unity. This is not the case, as the present limit on the nEDM can be translated to $\tilde{\theta} < 10^{-10}$. Thus, the strong $\mathcal{CP}$ problem is why $\tilde{\theta}$ is so small. One usually arbitrarily assumes that fine-tuning of parameters leads to an extremely small effective value of this contribution, but despite several solutions proposed, the mystery remains unresolved. The most natural and accepted idea was proposed by Peccei and Quinn [13]. $\tilde{\theta}$ becomes here a pseudo-scalar dynamical field (not a parameter as before) and a new Goldstone boson, the axion, is required. There have been many searches for axion, but so far it has not been seen.

The most recent experimental result gives the nEDM upper limit of

$$|d_n| < 2.9 \times 10^{-26} e \cdot \mathrm{cm} \ \ [14],$$

which is almost five orders of magnitude above the value predicted by the SM, $|d_n| \sim 10^{-32} \, e \cdot \mathrm{cm}$ [15] , as derived from the $\mathcal{CP}$-odd phase in the CKM matrix (thus, from the electroweak sector). The strong contribution to the nEDM scales with the $\tilde{\theta}$
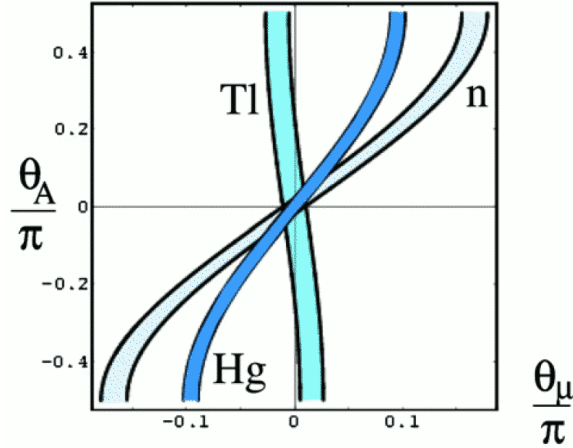
Figure 1.2: Constraints on the two $\mathcal{CP}$ violating phases for a given supersymmetric model from the experimental limits for the neutron, mercury and thallium EDM (from [18]).

angle, which is already many orders of magnitude below the naively expected value. Therefore it is hard to give any quantitative SM predictions on strong contributions to nEDM. In conclusion, search for the nEDM is not affected by any SM background and is directly sensitive to unknown sources of $\mathcal{CP}$ violation.

Interestingly, some theoretical extensions of the SM, including various types of supersymmetric models [16, 17] predict $|d_n|$ just "round the corner" in the range between 10^{-25} and $10^{-28}\,e\cdot\mathrm{cm}$. Supersymmetric models like MSSM, some of them additionaly adopting the discussed Peccei-Quinn mechanism, generally lead to new $\mathcal{CP}$-odd processes, either by a spontaneus symmetry breaking or by an intrinsic $\mathcal{CP}$ asymmetry of the theory. However, given the number of competing supersymmetric theories and the size of the parameter space (e.g. $\mathcal{CP}$-odd phases θ_A and θ_μ), it is not possible to give a more accurate prediction. In particular, it is also not feasible to derive a model-independent $|d_n|$ prediction from the observed Baryon Asymmetry. Typical, parameter-dependent and speculative predictions have the simplified form

$$d_n \sim \left(\frac{300\,\mathrm{GeV}}{M}\right)^2 \sin\phi \times 10^{-24}\,e\mathrm{cm}\,, \tag{1.1}$$

where M is the typical SUSY mass scale and ϕ is a combined $\mathcal{CP}$ violating phase. As with the strong $\mathcal{CP}$ problem, the current experimental limits require either the SUSY mass scale or the $\mathcal{CP}$ violating phase to be small, which leads to a brand-new *SUSY $\mathcal{CP}$ problem*. Figure 1.2 shows the constraints that the experimental limits from the neutron, mercury and thallium EDM pose on the two SUSY $\mathcal{CP}$ violating phases. Both phases are already constrained to be $< 10^{-2}$.

As explained, it is sufficiently theoretically motivated to expect a finite nEDM value, which can be reached by the next generation experiments, if the sensitivity can be increased by a factor 10 to 100. However, even if the nEDM is not discovered, further improvement of the existing limit can significantly reduce the available parameter space and eliminate some of the theoretical $\mathcal{CP}$ violation models (in fact

it has already ruled out a large number of models over the last 50 years). Therefore, an improvement of the present upper limit by one or two orders of magnitude would yield a sensitive test of physics beyond the SM and could provide some answers essential for our understanding of the Universe, both in particle physics and on the cosmological scale.

Historical review The history of EDM measurements started in 1950 when Purcell and Ramsey suggested to test the parity symmetry via detection of the neutron EDM and deduced the first upper limit for nEDM from earlier neutron–nucleus scattering data [19]. Their own pioneering experiment moved the upper limit two orders of magnitude down to $4 \cdot 10^{-20}\, e \cdot \mathrm{cm}$ [20]. That was the first time when the magnetic resonance method was used in the context of nEDM and it has been used ever since. It analyzes the tiny phase difference after spin precession for subsequent measurements with opposing electric field. The phase angle difference can be observed as a difference in polarization. There was also a succesfull attempt of employing Bragg reflection of thermal neutrons on a crystal to measure nEDM ($|d_n| < 8 \cdot 10^{-22}\, e \cdot \mathrm{cm}$ [21]). Neutrons passing through a non-centered crystal experience high electric field gradients (up to $10^9\,\mathrm{V/cm}$) and are spin rotated by Schwinger interaction. As in the other technique, a finite nEDM would cause an additional phase difference. The scattering method was not as succesfull as the Ramsey technique due to serious technical limitations (e.g. on alignment of the crystal orientation along the polarization of incident neutrons). However, there has been recently a proposal to employ it for a competetive nEDM measurement, using the cold neutron beam at ILL [22].

For the next 20 years, the magnetic resonance measurement and, in particular, Ramsey technique of separated oscillatory fields used on beams of thermal or cold reactor neutrons completely dominated the research, leading to $|d_n| < 3 \cdot 10^{-24}\, e \cdot \mathrm{cm}$ [23]. That was when a systematic limit, caused by motional magnetic field (so called $\mathbf{v} \times \mathbf{E}$ effect), was reached. In the rest frame of a neutron, $\mathbf{B_m} = \frac{1}{c}\mathbf{v} \times \mathbf{E_0}$. If now $\mathbf{E_0}$ is not completely aligned with $\mathbf{B_0}$, the magnetic field experienced by the neutrons acquires an additional component, which changes the sign upon E-field reversal, leading to a false effect, proportional to the neutron velocity (see also Sec. 4.2.1). This effect dominates the error for beam experiments.

In 1968 Shapiro proposed [24] to use UCN in nEDM experiments. The clear advantage of this approach is the suppresion of the motional field effect, due to the low velocities of UCN and the fact that they move randomly during observation. Moreover, UCN can be trapped and stored in bottles, thus can be used in an experimental apparatus for times comparable with the neutron lifetime, which is a factor of $10^4 - 10^5$ longer than neutrons in beam experiments. Such long UCN confinement can be achieved with bottles made from low loss materials. In the years that followed, a series of experiments with UCN, both in a "flow-through" and in a storage mode, was performed at PNPI (Gatchina, Russia) and at ILL resulting in $|d_n| < 9.7 \cdot 10^{-26}\, e \cdot \mathrm{cm}$ (PNPI, 1992 [25,26]), limited mostly by statistical errors (and low intensity of available UCN sources).

One more order of magnitude was gained in the '90-ies due to a new more intense UCN source at ILL [2] and better control over magnetic field fluctuations

provided by the use of high sensitivity magnetometers (e.g. Rb [27]) and, above all, by co-magnetometers, i.e. ^{199}Hg vapor stored simultaneously with the neutrons. Co-magnetometers monitor in-situ the changes in the magnetic field and can be used for on-line control of the precession frequency. The accuracy of the most resently published result, $|d_n| < 2.9 \cdot 10^{-26} \, e \cdot \mathrm{cm}$ [14], is still dominated by statistics $(d_n = (0.2 \pm 1.5 \, \mathrm{stat.} \pm 0.7 \, \mathrm{syst.}) \times 10^{-26} \, e \cdot \mathrm{cm})$. It is clear that in order to increase the sensitivity, either the UCN density in the trap or/and its total volume should be increased significantly. In addition to this, the recent experiment has identified a new important source of systematic effect, namely the geometric phase, which arises when the trapped UCN experience a magnetic field gradient in the along the direction of the E-field [28]. Therefore, next generation experiments will also need a better control over magnetic field gradients.

Perspectives   Given the exciting perspective of discovering New Physics or at least excluding some of the proposed SM extensions, if the accuracy of nEDM experiments is improved by one or two more orders of magnitude, several competing experiments are planned for the next half a decade. They all have to deal with two main necessities: need for higher UCN statistics and need for better control over magnetic fields. Two different approaches can be distinguished: cryogenic experiments with UCN production in superfluid ^{4}He and room temperature (RT) experiments, based on the same principle as the recent ILL experiment.

In cryogenic experiments cold neutrons will be converted to UCN in superfluid ^{4}He. Since the problem of extraction of UCN from the ^{4}He has not been solved, the nEDM measurement has to be conducted in ^{4}He, i.e. the UCN source and the nEDM spectrometer are realized in one single apparatus. In this way one gains much on the UCN density, adding however lots of technical complexity to the system, due to the cryogenics (operating temperatures below $1 \, \mathrm{K}$). The CryoEDM setup [29] by the Sussex/RAL/Oxford/Kure/ILL collaboration is located at a polarized cold neutron beam at ILL. The control over magnetic field is to be achieved with the combination of conventional μ-metal shields at room temperature ($\sim 10^6$ shielding factor) with a superconductiong inner shield, an array of 12 SQUID magnetometers and an additional neutron cell, with no electric field applied, which will act as a neutron magnetometer. The experiment is currently undergoing commisioning and claims to reach a statistical sensitivity of $\sim 10^{-27} \, e \cdot \mathrm{cm}$ within about a year of running. Within five years of running the sensitivity of $\sim 2 \cdot 10^{-28} \, e \cdot \mathrm{cm}$ is anticipated.

Another cryogenic experiment [30] will run at the Spallation Neutron Source (SNS) at the Oak Ridge National Laboratory (ORNL). A major innovation, when compared to the CryoEDM, is that ^{3}He, added to the moderator in tiny concentration, is going to act as a co-magnetometer as well as a neutron spin analyser. This is due to the large spin dependence of the n-^{3}He absorption. The reaction n + ^{3}He→p+^{3}H releases also 764 keV of recoil energy, which excites the superfluid ^{4}He and causes emission of UV scintillation light, detected with photomultipliers. By measuring the modulation of the scintillation light one can directly monitor the difference of neutron and ^{3}He precession frequencies. The Fundamental Neutron Physics Beamline (FNPB) at the SNS should be completed in 2010; the construction of the nEDM

spectrometer should start in 2009, however it will not commence data taking until 2014.

Considering the room temperature experiments, a multi-chamber experiment being set up by the PNPI group [31] is located at the UCN source at ILL. The statistics will be improved by means of larger total UCN storage volume. Some gain in sensitivity is also expected due to larger electric field gradients available. The apparatus consists of 4 double measurement chambers with opposite electric field orientations, which will allow to cancel some of the systematic effects. An array of 16 optically pumped Cs magnetometers is used for magnetic field monitoring and stabilization. The experiment aims at reaching the sensivity of $10^{-27}\,e\cdot\mathrm{cm}$ around 2010.

This work contributes to the nEDM project at PSI. The nEDM collaboration [32] was given access to the old RAL/Sussex/ILL [33] group apparatus located at ILL, the one which was used to measure the best result quoted. The collaboration plans to further advance the (proven) RT technique of nEDM measurements, using the old spectrometer in the initial phase of the project. The sensitivity improvement will be achieved mainly due to the high UCN flux at PSI (two orders of magnitude improvement over the present ILL source). Main developements leading to better control over systematic effects contain additional magnetometry systems and better magnetic shielding and stabilization.

In more detail, the PSI project consists of three phases:

- Phase I (at ILL, in progress until 2009): Improving the old apparatus (optimization of the ^{199}Hg co-magnetometer and the detection system), testing new solutions (external Cs magnetometer array), R&D (new storage materials, leakage current monitoring).

- Phase II (at PSI, 2009 – 2010): Moving the apparatus to the new source at PSI and a measurement on the $5\cdot10^{-27}e\cdot\mathrm{cm}$ accuracy level. In parallel, design and construction of a new double-chamber nEDM spectrometer. Planned upgrades contain an additional co-magnetometer (based on ^{129}Xe) and two large external ^{3}He magnetometers read-out by Cs magnetometers.

- Phase III (at PSI, 2011– 2015): Measurement with the new apparatus on the $5\cdot10^{-28}e\cdot\mathrm{cm}$ accuracy level. It will be achieved due to the advantages of the double setup, new magnetic shield and new magnetometry subsystems (developed in the Phase II). Also the statistics will increase because of the higher volume of the trap and its more desired location at the beam level (which is impossible in the Phase II).

This work, focused on search of new materials for the UCN trap, directly belongs to the first phase of the project. The results presented are an important contribution to its second and, possibly, also the third phase.

Three out of four projects discussed above have a realistic chance of reporting the result on the sensitivity level of $10^{-27}e\cdot\mathrm{cm}$ within next three years and, because of their technical complexity, it is hard to judge which one will be the first to do that. But the race has already started and, as explained before, what makes it

really exciting is the perspective of the first discovery of new physics beyond the SM, possible already at $10^{-27}e \cdot \mathrm{cm}$ sensitivity level and perhaps even before anticipated new discoveries from Large Hadron Collider (LHC). And if the sensitivity is pushed further to $10^{-28}e \cdot \mathrm{cm}$, then either:

- An nEDM will be observed

- SUSY is not a property of nature

- There are large cancellations, or some unknown other mechanism strongly suppresses EDMs despite $\mathcal{CP}$ violation elsewhere

If SUSY does not exist, still the baryon asymmetry must be explained, so investigations sensitive to new sources of $\mathcal{CP}$ violation will be critical.

1.1.2   Mirror matter hypothesis

The concept of a mirror world, as an attempt to restore global parity symmetry, has been attracting interest since the discovery of parity violation in weak interactions, started with the famous paper of Lee and Yang [34] and was significantly expanded in the work of Kobzarev, Okun, and Pomeranchuk [35]. The mirror matter idea was first applied to the Standard Model of particle physics in [36] and more recent overviews can be found in [37, 38].

The mirror world could hold a copy of the particle spectrum of our ordinary world and would have the same gauge group. If the ordinary world has the gauge symmetry $G_{SM} = SU(3) \times SU(2) \times U(1)$ with left-handed weak interactions $(V - A)$, the mirror world would be described by $G'_{SM} = SU(3)' \times SU(2)' \times U(1)'$ with right-handed $(V + A)$ mirror weak interactions, respectively. The left-right symmetry between both sectors, considered as a generalization of parity, might be then conserved on a more universal level $(G_{SM} \times G'_{SM})$. Matter and mirror matter would occupy the same space-time, interact essentially via gravity and present a viable explanation to the dark matter problem [39, 40, 41, 42, 43]. Besides gravity, other (new) interactions could show up in minute mixings of neutral matter particles — such as neutrons, neutrinos, pions, kaons, or positronium (see [44] for e^+e^-) — and degenerate mirror partners leading to oscillations between them.

So far, there is no experimental data excluding the mirror matter hypothesis. In the literature one can even find a number of clues, however controversial, indicating that some of the observed anomalies could be also explained by various mirror world models:

- Pioneer spacecraft anomaly [45]

- Anomalous meteoroids impacts [46]

- Anomalous stars and planets [47, 48]

- Some WIMP search results (DAMA/NaI) [42]

- Ultra high energy cosmic rays above the GZK cutoff [49]

Apart from the dark matter search, also experiments looking for invisible decay modes of orthopositronium have large potential of proving that the mirror matter hypothesis is not valid. Decreasing the upper limit for the branching ratio of the decay to mirror orthopositronium [44] by two further orders of magnitude would already make most of the above mentioned phenomena obsolete.

Neutrons provide an additional possibility to discover the mirror world by means of the neutron-mirror neutron oscillation search in UCN storage experiments. Interestingly, the (magnetically shielded) nEDM spectrometer is perfectly suited to perform this type of measurements. The nEDM collaboration took advantage of that fact and conducted the experiment in March 2007. The last chapter of this work deals with that issue in more detail and, as no oscillations have been observed, contains the first direct experimental limit on the neutron-mirror neutron oscillation time. Since, as for the moment, the experimental uncertainty is dominated by statistical errors a further improvement in the density of stored UCN is being considered, which is possible also with better trap materials.

Chapter 2

Physics of UCN

UCN are usually defined as neutrons which can be stored in suitable material bottles. As the Fermi potential of the best material available, ^{58}Ni, is 335 neV only neutrons with kinetic energies lower than that can be potentially stored in the way described below. For neutrons, 335 neV translates to velocities below 8 m/s or temperatures below 4 mK. De Broglie wavelentghs of so slow neutrons exceed 50 nm and reach molecular scale, therefore when UCN hit a material surface, they strongly interact in a coherent way with a *large* ($\sim 10^9$) number of nuclei. To describe that interaction, the mean *Fermi potential*, V_F, is introduced (see Sec. 2.2), which is an effective strong scattering potential felt by the incoming neutron at the material surface

$$V_F = \frac{2\pi\hbar^2}{m_n} \sum_i N_i b_i, \tag{2.1}$$

where N is the scattering center density, m_n the neutron mass and b denotes the bound coherent scattering length. Neutrons with kinetic energies lower than V_F are reflected from the surface independent of the angle of incidence. It is convenient, to define also a *critical velocity*, v_F, which can be classicaly derived straight from the Fermi potential,

$$v_F = \sqrt{2V_F/m_n}. \tag{2.2}$$

UCN with velocity component perpendicular to the surface higher than v_F are transmitted and, in most of the cases, subsequently absorbed or up-scatterd in the material (e.g. they are lost). This characteristic feature of UCN allows to store them in bottles for times close to the free neutron life time of 885.7 s [8], which gives interesting experimental perspectives.

The following sections deal with fundamental properties of neutrons, neutron scattering and its interactions with materials. Other methods of confining UCN in traps are also mentioned.

2.1 Properties of the neutron

As a massive particle, the neutron interacts with gravitational fields and in particular with Earth's gravitational field. The potential is given as

$$V_g = m_n g H, \tag{2.3}$$

where $m_n = 1.674927211(84) \cdot 10^{-27}$kg [50] is the neutron mass and H is the height. For example, 1 meter of height corresponds to $V_g = 102.57$ neV, which is a lot compared with typical UCN kinetic energy. Using classical ballistic formulas one can calculate UCN trajectories and the maximum height they can reach, which has the value in centimeters approximately equal to their kinetic energy given in neV. Thus, gravity can be also used to trap UCN.

The neutron is a fermion with a $\frac{1}{2}$ spin. From the Wigner-Eckhart theorem it is known that quadrupole (or higher rank) moments of any such particle are not allowed and that it can have only one favored orientation. Therefore both magnetic and electric (if it exists) moments of the neutron are parallel to the spin,

$$\mu_{\mathbf{n}} = \gamma \mathbf{S}, \tag{2.4}$$

where γ is the gyromagnetic ratio and $\mu_n = -1.9130427(5)\mu_N$ [8]. The existence of the magnetic dipole moment of the neutron is a consequence of its composite quark structure and can be approximated in the QCD framework.

The potential energy V of a neutron in the magnetic field B is given by

$$V = -\mu_{\mathbf{n}} \cdot \mathbf{B}. \tag{2.5}$$

Since the value of the potential is again comparable to the UCN kinetic energies (5 T field would correspond to about 300 neV UCN), Therefore, in the inhomogeneous magnetic field, neutrons experience a force proportional to the potential gradient, $\mathbf{F} = \nabla(\mu_{\mathbf{n}} \cdot \mathbf{B})$, which can be used to confine neutrons in magnetic traps.

In a similar way, magnetic fields and magnetized ferromagnetic materials, like magnetized iron foil in particular, are employed to polarize UCN beams. UCN in the presence of magnetic materials would experience total potential consisting of both magnetic and Fermi potential

$$V = V_F - \mu_{\mathbf{n}} \cdot \mathbf{B} = \frac{2\pi\hbar^2}{m_n} \sum_i N_i b_i \pm \mu_n B \,, \tag{2.6}$$

where the choice of sign depends on the orientation of the neutron spin relative to the magnetic field. UCN can be thus polarized by preferentially reflecting only one spin state.

2.2 Interaction with materials

Elastic scattering   The wavefunction of a particle scattered on a strong potential $V(r)$ of a nuclei can be described as

$$\psi(r \to \infty) \quad = \quad \psi_{Incident} + \psi_{Scattered} \quad \sim \quad A\,\mathrm{e}^{\mathrm{i}kz} + f(\theta,\phi)\frac{\mathrm{e}^{\mathrm{i}kr}}{r}, \tag{2.7}$$

a superposition of a plane wave and a spherical wave centered on the nucleus.

The differential cross section can be obtained from the scattering amplitude $f(\theta, \phi)$,

$$\frac{d\sigma}{d\Omega} = |f(\theta, \phi)|^2. \tag{2.8}$$

$f(\theta, \phi)$ can be approximated using the assumption that the nuclear potential is sferically symmetric and much greater than the UCN energy. In this case one can perform partial wave analysis, i.e. expand the function $f(\theta)$, now dependent only on θ, into a series of Legendre polynomials

$$f(\theta) = \sum_{l=0}^{\infty} (2l + 1) f_l(k) P_l(\cos\theta), \tag{2.9}$$

with the scattering amplitude $f_l(k)$ found to be given as

$$f_l(k) = \frac{e^{i\,\delta_l(k)} \sin(\delta_l(k))}{k}, \tag{2.10}$$

where $\delta_l(k)$ is a phase shift. Applying now the assumption that the UCN wavelength λ is much larger than the range of the interaction r_0, one neglects waves of higher order than s-wave ($l = 0$). It turns out that

$$\lim_{\lambda \gg r_0} f_l(k) \to -a \quad \implies \quad f(\theta) = -a, \tag{2.11}$$

where a is called the *scattering length*.

In order to introduce the Fermi pseudo potential V_F, we need to substitute that result into the Born approximation, given, in general form, by

$$f(\theta, \phi) = -\frac{\mu_A}{2\pi\hbar^2} \int V(\mathbf{r}') \, e^{i\,\mathbf{q} \cdot \mathbf{r}'} \, d^3 r, \tag{2.12}$$

where μ_A is the reduced mass for the neutron – nucleus two-body system. Since the UCN energy is not large in comparison with the nuclear potential $V(r)$, the perturbation theory and the Born approximation cannot be directly applied. Nevertheless, it is still useful to introduce a pseudo potential valid in the "zero energy" limit, which could be used within the first Born approximation to recreate the scattering amplitude and the change of the UCN wavefunction far from the scattering center.

Thus, from Eq. 2.11 and Eq. 2.12 we get

$$a = \frac{\mu_A}{2\pi\hbar^2} \int V(\mathbf{r}') \, e^{i\,\mathbf{q} \cdot \mathbf{r}'} \, d^3 r \tag{2.13}$$

and the solution is given by

$$V_F(\mathbf{r}) = \frac{2\pi\hbar^2 b}{m_n} \delta^{(3)}(\mathbf{r}), \tag{2.14}$$

where $b = \frac{m_n}{\mu_A} a$ is known as the bound nucleus scattering length. If b is positive, which is usually the case, the Fermi pseudo potential is repulsive. Finally, after averaging

that formula over many scattering centers, the mean Fermi potential (Eq. 2.1) is obtained.

Neutrons can be also absorbed by nuclei, which one takes into account introducing absorption cross section σ_a. In the low energy limit, i.e. for UCN, it is inversely proportional to the velocity $\sigma_a \propto \frac{1}{v}$. To fully describe the UCN scattering process one introduces an averaged complex potential

$$V = V_F - \mathrm{i}\,W, \quad W = \frac{1}{2}\hbar v \sum_i N_i \sigma_{ai}, \tag{2.15}$$

where the imaginary part $-\mathrm{i}\,W$ in the Schödinger equation would cause the probability density to decay. In the low energy limit W is independent on the neutron velocity. In case of UCN scattering, both absorption and inelastic scattering (when the neutron energy is increased beyond the ultra cold range) are responsible for losses. Since the inelastic scattering is also dependent on $1/v$, one can treat both phenomena with Eq. 2.15, substituting σ_a with $\sigma_l = \sigma_a + \sigma_{ie}$, which contains both contibutions.

Optical properties   Collision of an UCN with a material surface can be described by the Schrödinger equation for a neutron of energy E interacting with a complex potential barrier of the form

$$V = 0 \qquad x < 0, \tag{2.16}$$
$$V = V_F - \mathrm{i}\,W \quad x > 0, \tag{2.17}$$

where infinite depth of the material is assumed. From the solutions for inside and outside of the potential barrier, amplitudes of resulting waves are obtained

$$\psi_{x<0}(x) = \mathrm{e}^{\mathrm{i}kx} + R\,\mathrm{e}^{-\mathrm{i}kx}, \quad \psi_{x\geq 0}(x) = T\,\mathrm{e}^{\mathrm{i}k'x}. \tag{2.18}$$

The amplitude R of the reflected wave is given by

$$R = \frac{\sqrt{E} - \sqrt{E-V}}{\sqrt{E} + \sqrt{E-V}}. \tag{2.19}$$

This can be expanded for $W \ll V$, which is usually the case, resulting in

$$|R|^2 = 1 - \frac{2W}{V_F}\sqrt{\frac{E}{V_F - E}}. \tag{2.20}$$

Even if the $E < V_F$ and the wave is mostly reflected, there is still some loss probability proportional to W, due to the transmitted evanescent wave, which enters the inside of the material with penetration depth of the order of $100\,\text{Å}$. The losses are described by *loss probability per wall collision* $\mu(E)$, defined as $\mu(E) = 1 - |R|^2$. Generalizing our considerations for a three dimentional motion, from Eq. 2.19 one gets

$$\mu(E, \theta) = 2\eta\sqrt{\frac{E\cos^2\theta}{V_F - E\cos^2\theta}}, \tag{2.21}$$

where $\eta = W/V_F$ is the *UCN loss factor*.

Finally, for the case of stored UCN, this equation can be integrated over all angles of incidence [51, p. 25]

$$\bar{\mu}(E) = 2\eta \left[\frac{V_F}{E} \sin^{-1} \left(\frac{E}{V_F} \right)^{1/2} - \left(\frac{V_F}{E} - 1 \right)^{1/2} \right], \tag{2.22}$$

obtaining the commonly used parameter $\bar{\mu}$.

It was found that for all materials except Fomblin oil[1] the measured losses were much higher than expected from the theory. Several mechanisms of that phenomena have been proposed and the clear unambiguous solution of the problem has not been found yet. However, it has been shown experimentally, that at least part of the "anomalous losses" can be explained by (i) holes and cracks in the coating surfaces, (ii) microscopic or nanoscopic dust particles present on the surface or (iii) hydrogen contamination on and in the surface [52,53].

More complicated situation considered later in this work involves UCN interaction with material with Fermi potential V_F covered with a layer of material with potential V_F' and thickness d. Materials with poor Fermi potential can be coated with a thin layer of another much better material, in order to improve their ability to store UCN (so $V_F' > V_F$). Therefore, also losses due to the transmission through the coating and their dependency on the coating thickness become an important issue. The solution of the problem is easily available in the UCN related literature (see e.g. discussion by Golub [51, Sec. 2.4.3]) and in basic quantum mechanics textbooks.

As before, we assume that UCN are coming from a region where potential equals zero ($x < 0$). But this time the region where $0 < x < d$ corresponds to the coating with the potential V_F' and $x > d$ to the base material (V_F). Then the general form of the Schrödinger equation solutions for three relevant regions are given as:

$$\psi_{x<0}(x) = e^{ikx} + R\, e^{-ikx}, \quad \psi_{0<x<d}(x) = A\, e^{-\beta x} + B\, e^{\beta x}, \quad \psi_{x>d}(x) = T\, e^{-\kappa(x-d)}, \tag{2.23}$$

where

$$\beta = \sqrt{\frac{2m_n}{\hbar^2}(V_F' - E)} \quad \text{and} \quad \kappa = \sqrt{\frac{2m_n}{\hbar^2}(V_F - E)}. \tag{2.24}$$

The main point of interest is the transmission probability amplitude T for the case of UCN energy $E < V_F'$. In this situation, from boundary and continuity conditions one obtains

$$T = \frac{2}{D} \quad A = \frac{e^{i\beta d}}{D}(1 + i\,\kappa/\beta) \quad B = \frac{e^{-i\beta d}}{D}(1 - i\,\kappa/k') \tag{2.25}$$

$$D = \cosh(\beta d)\left(1 + i\,\frac{\kappa}{k}\right) + i\sinh(\beta d)\left(\frac{\beta}{k} - i\,\frac{\kappa}{\beta}\right) \tag{2.26}$$

Calculated amplitudes can be now used to derive contribution to the loss probability per bounce η for both wall materials

$$\eta = \int [N\sigma_l(v)]_x |\psi(x)|^2 \, dx, \tag{2.27}$$

---

[1]Perfluorinated Polyether.

which depends on the UCN loss cross section of the materials (the integration has to be conducted separately for each region).

The above discussion may be applied directly to Sec. 5.4.3.3, where we estimate the minimal necessary thickness of a deuterated polymer coating. However, because of the anomalous losses, results obtained in that way are not useful and a simplified approach turns out to be more practical, which neglects the UCN absorption/up-scattering loss and takes into account exclusively the effect of quantum tunnelling through a thin film.

Chapter 3

The nEDM Experiment

3.1 The principle of the measurement

The measurement is made with neutrons stored in a cell (bottle) placed in uniform collinear E- and B-fields. The Hamiltonian determining the energy states of the neutron depends on the terms $\mu_\mathbf{n} \cdot \mathbf{B}$ and $\mathbf{d_n} \cdot \mathbf{E}$, where $\mu_\mathbf{n}$ denotes the neutron magnetic moment and $\mathbf{d_n}$ the hypothetical electric dipole moment. Depending on the relative orientation (parallel or anti-parallel) of the E- and B-fields, the energy of the state is given by $h\nu_{\uparrow\uparrow} = 2|\mu_n|B - 2d_n E$ or $h\nu_{\uparrow\downarrow} = 2|\mu_n|B + 2d_n E$, respectively. The precession frequencies ν relate to d_n via

$$h\delta\nu \equiv h(\nu_{\uparrow\uparrow} - \nu_{\uparrow\downarrow}) = -4d_n E. \tag{3.1}$$

Thus, the goal is to measure, with the highest possible sensitivity, the shift $\delta\nu$ when a strong E field is reversed relative to the direction of B_0, the main magnetic field in the experiment.

The neutrons are prepared in a spin-polarised state, and their precession frequency ν is then measured using the Ramsey separated oscillatory field magnetic resonance method. The neutron spins are precessed by $\pi/2$ by a magnetic field pulse transverse to B_0 and oscillating at the neutron Larmor frequency, $B(t) = B_T \cos(2\pi\nu_L \cdot t)$. Then the neutrons precess freely (around the direction of B_0) for a time T ($\sim 130\,\text{s}$) and, if the neutron electric dipole moment is non-zero, $d_n \neq 0$, the precession frequency in the combined magnetic and electric field is different from the Larmor frequency. Thus, a phase difference proportional to the precession time T builds up, $\phi \approx (2\pi\nu - 2\pi\nu_L) \cdot T$, which has opposite sign for $E \uparrow$ and $E \downarrow$. During time T, B_0 is monitored by a ^{199}Hg co-magnetometer, i.e. polarized mercury vapor stored in the same volume with the UCN. After that the oscillating field is activated again (strictly in phase with the first $\pi/2$ flip) and the UCN are again precessed by $\pi/2$. If $d_n = 0$, the spins after two $\pi/2$ pulses are all oriented anti-parallel to their initial direction. In any other case, the accumulated phase shift results in a different neutron spin orientation. The last step is to analyze the number of neutrons N_{up} and N_{down} that finish in the two spin states (up or down) relative to B_0. This is accomplished by transmission through a magnetized iron foil, the same which is used for polarizing when filling the chamber.

The experiment is operated on a batch cycle principle: (a) fill with polarised neutrons for ~ 40 s, (b) carry out the magnetic resonance, and (c) empty, spin analyze and detect to obtain N_{up} and N_{down}. Fig. 3.1 shows N_{up} from a series of batch cycles, each with a slightly different offset between the Larmor frequency and the oscillating field frequency. For the data-taking, a working point is chosen at a half-height position
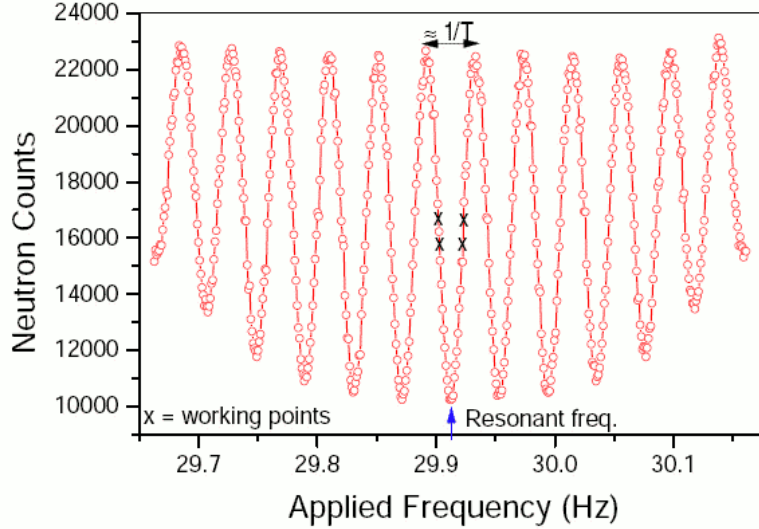

Figure 3.1: The number of UCN after spin analysis after application of Ramsey separated oscillatory fields, as a function of the oscillation frequency (from [54]). Note, that the separation of 2 maxima depends on T, the free precession time.

close to the centre of the resonance pattern of Fig. 3.1, where the slope of the curve is greatest and so is the sensitivity. The cycles are conducted continuously, while the direction of E is reversed a few times per day. One can then use the data to obtain d_n from the relation

$$d_n = \frac{(N_{up,\uparrow\uparrow} - N_{down,\uparrow\uparrow} - N_{up,\uparrow\downarrow} + N_{down,\uparrow\downarrow})\hbar}{2\alpha ETN}, \tag{3.2}$$

where α is the visibility of the central resonance fringe (represents the efficiency of maintaining polarization throughout the process) and N is the sum of the four counts. The error due to counting statistics is given as

$$\sigma(d_n) = \frac{\hbar}{2\alpha ET\sqrt{N}}. \tag{3.3}$$

The above formulae can be applied assuming that the B_0 field has not changed over the four measurements. This assupmtion is to large extent fulfilled, because of the magnetic shield, which suppresses the ambient field. Residual changes of the magnetic field can be still corrected for with the ^{199}Hg magnetometer.

For more details on Ramsey method of separated oscillatory fields, see Ref. [55, Sec. 3.5].

3.2 Experimental apparatus

The most detailed desription of the RAL/Sussex/ILL nEDM spectrometer is available from Ref. [55, Chapt. 5], here we will focus only on the most relevant elements. The schematic of the apparatus is shown in Fig. 3.2.
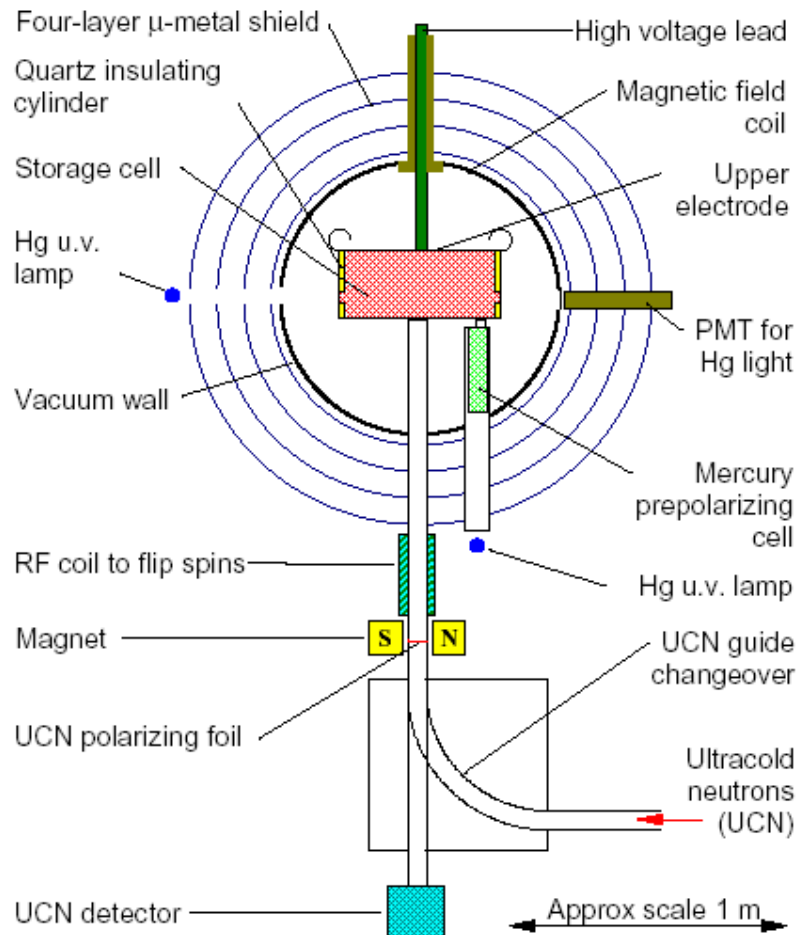

Figure 3.2: RAL/Sussex/ILL nEDM spectrometer (from [54]).

3.2.1 UCN guides

The neutrons, coming from the ILL UCN turbine (described in Ref. [2]), are guided to the apparatus by a 5.9 m long horizontal tube (78 mm inner diameter) made of stainless steel, which has been electropolished and coated with a thin layer of ^{58}Ni/Mo. The loss rate of the horizontal guide is approximately 10% per meter. At the switch pot, neutrons are directed upwards to the storage chamber via vertical guides; first a 25 cm long Ni/Mo coated copper section, then a 1.5 meter long beryllium coated glass tube, both of 68 mm inner diameter. Glass and copper tubes are used in order to avoid remanent magnetisation, typical for stainless steel tubes, which would depolarize

UCN. Additionally, glass can be penetrated by the oscillating field produced by the spin flipper coil (see 3.2.3).

3.2.2   The storage chamber

The storage chamber consists of a hollow electrically insulating cylinder located between a HV electrode (top) and a ground (bottom) electrode. The full volume of the trap is approximately 20 liters. At present the insulator is made of fused silica HSQ300. It has UV grade fused silica (UVFS) optical windows on either side, of 50 and 57 mm diameters, which roughly correponds to the divergence of the UV light beam, used for the ^{199}Hg co-magnetometer.

The electrode surfaces are coated with DLC with a Fermi potential of about 225 neV. The cylinder fits into 15 mm deep grooves in both electrodes, which reduces HV breakdown probability. Both UCN (78 mm diameter, DPS coated) and ^{199}Hg (14.5 mm diameter, Teflon) shutters are recessed into the bottom electrode in order to minimize their influence on HV stability. The shutters are controlled by pistons powered by compressed air. The gas tight seal between the insulator and the electrodes (necessary for the ^{199}Hg operation, see below) is made with two teflon o-rings located in the grooves.

An electric field of up to 180 kV (which translates to 15 kV/cm) is applied to the top electrode and its polarity is reversed after each series of measurement cycles. High voltage is provided via the HV feedthrough and a cable, with a 1 MΩ resistor close to the feedthrough, connected to a HV generator.

It is essential that all the materials used in the vicinity of the chamber are not magnetic.

3.2.3   UCN polarization and detection

The polarizer foil (either a silicon wafer or an aluminum foil coated with a 200 nm layer of iron, magnetized with by permanent magnet positioned around the foil) is located between the two vertical guides, mentioned before. According to Eq. 2.6, the foil will have different potentials depending on the orientation of the neutron spin, $V_F \pm |\mu_n \cdot \mathbf{B}| = (204 \pm 120)$ neV. Neutrons with spin oriented in the direction of the field within the foil (called spin down) experience a Fermi potential of about 324 neV and are reflected (for $E_{kin.} < 324$ neV), while those with opposite spin orientation (called spin up) experience only 84 neV and most of them can pass the foil. Polarizations of ∼ 90% are typically achieved in this way.

Just above the magnetized foil, an adiabatic spin flipper is located. This spin flipper, which consists of a RF longitudinal coil in combination with the transverse, linearly decreasing fringe field of the polarizer magnet, is used normally at the end of the measurement cycle during emptying. The polarizing foil acts at that time as a spin analyzer; UCN which are in the spin up state pass through the polarizing foil, the remaining ones are unable to do so until the spin flipping coil, located above the foil, is turned on, reversing their spin orientation. During emptying the switch-pot provides a direct connection to the ^{3}He, detector located ∼0.5 m below the foil.
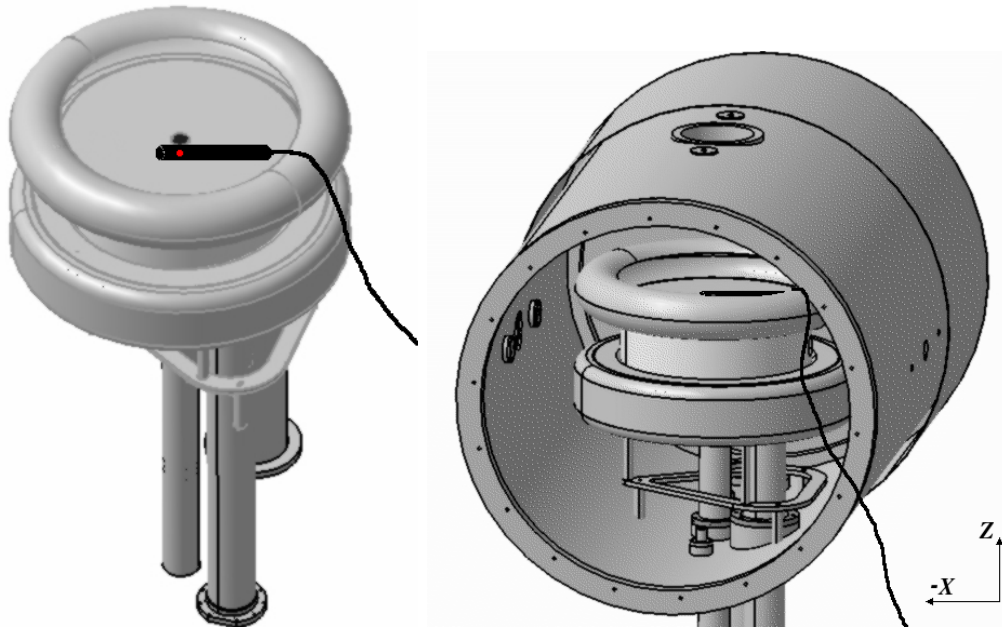
Figure 3.3: Location of the fluxgate meter: common view of the storage chamber (left) and its location in the vacuum tank (see also Fig. 3.2). The fluxgate was fixed on the top electrode and aligned with the main axes. Pictures from [56].

Typically, spin up neutrons are counted for 8 seconds, then the spin flipper is turned on and spin down neutrons can pass the foil for the next 20 seconds. At the end, the spin flipper is turned off and spin up neutrons are detected again, this time for 12 seconds. The counting periods are adjusted such that for unpolarized neutrons there is almost no asymmetry between spin up and spin down counts. However, because of storage effects during emptying some small residual asymmetry might still appear. Since the measurement of d_n is based on a *relative* change of this asymmetry upon E-field reversal, this is not a problem.

3.2.4 The magnetic field

Equation 3.1 shows that it is necessary to control very precisely the magnetic field in the storage volume. In order to keep the systematical uncertainties on a level of $10^{-26}e$cm a certain degree of homogeneity ($\sim 10^{-3}$) and temporal stability ($\sim 10^{-5}$) is required. The four layer μ-metal shield significantly suppresses the influence of the ambient fields, nevertheless, strong external fields still can penetrate the inside to some extent. It has several holes necessary, e.g. for the HV feedthrough, UCN guides, mercury prepolarization chamber, vacuum system etc., which unfortunately affect the field inside the vacuum tank. The ends of the shield can be removed to gain access to the storage chamber.

We have recently re-measured the axial and longitudinal shielding factors. A 1.4 m diameter external coil was used to generate a magnetic field of known magnitude (of

order $10\,\mu\text{T}$ at a distance of one meter from the coil center) and the field change inside the chamber was measured with fluxgate meters[1], located on the top electrode (see Fig. 3.3). The summary given in the Tab. 3.1 compares the measured values with the ones calculated employing both the "accurate" and the approximated Dubbers formula [57]. The magnetic permeability of the μ-metal was assumed as 20000 for the calculation.

Axis	Exact calculation	Approx. calculation	Measurement
X	24023	22000	21500
Y	3550	3460	1935
Z	24023	22000	6500

Table 3.1: Comparison of calculated and measured shielding factors for the magnetic shield of the nEDM experiment, where "X" corresponds to the shield symmetry axis. The most critical direction is "Z", because vertically oriented fields would directly affect the spin precession frequency.

The shielding factor of the nEDM magnetic shield could be then understood with a value of $\mu \sim 20000$ (or better, and stronger influence of the holes) [58].

The shield properties can be negatively affected by mechanical stresses and thermal expansion, therefore each time after it is disturbed, e.g. by opening, a demagnetization procedure is conducted. A slowly oscillating current is sent through dedicated coils wrapped around the shields. The remanent magnetization is cycled over the μ-metal hysteresis loop. Over about 20 minutes the oscillation amplitude is gradually reduced to zero, and so is the magnetization of the shields.

Batch-by-batch magnetic field variations observed in the experiment of the order of 10 pT are common and sudden jumps about one order of magnitude higher would occur several times per day [59].

The coil, which generates the 1 μT main static guiding field B_0, is wound directly onto the vacuum vessel (see Fig. 3.2), with a constant number of turns per unit vertical distance. The field is aligned in the vertical direction and is driven by a high-stability current source.

3.2.5 The ^{199}Hg magnetometer system

As the B_0 field stability is the central assumption, it is monitored during the measurement with a Hg vapor co-magnetometer. The precession frequency of the neutrons and ^{199}Hg atoms is given by respective formulas

$$\omega_n = -\gamma_n B_n, \quad \omega_{^{199}\text{Hg}} = -\gamma_{^{199}\text{Hg}} B_{^{199}\text{Hg}}, \tag{3.4}$$

where gammas are the gyromagnetic ratios and B is the strength of the experienced magnetic field. The magnetic field experienced by the neutrons can be deduced from

$$B_n = -\frac{\omega_n}{\gamma_n} = -\frac{R\omega_{^{199}\text{Hg}}}{\mathcal{R}\gamma_{^{199}\text{Hg}}} = \frac{R}{\mathcal{R}} B_{^{199}\text{Hg}}, \tag{3.5}$$

---

[1]Mag-03MC500 and Mag-03MCL70 from Bartington

where $\mathcal{R}$ is the (constant) ratio of gyromagnetic factors, measured e.g. by May [55] and $R \equiv \frac{\omega_n}{\omega_{199\text{Hg}}}$ is directly measured in the experiment. Thus, based on the co-magnetometer measurement a proper correction can be applied to the measured neutron precession frequency. The B field experienced by ^{199}Hg and by the neutrons is not exactly the same, mostly because of different centers of gravity for both species. Despite that, the method is good enough to significantly reduce the systematic uncertainty.

The ^{199}Hg vapor, produced by heating ^{199}HgO and spin-polarized in the prepolarizing cell by optical pumping from the light emmited by a ^{204}Hg discharge lamp, is fed into the storage chamber just after it is filled with UCN. ^{199}Hg atoms are also rotated to the precession plane by an RF pulse at the Hg Larmor frequency and then precess around the B_0 field. Their precession frequency is monitored by measuring the modulation of a UV beam of circularly polarized light, produced by another ^{204}Hg discharge lamp and detected by a photomultiplier tube (PMT). If the mercury vapor has a polarisation P, which is precessing in a plane perpendicular to the light polarization plane, then the absorption cross section σ will vary sinusoidally with the precession frequency between the maximal and minimum values of $\sigma_0(1 + P)$ and $\sigma_0(1 - P)$. The amplitude a of the transmitted light intensity oscillation is then given by

$$a = I_0 \exp(-n\sigma_0 L)(\exp(n\sigma_0 LP) - 1), \tag{3.6}$$

where σ_0 is the light absorbtion cross section per atom, n is number density, L is the thickness of target atoms and I_0 the initial light intensity.

The readout provides the average ^{199}Hg precession frequency inside the chamber, which can be translated into the average magnetic field and used later to correct the data for field variations. The co-magnetometer has been described in more detail elsewhere [60, Chapt. VII], [61].

3.3 Operation modes

The nEDM apparatus can be operated in several modes (for more see [55, Sec. 5.3]). After a certain filling time, typically 40 seconds, the entrance to the chamber is closed with a shutter and one of the following run types is carried out:

- nEDM run: as described in Sec. 3.1, Ramsey procedure with 130 s storage time for working points at the steepest gradient of the resonance curve. Used for actual data taking.

- Ramsey scan: as above, but more points of the resonance curve are measured (see Fig. 3.1). Used mostly for principle demonstration purposes.

- Alpha run: two cycles are performed; one with no $\pi/2$ spin flips (no precession phase) and one with the flips at the neutron resonance frequency. The data from the first type of cycle can be used to determine neutron storage time constants of the chamber and the T_1 depolarization time (depolarization due to the

wall reflections). The latter type is used to measure the T_2 depolarization time (depolarization mostly due to B-field inhomogeneities during the precession).

- Mercury run: measures the magnetic field with the Hg atoms. This is often used for setting up and testing when there are no neutrons available.

- Rabi run: instead of two RF pulses of the Ramsey technique, only one is applied. It is used to set up the strength of the RF pulses, so that the optimum visibility can be achieved in the other run types.

Chapter 4

Simulations

As already discussed in Sec. 1.1.1, the second phase of the PSI nEDM project involves moving the old nEDM spectrometer from ILL to the new intense UCN source at Paul Scherrer Institut and implementing all the improvements tested during the phase I. Data taking will aim at achieving $5 \cdot 10^{-27} e \cdot \mathrm{cm}$ accuracy. Understanding the experiment calls for detailed modelling of various aspects, e.g. neutron transport during the whole data taking cycle, the electric and magnetic field configuration, the ^{199}Hg co-magnetometer etc. This chapter concerns simulations of the UCN transport and modelling of the electric field.

Due to the complicated geometry of the system and the influence of gravity and magnetic fields on UCN, it is very difficult to treat the problem of UCN transmission and storage analytically. Therefore, a major effort was invested to create a dedicated Monte Carlo model of the experimental apparatus. For that purpose GEANT4-UCN was used, which is a well known GEANT4 package [62], adapted at PSI for the UCN physics (all the changes to the original code are described elsewhere [52, chapter 3], [63]). Furthermore, new materials with electrical properties different from those that have been used so far, change the electric field configuration around the storage ring, affecting both the high-voltage stability and the field homogeneity, which might result in some systematic effects. To assess the problem, Opera (TOSCA)[1], which is a commercially available finite elements calculation packages, was used.

In this chapter, the experimental setup is briefly described, outlining to what extent it was approximated by the models. Later, results from UCN transportation, storage simulations and, finally, electric field modelling are summarized. The intensity predictions for the Phase II of the nEDM project are definitely the most important result given in this chapter, since they have directly influenced the strategic planning and, in particular, motivated the decision to move the old RAL/Sussex/ILL apparatus to PSI.

---

[1]http://www.vectorfields.com

4.1   UCN transport with Geant4-UCN

Simulations of UCN storage and transmission through guides are crucial for understanding the experimental setup and optimizing its parameters. Geant4-UCN generates a large number of particles and separately calculates their tracks in many short steps, taking into account the geometry of the apparatus and relevant physics processes. The entire measurement cycle, with typical filling, storage and emptying periods was reproduced in the simulation, allowing for a direct comparison of simulated and experimental data. The materials, their essential properties (Fermi potentials, loss probabilities, diffuse reflection probabilities) and basic geometrical parameters of the model can be easily varied, allowing to select the most suitable configurations.

The model implemented in the simulation contains all the parts of the apparatus directly seen by the neutrons. At ILL (see Fig. 3.2), UCN traverse a 5.9 m long guide and an aluminum window before entering the switch pot. For the PSI source, the input beamline will be modified (see Fig. 4.4). The curved guide and the vertical guides, as seen in the Fig. 3.2, are implemented with their exact sizes and material properties. The iron polarizer foil was characterized by its Fermi potential for a preferred spin orientation (88 neV). The storage volume is defined by a quartz[2] cylinder with two quartz optical windows and both electrodes. As in reality, the DLC coated electrodes have grooves for the insulator and contain the recessed UCN and Hg shutters. Because Geant4-UCN allows convenient shutter operation, both shutters in the storage chamber together with the guide changeover system (the switch pot) open and close at pre-defined moments, like in the real measurement cycle. All the neutrons which enter the detector volume located at the bottom of the vertical guide are considered as counted.

Each data point shown in the plots in this chapter is a result of a separate simulation performed for about 10^5 UCN tracks, taking typically several hours of CPU time on dual core AMD Athlon 1.4 GHz with 2 GB memory. For convenience, the calculations were performed on the Merlin cluster [64] at PSI.

4.1.1   Model calibration

In summer 2005, the collaboration performed first measurements with the nEDM spectrometer at ILL. The main goal was to characterize the apparatus and later use the measured observables (storage, filling and emptying curves) to tune the poorly restricted parameters of the Geant4-UCN simulation in order to reproduce the data. The detailed geometrical model implemented allowed for fine-tuning of important simulation parameters, namely, the loss probabilities per wall collision, η, for the storage volume walls. While Fermi potentials and diffuse scattering probability in most cases are known with reasonable accuracy, the loss parameter, η, is more difficult to predict, usually differs from theoretical predictions by orders of magnitude and has to be measured experimentally.
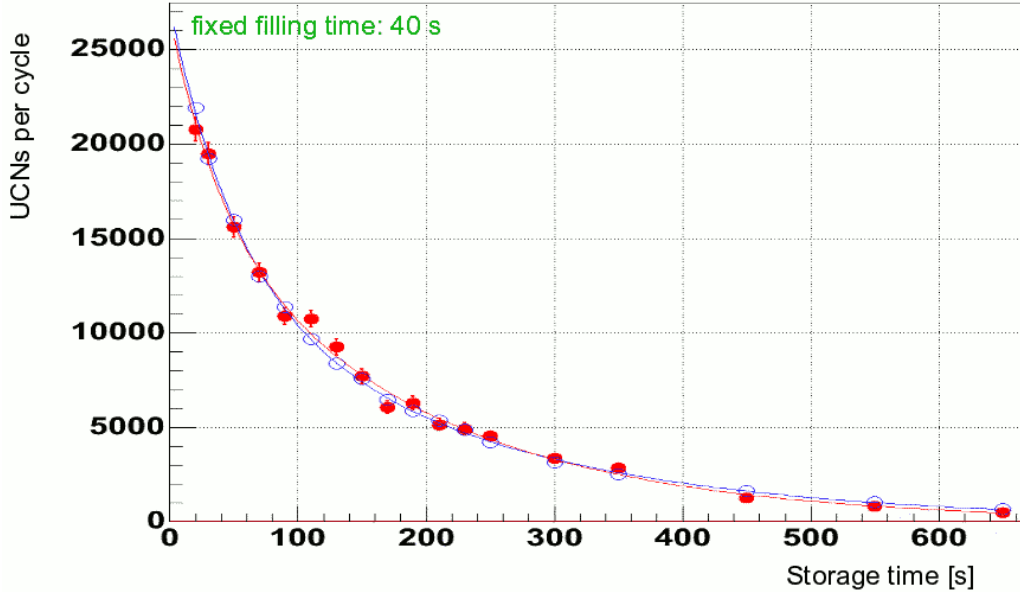
---

[2]fused silica HSQ300 from Heareus

Figure 4.1: Measured and simulated storage curves (number of UCN counted per cycle vs. the storage time). The simulation (red ●) was tuned to reproduce the measured data from July 2005 (blue ○). Each dataset was fitted with a sum of two exponentials.

The characteristics of the UCN beam at ILL were known only qualitatively. The initial UCN velocity distribution at the entrance to the horizontal guide was implemented as in Ref. [55, Sec. 4.2.1.2]. The velocities in the simulation are sampled from a Maxwellian distribution (for $T = 39$ K) with cutoffs corresponding to the critical velocity of the guide. Thus, the velocity components perpendicular to the guide are limited to 7.92 ms^{-1} (NiMo critical velocity), while the parallel component could be limited to less than 15 ms^{-1}. It was checked that the results of the simulation do not change with further increase of the latter limit. Both energy spectra, the initial one at the turbine exit and the one at the storage chamber entrance, after propagation through the guides are shown in the Fig. 4.3.

Part	Material	V_F [neV]	$\eta \cdot 10^4$	p_{diff}
Insulator	Fused Silica	90	3.0	0.1
Electrodes	DLC	225	3.0	0.1
Horizontal guide	NiMo	318	1.25	0.01
Vertical guide (bottom)	NiMo	318	1.25	0.01
Vertical guide (top)	Be	250	2.0	0.1
Polarizer	Fe	88	4.0	0.1

Table 4.1: Validated parameters of the model of the nEDM spectrometer at ILL: the Fermi potential V_F, loss probability per wall collision η and diffuse reflection probability p_{diff}.

After reproducing the experimental time constants of the storage curve measured
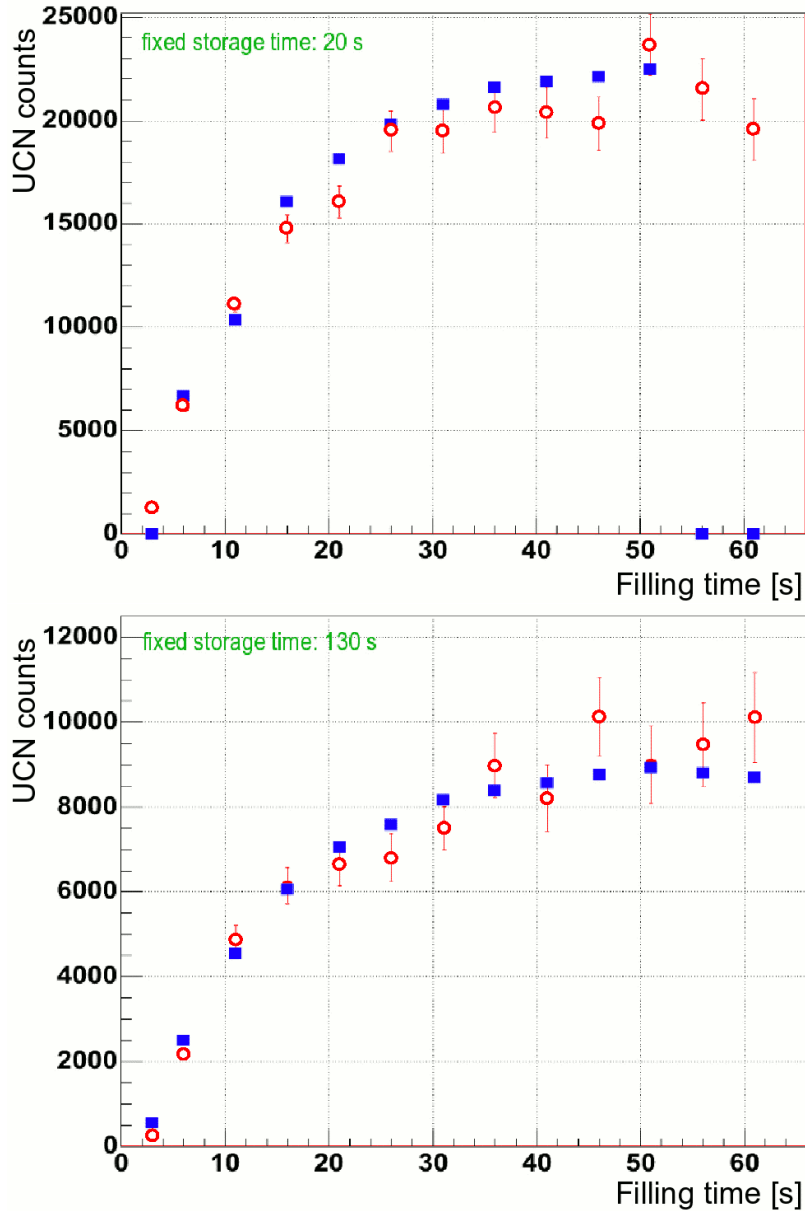
Figure 4.2: Measured and simulated filling curves measured for storage times of 20 and 130 s. The simulation (red ○), scaled by a common factor obtained from the comparison of the storage curves (see Fig. 4.1), reproduces the data measured in July 2005 (blue squares).

at ILL (see Fig. 4.1), also filling (Fig. 4.2) and emptying curves [65] were simulated, consistent with the measured data. Because, as mentioned earlier, the incident ILL UCN beam intensity was not known with sufficient accuracy, the simulated intensities were scaled by a constant common factor to fit the experimental data. The same factor was successfully used to check the consistency of the simulated filling and emptying data with the measurements. Table 4.1 summarizes the final properties of the model. It should be pointed out, that the properties of the storage volume walls

(a)   (b)
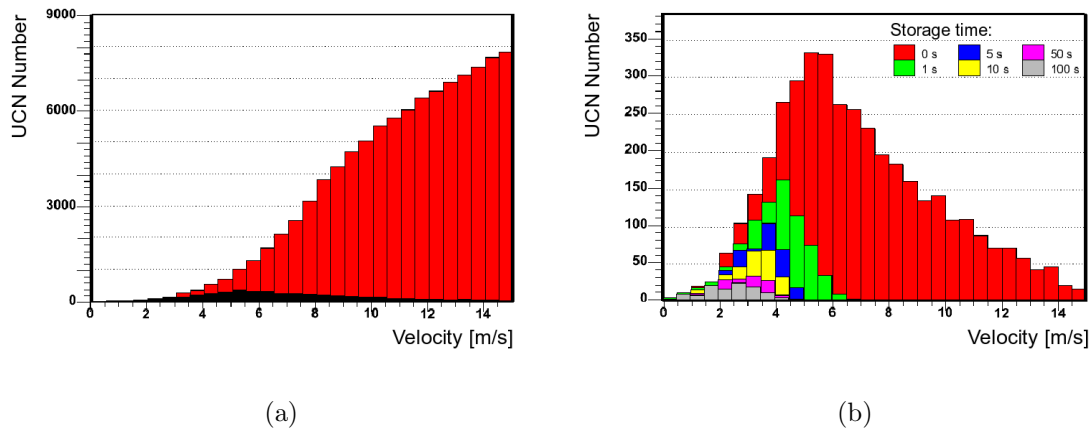
Figure 4.3: ILL input total velocity spectrum used for the simulation at the entrance to the horizontal guide (a). Only a small fraction of the initial spectrum reaches the storage chamber (black). On the right, the spectrum time evolution ("softening") inside the storage chamber is shown (b). Again, only a small fraction of the UCN, which have reached the trap (now in red), survives the first second of storage (green). During the first 50 s of storage all UCN with velocities exceeding the critical velocity of quartz (4.15 m/s) are lost.

(electrodes and the chamber) were treated integrally, since η and p_{diff} (the diffuse reflection probability) for both materials cannot be separated.

4.1.2 Predictions for the new PSI source

After the parameters of the model and, in particular, the storage volume had been determined, the code could be applied to predict the performance for the nEDM
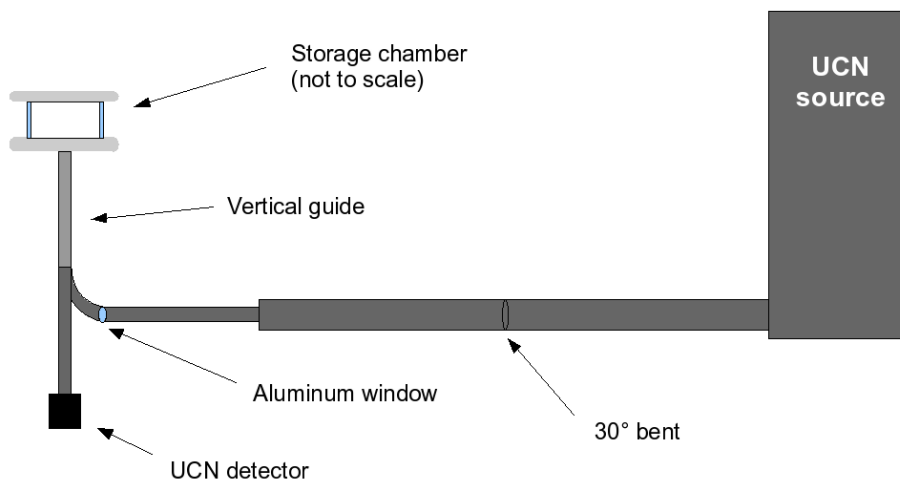
Figure 4.4: nEDM spectrometer at the PSI UCN source in the vertical configuration.

spectrometer operating at the PSI UCN source. The geometry was updated accordingly: a 18 cm diameter DLC coated horizontal guide with a 30° bend in the middle connects the apparatus with the large UCN storage tank of the source (see Fig. 4.4 and Tab. 4.2 for the material properties)[3]. The vertical guide of the apparatus was shortened to 1 meter, which is the minimal length given the constraints coming from the magnetic shield geometry. The iron foil polarizer was removed, since at PSI a superconducting magnet will be used to polarize UCN with close to 100% efficiency. The input beam parameters and its absolute normalization were obtained from independent simulations [66].
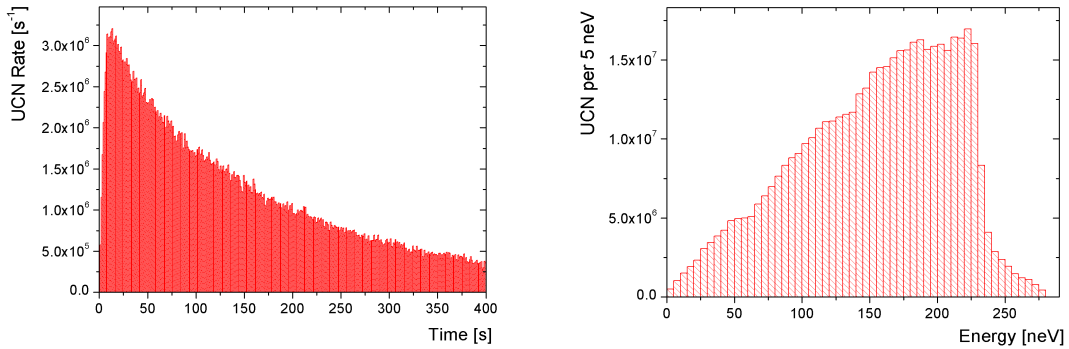
Figure 4.5: Simulated UCN rate and the energy spectrum at the exit from the horizontal guide coming from the PSI source. The proton pulse, which produces spallation neutrons converted to UCN starts at $t = 0$ and lasts 8 seconds [66].

Firstly, filling time curves were calculated and the optimal filling time was found to be around 20 seconds. This is to be compared with 40 seconds at ILL (see Fig. 4.6). The shorter filling time is a consequence of the pulsed operation mode of the PSI source, which will provide the highest intensity within the first 10 seconds after the pulse (see Fig. 4.5). The 20 seconds filling time is from now on used for all simulations.

The interesting question is how much improvement in statistics can be gained after moving the apparatus to PSI and whether it is worthwhile to change some of the materials, the insulator cylinder, in particular. Materials shown in the Tab. 4.2 have been used in the simulations. Different configurations of the storage chamber insulator wall and the electrodes have been tested (see Fig. 4.7), in connection with varying the length of the vertical filling guide, see Fig. 4.8. The gain factor is defined as the number of UCN detected after 130 seconds storage time, divided by the corresponding number obtained at ILL. It directly shows the increase in number of counts and, after taking the square root, shows how much will the statistical error bar, δd_n, be decreased (see Eq. 3.3). Gain factors for various configurations are summarized in the Tab. 4.3. The dependency of the number of UCN on the height of the storage

---

[3] The Fermi potential of DLC coating used here is about the same as that of the NiMo coating to be employed for the start-up of the PSI source
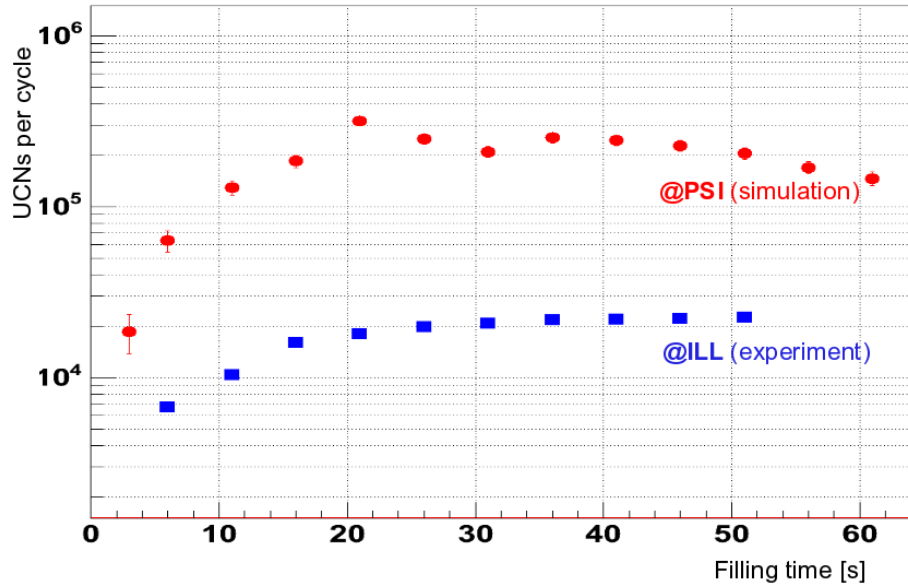
Figure 4.6: Filling time optimization for the experiment at PSI. Optimal filling time turns out to be 20 seconds. Although both curves are relevant for 20 seconds storage time and the quartz insulator, similar conclusions have been obtained also for the other storage time (130 s) and other materials (diamond and DPS).

Part	Material	V_F [neV]	$\eta \cdot 10^4$	p_{diff}
	Fused Silica	90	3.0	0.1
Insulator	DPS or Si_3N_4	174	3.0	0.1
	Diamond	305	3.0	0.1
Electrodes	DLC	241	3.0	0.1
	Diamond	305	3.0	0.1
UCN Tank	DLC	241	3.0	0.1
UCN Guide	DLC	241	3.0	0.05

Table 4.2: Parameters used for the simulations at the PSI UCN source.

chamber above the beamline was also studied (Fig. 4.8). The results show that reducing the height of the vertical guide gives more UCN only if the Fermi potential of the trap is increased beyond the present quartz value. The additional gain is around a factor of two.

The present geometry of the spectrometer limits the possibility of the height reduction. The cylindrical storage chamber can be operated only in horizontal orientation, with a vertical neutron guide coming directly from below and connected to the horizontal guide via a 90° bend, which is a dominant source of UCN losses during filling. Furthermore, any serious modification of the existing shield, e.g. drilling additional holes, is excluded. The minimal feasible height above the beamline corresponds to the magnetic shield radius, which is 1 m. Therefore, the so-called "vertical" configuration, shown in Fig. 4.4, is the best one, which is possible with the existing apparatus.

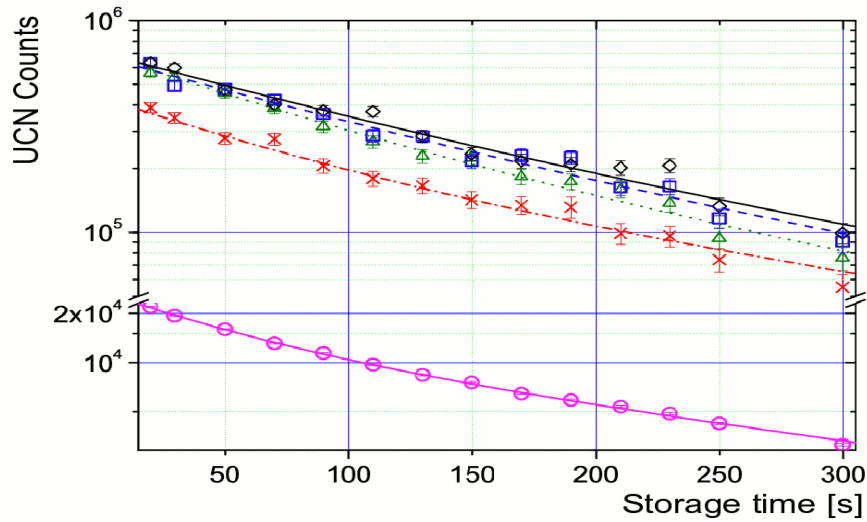Figure 4.7: Simulated neutron storage curves in the nEDM apparatus, with the storage chamber placed 1 m above the PSI UCN beamline: quartz+DLC (red ×, dash-dotted line), DPS+DLC (green △, dotted line), diamond+DLC (blue □, dashed line), diamond coated insulator and electrodes (black ◇, solid line). The experimental curve from 2005 ILL measurement is shown for comparison (magenta ○, solid line). The curves fitted to each dataset are sums of two exponents.
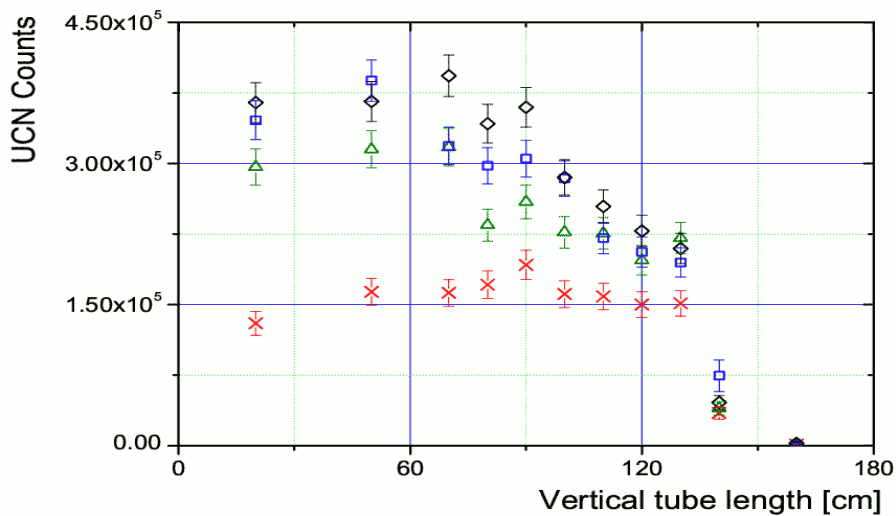

Figure 4.8: The position of the chamber above the horizontal UCN guide was varied in the simulation for different materials. The colors are as in Fig. 4.7: quartz+DLC (red ×), DPS+DLC (green △), diamond+DLC (blue □), diamond coated insulator and electrodes (black ◇).

Nevertheless, for Phase III of the project, the spectrometer contained inside a custom-designed shield can be located directly at the beamline level, without the bend. The first naive approximation of this idea is the "horizontal" setup shown
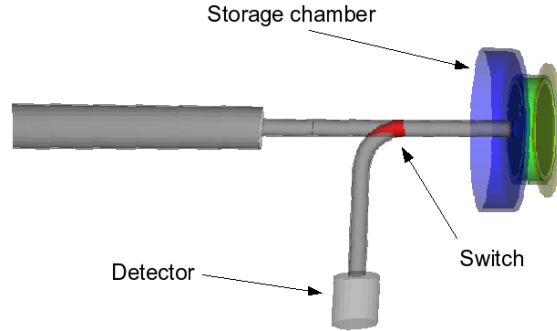
Figure 4.9: Horizontal configuration. The existing UCN storage chamber connected directly to the horizontal beamline. During emptying, neutrons fall down to the detector via the switch.

in Fig. 4.9. It consists of the existing storage chamber (which has about half the volume of the planned new system) connected directly to the horizontal guide. As mentioned, a superconducting magnet will be used to polarize the UCN instead of the foil, which would cut away a significant part (below 88 neV) of the available spectrum (Fig. 4.5). The aluminum window, needed for safety reasons (to separate vacuum in the source and in experiments), will be located inside the magnet, which largely reduces the transmission losses [67]. As a first order approximation the "horizontal" arrangement was then simulated without the Al window.For the results see Tab. 4.3.

Insulator	Electrodes	ILL	Vertical	Horizontal
Fused Silica	DLC	1	19	26
DPS or Si_3N_4	DLC	1.3	29	76
Diamond	DLC	1.5	33	89
Diamond	Diamond	1.7	35	99

Table 4.3: Gain factors (relevant for 130 s storage time) for the material studied and geometrical configurations at ILL and at PSI.

4.1.3   Conclusions

The optimal filling time for the nEDM spectrometer is 20 seconds. We conclude from Fig. 4.8 that reducing the height of the vertical guide is not important in the present configuration with a chamber made out of quartz and DLC. But it will improve the statistics in case one would use higher Fermi potential materials for the storage chamber. Keeping in mind the geometrical constraints of the old setup (due to certain features of the magnetic shield, the storage chamber must be located vertically at least one meter above the beamline), an icrease in V_F of the chamber to about 160 – 170 neV gives a 50% gain in statistics, while further increase of that parameter does not provide much more improvement. Assuming that V_F is enhanced to the level of about 160 neV, the statistical error of the nEDM measurement will be decreased by

a factor of five as compared to the present situation at ILL. The simulation results strongly support the idea to move the old nEDM spectrometer to PSI and use it for a real physics run. They have also motivated the decision to modify the mechanical support of the apparatus in order to put it as close to the beamline as possible.

Considering the phase III of the nEDM project, moving the storage volume to the beam level and further increase of the wall Fermi potential to $\sim$300 neV can yield up to 25% more neutrons, since it will be possible to efficiently trap also faster UCN.

4.2 Electric field modelling with Opera

An effect related to motional magnetic fields ($\mathbf{v} \times \mathbf{E}$ effect) was an important source of systematics in nEDM experiments with neutron beams. In storage experiments its influence is reduced by many orders of mangnitude but still has to be well controlled. A selected aspect of that systematic problem is discussed below. After analytical descripton, numerical calculations are employed in order to get some estimate on its influence on measured d_n.

4.2.1 Ordered motion

The following discussion is based on Ref. [68, Sec. 3.5.3.] and addresses the first order $\mathbf{v} \times \mathbf{E}$ systematic effect, coupled with the ordered motion of the UCN stored in the trap. One should keep in mind that it is not the only possible eystematic effect related with velocity; even without the ordered motion the first order $\mathbf{v} \times \mathbf{E}$ can couple to magnetic field gradients in the chamber and generate dangerous geometric phases, mimicking the nEDM signature. In addition, there is also a second order $\mathbf{v} \times \mathbf{E}$ effect and other effects caused by the B field inhomogeneities, which are neglected throughout this chapter. Further studies are ongoing [5].

Effective B field   According to special relativity, in the frame of a particle moving in a static electric field $\mathbf{E}$, a magnetic field $\mathbf{B_m}$ is generated

$$\mathbf{B_m} = \frac{\gamma}{c} \cdot \frac{\mathbf{v}}{c} \times \mathbf{E}. \tag{4.1}$$

To first order in v/c, B_m is

$$B_m \approx \frac{v}{c^2}E \quad (v \ll c) \tag{4.2}$$

The particle experiences the effective magnetic field $\mathbf{B} = \mathbf{B_0} + \mathbf{B_m}$. Total $\mathbf{B}$ field magnitude is given by the formula

$$B = \sqrt{(\mathbf{B_0} + \mathbf{B_{sys}})^2 + (B_m \cos\theta_{EB})^2}. \tag{4.3}$$

Substituting B_{sys} with $B_m \sin\theta_{EB}$, one obtains

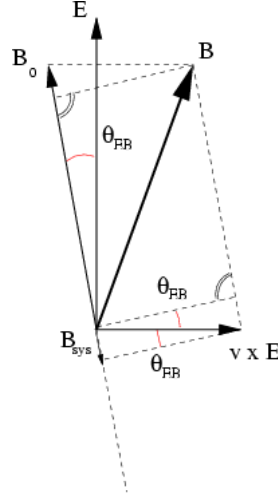$$B = \sqrt{(B_0 + B_m \sin\theta_{EB})^2 + (B_m \cos\theta_{EB})^2}. \tag{4.4}$$

Figure 4.10: Geometrical picture of the $\mathbf{v} \times \mathbf{E}$ effect. The particle velocity $\mathbf{v}$ points into page.

Taylor expansion of the above expresion for $\theta_{EB} \ll 1$ and $\frac{B_m}{B_0} \ll 1$, thus for nearly parallel fields and small motional component, gives

$$B = B_0 + \theta_{EB} B_m + \frac{1}{2} \frac{B_m^2}{B_0} + O^2 \left(\frac{B_m}{B_0} \right) + O^3 \left(\theta_{EB} \right). \qquad (4.5)$$

Finally, neglecting the higher order terms and using the Eq. 4.2, one obtains

$$B \approx B_0 + \theta_{EB} \frac{v}{c^2} E + \frac{1}{2} \frac{B_m^2}{B_0}. \qquad (4.6)$$

False nEDM   The dipole moment measured in the experiment is defined as

$$d_n^{exp} = \frac{\varepsilon^+ - \varepsilon^-}{4E}, \qquad (4.7)$$

where

$$\varepsilon^+ = 2\mu_n B + 2d_n E, \quad \varepsilon^- = 2\mu_n B - 2d_n E \qquad (4.8)$$

are measured for opposite $\mathbf{E}$ field orientations. Employing Eq. 4.6, one gets

$$\varepsilon^+ = 2\mu_n (B_0 + \theta_{EB} \frac{v}{c^2} E + \frac{1}{2} \frac{B_m^2}{B_0}) + 2d_n E, \qquad (4.9)$$

$$\varepsilon^- = 2\mu_n (B_0 - \theta_{EB} \frac{v}{c^2} E + \frac{1}{2} \frac{B_m^2}{B_0}) - 2d_n E.$$

After the subtraction, terms with B_0 and the quadratic one cancel, but the θ_{EB} dependent term remains

$$d_n^{exp} = \frac{1}{4E} (4\mu_n \frac{v}{c^2} \theta_{EB} E + 4d_n E) = \mu_n \frac{v}{c^2} \theta_{EB} + d_n. \qquad (4.10)$$

Therefore, the false EDM effect can be written as

$$d_{v \times E} \equiv \mu_n \frac{v}{c^2} \theta_{EB} \quad [e \cdot \text{cm}]. \tag{4.11}$$

For practical purposes: $d_{v \times E} = -6.70 \times 10^{-25} \, [e \, \text{s} \, \text{rad}^{-1}] \cdot v \cdot \theta_{EB}$, where v is in units of cm/s and θ_{EB} is in radians.

Net velocity v in Eq. 4.11 denotes the net-velocity of UCN moving in an ordered way in a certain direction around the storage chamber. In ideal conditions, when the storage chamber and the UCN guide system are axially symmetric, the same number of neutrons should move clockwise and counter-clockwise around the chamber such that the net-velocity would equal zero. In reality some small but finite effect might be expected, however it is additionally suppressed by diffuse reflections from the trap walls. In fact, with the typical wall collision frequency of 20 Hz and diffuse reflection probability on the level of 5 – 10%, the UCN motion should be isotropic already after a few seconds of storage and ordered motion should contribute only very little to the final result averaged over the full storage time.

Earlier analysis of that phenomena for a vertically oriented cylindrical chamber with a neutron guide entrance positioned asymmetrically on the side wall [69, Sec. 5.2.3] resulted in 5 cm/s average net velocity (given the average UCN velocity of a few m/s) for mirror reflections in the chamber and a negligible effect for the diffuse reflections.

For a symmetric, horizontal configuration of the existing apparatus, even assuming very pessimistically much less than the typical 5% diffuse reflection probability of the insulator, the net velocity over the full storage time should be at least an order of magnitude less (~ 5 mm/s net velocity). One should then keep in mind (see Eq. 4.11), that the E-field inhomogeneities, discussed in the next section, are to be multiplied by the small net velocity, which will result in an even smaller false effect on d_n.

4.2.2   Storage chamber

As the $\mathbf{v} \times \mathbf{E}$ effect scales also with the θ_{EB} angle, it is interesting to get some estimate of this property for the real setup. Opera is a state-of-art commercial software used for modeling with finite elements method (FEM), especially useful for calcualtion of electrostatic fields from given boundary conditions (solving the Laplace equations). A 2-dimensional model of the quartz precession chamber and both electrodes was implemented and the numerical solution was calculated. Since axial symmetry of the chamber was assumed, it is also valid for a 3-dimensional chamber. However, in reality the ^{199}Hg shutter and optical windows break the axial symmetry, so the results should be considered only as a first order approximation. Also only the E-field was calculated, the θ_{EB} is obtained with the assumption that the B-field is oriented along the vertical axis and perfectly homogeneous.

The field maps were calculated for several combinations of geometrical and electrical properties and different meshes, in order to test the reproducibility and accuracy of the results. Firstly, an up-down symmetric arrangement was solved, with both

electrodes identical to the top electrode. One expects small field deviations from the vertical direction inside the chamber near the insulator and mostly close to the grooves.Given the symmetry plane, both contributions to the $\theta_{EB} = \arctan\left(\frac{E_r}{E_z}\right)$, should have different signs in top and bottom parts of the volume and should cancel when averaged over the full space. The averaged result calculated for several different meshes equals 10^{-6} rad, therefore from now on this value should be considered as the systematical uncertainty of the model.

In addition to the normal configuration, as shown in Fig. 4.11, two other cases were studied in order to investigate the influence of the homogeneity of the chamber wall: one case with dielectric constant of the insulator changing linearly from 4.0 at the top to 3.8 at the bottom and another one, with reversed dependency (3.8 at the top an 4.0 at the bottom). Results of all three calculations are summarized in Tab. 4.4.

ε		$\theta_{EB}\,[10^{-3}\,\mathrm{rad}]$			$d_{v\times E}\,[10^{-28}\,e\cdot\mathrm{cm}]$
top	bottom	top	bottom	full	
3.8	3.8	−6.35	5.79	−0.28	−0.94
3.8	4.0	−7.41	4.93	−1.24	−4.16
4.0	3.8	−5.49	6.86	0.68	2.30

Table 4.4: Results of the E-field calculations. First two columns contain assumed dielectric constants at the top and bottom of the insulator ring (ε inbetween is extrapolated). Later follows the integrated θ_{EB} for the top half, the bottom half and the full storage volume. Finally, the false nEDM is obtained from Eq. 4.11, using the θ_{EB} values and an assumed ordered motion velocity of 5 mm/s.

All the obtained θ_{EB} results are much higher than the systematic uncertainty of the model. An average non-parallelism between B and E-fields of at least $10^{-4} - 10^{-3}$ rad can be expected in the storage volume. In case of the homogeneous insulator (constant ε), the observed asymmetry between top and bottom parts of the storage volume is apparently caused by the electrode geometries, i.e. different shapes of the top and the bottom electrodes. Five percent variation in dielectric constant along the insulator wall can obviously amplify (or reduce) that asymmetry. The model implemented exploits axial symmetry of the chamber. It does not take into account optical windows located in the insulator wall and shutters in the bottom electrode.

In conclusion, the first order $\mathbf{v} \times \mathbf{E}$ effect coupled to the ordered UCN motion should not contribute significantly to the systematic accuracy of the measurement. Even assuming very conservative value for the net velocity the result obtained is below the anticipated statistical uncertainty ($5 \times 10^{-28}\,e\,\mathrm{cm}$). For phase III of the project some more elaborate analysis would be required, including more details like shutter geometries, optical windows and reliable estimates for the ordered motion net velocity and the diffuse reflection probability of the chamber.
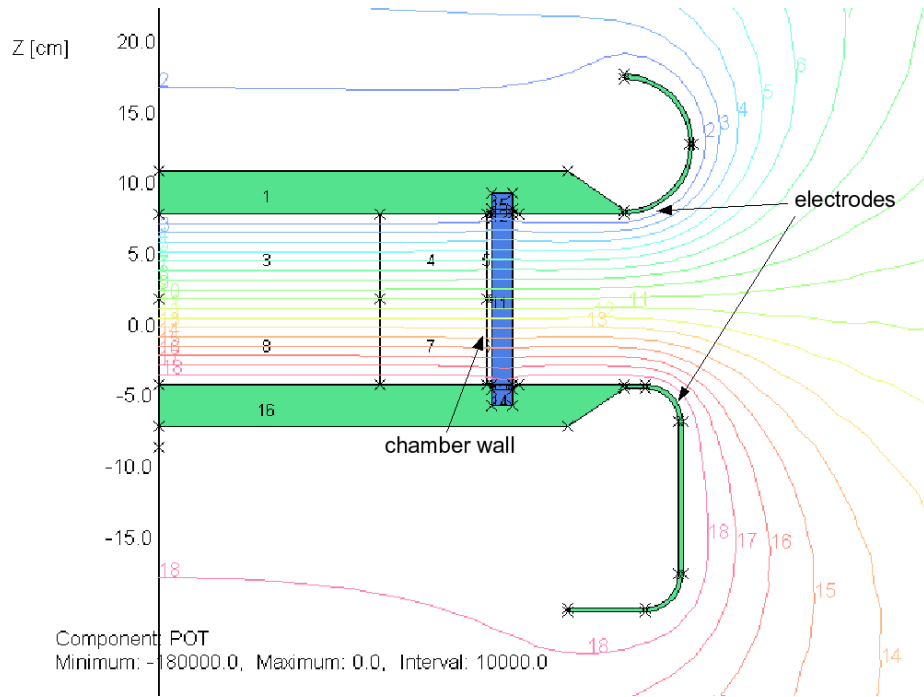
(a)
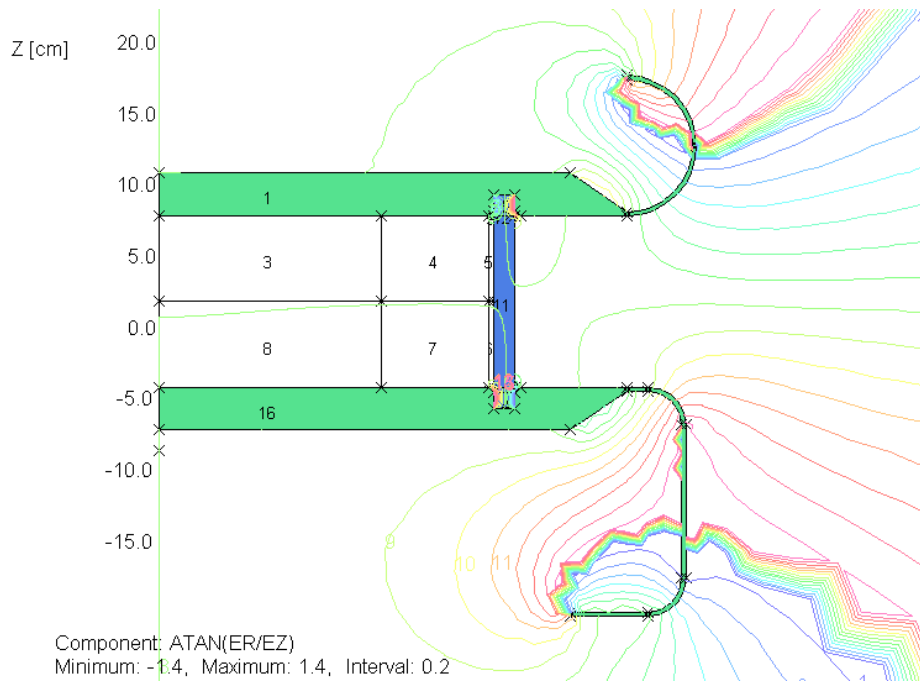
(b)

Figure 4.11: E-field configuration in the vicinity of the nEDM precession chamber, calculated with Opera 2D. Dielectric constant of the insulator is 3.8, the top electrode is at $180\,\mathrm{kV}$ potential and the bottom one is grounded. (a) Equipotential lines, drawn with $10\,\mathrm{kV}$ spacing, (b) lines of constant θ_{EB}, with $0.2\,\mathrm{rad}$ spacing.

Chapter 5

Improved wall material

The storage chamber is one of the most critical parts of the EDM spectrometer, because its material composition and surface quality affect strongly both the polarization and the number of neutrons detected at the end of storage. At the same time the trap is exposed to high electric field, which it has to stand, with minimum leakage currents. Additionally a co-magnetometer, based on Hg vapor, is simultaneously stored inside the chamber, which sets new requirements for the system and makes the entire task quite challenging. So far, good insulating materials such as BeO [70], Al_2O_3, acrylic, fused silica [55] or Teflon have been tested and used by other groups, sometimes with some additional coating (Teflon, deuterated polystyrene or Fomblin oil). The following chapter describes in detail the research and development program that was accomplished in order to find better materials for the chamber (optionally also for the coating), optimize its performance and finally, as a consequence, achieve a considerable gain in experimental accuracy. After specifying requirements that must be fulfilled by the new storage chamber, the development steps are described. Since it was not clear at the beginning, whether it would be worthwhile to coat a chamber from inside with some additional layer (e.g. diamond or DPS), to some extent we tried to reach two goals:

- find the best insulating material, to be coated with some good neutron reflector

- find the best material both for neutrons and Hg, with acceptable electric properties and use it as it is

The outcome is summarized in two further sections, one of them describes the search for a good bulk insulating material, the other one concerns coating related issues.

5.1   Requirements

There is a number of stringent requirements on the properties of the EDM storage chamber material. First of all, a trap for ultra-cold neutrons should have high Fermi potential V_F. All the neutrons with kinetic energy higher than the Fermi potential of the chamber surface penetrate the walls and are lost after few seconds of storage. The world's most accurate value of nEDM was measured using simple fused silica

chamber with V_F of only 90 neV, leaving quite some space for improvements, see simulation results in Sec. 4.1.2.

Another parameter important in terms of neutron storage is the loss coefficient per wall reflection η, which is of the order of 10^{-4} for most materials used so far for this application. It describes the loss rate of ultra-cold neutrons trapped in the chamber, those, in other words, with kinetic energies lower than the V_F of the chamber walls.

Both aforementioned properties enter into the effective, energy dependent loss probability parameter $\mu(E)$ according to the Eq. 2.22 (see section 2.2), therefore losses during the storage period can be reduced by using materials with high Fermi potential.

The mechanism of the UCN losses due to the wall collisions is not theoretically explained in a sufficient way. For unknown reason the values measured experimentally are much higher than predicted (see p. 15). It is clear, though, that one of the most important loss contribution is caused by up-scattering and absorption (capture) mostly on hydrogen, which is always present on surfaces. Thus, the surface hydrogen concentration is to be controlled and kept on a possibly low level. Alternatively, deuterated materials could be used. A variety of other elements, including boron or ^{6}Li, have to be avoided for the same reasons.

Not only the number of UCN but also their polarization has to be preserved during the storage time, therefore the spin flip probability per wall reflection β ought to be not more than 10^{-5} and stable in time [69, Sec. 5.3], assuming pessimistically, that the depolarization can be correlated with the E-field direction (which is unlikely). Experimentally, this requirement is easily fulfilled [52]. Simultaneously it is necessary to achieve a reasonably long polarization lifetime for the mercury co-magnetometer and, as it turns out, some materials (Teflon, quartz) are much better in these terms than others (BeO). Thus, it is needed to balance both factors with respect to UCN storage time (typically 130 seconds) and find a material that would be good enough both for neutrons and for mercury.

Since the magnetic field inside the chamber has to be homogeneous and well under control, magnetic materials must not be used in the vicinity of the storage volume. Required field homogeneity ($\sim 10^{-3}$ on $10^{-26}\,e\,cm$ sensitivity level) makes it clear that any, even small, admixture of ferromagnetics (e.g. in some type of ceramics) is not acceptable.

Last but not least, both the chamber material and optionally the coating must be highly resistive, because the storage chamber is to be located between two high-voltage electrodes and leakage currents would disturb magnetic field stability and homogeneity, introducing dangerous systematic effects. Requiring the total leakage current to be below 1 nA constrains the chamber resistivity to $10^{15}\,\Omega\cdot cm$ or more. If the coating thickness is of the order of 10 microns, its lowest acceptable resistivity will be around $10^{12}\,\Omega\cdot cm$. Besides, one should keep in mind that while the experimental accuracy is proportional to the square root of number of counted neutrons, it is linearly dependent on the high-voltage value. So, on top of the resistivity requirements comes the question of dielectric strength of the entire trap, its stable operation up to 20 kV/cm and its resistance for high-voltage breakdowns, flashover discharges, treeing, tracking, etc. The inner surface of the chamber, whether coated or not, should

be also resistant to oxygen discharge cleaning, a standard procedure used regularly to improve the Hg co-magnetometer performance.

5.2 The insulating chamber

In order to find an optimal material for the chamber wall and improve its performance, as compared to the fused silica chamber used up to now, tests were done with a selection of materials. The first natural candidate was Si_3N_4, since it was a recommended substrate for CVD diamond coating. Later, when difficulties related with this type of ceramics were encountered, also other materials were taken into consideration; eventually, we focused our efforts on thermoplastic polymers.

Table 5.1 contains some general physical properties of materials tested, with exception of the two last ones (^{58}Ni and BeO), which were not investigated and are shown only for the sake of comparison. The coefficient of thermal expansion (CTE), is given there as one of the parameters important for CVD coating: the difference between substrate and coating should not be too large in order to prevent delamination or cracking of the deposited film when cooling down the material after deposition at more than 700°C. The dielectric constant is indirectly related with the flashover voltage, as smaller ε would improve the high-voltage stability and homogeneity of the electric field inside the chamber (see [71, Sec. 7.1], [72]). It is worth mentioning, that ^{58}Ni and BeO shown as a reference, which are among the best neutron reflectors available, cannot be used for our application: nickel because it is conductive and ferromagnetic, BeO because of its high toxicity.

In the table, one can distinguish several groups of materials:

- two types of Corning quartz glass[1], with good electrical properties and relatively low V_F, though, presumably suitable for CVD coating

- sintered ceramics such as Si_3N_4[2], AlN[3] and Al_2O_3, frequently used as electrical insulation and with considerably higher V_F, also possible to be coated using CVD technique and with more suitable CTE than quartz

- some more types of ceramics: $MgAl_2O_4$ and exotic (and more expensive) Y_2SiO_5, $Y_3Al_5O_{12}$ [73][4]

- thermoplastic polymers with good insulating properties: PS, PE, PMMA, PC

---

[1]Docter Optics GmbH, Greizer Strasse 62, 07907 Schleiz, Germany.
[2]More exactly: 90% Si_3N_4, 6% Al_2O_3, 4% Y_2O_3. Obtained from FCT Ingenieurkeramik GmbH, Gewerbepark 11, 96528 Rauenstein, Germany.
[3]ANCeram GmbH, Esbachgraben 21, 95463 Bindlach, Germany.
[4]Fraunhofer IKTS, Winterbergstrasse 28, 01277 Dresden, Germany.

Material	Name	V_F [neV]	ε	$U_{br.}$ [kV/cm]	CTE [10^{-6}/K]	R [$\Omega \cdot$ cm]
Si_3N_4	–	171	10	170	3.2	$\sim 10^{14}$
AlN	–	160	9	100	4.5	$> 10^{14}$
Al_2O_3	sapphire	138	9.3	146	8.8	$> 10^{14}$
Corning 7972	ULE glass	94	3.8	300	<0.03	$10^{11.6}$
Corning 7980 5F	quartz	94	3.8	300	0.5	$\sim 10^{10}$
Y_2SiO_5	Y-monosilicate	118	3.1	–[a]	6	–[a]
$MgAl_2O_4$	spinel	145	8.3	–[a]	8	–[a]
$Y_3Al_5O_{12}$	YAG	132	6.9	–[a]	5.5	–[a]
C	diamond	304	5.7	10^4	1.3	10^{9-16}
PMMA	plexiglas	120[b]	3.5	140	50 – 90	10^{15}
PS	polystyrene	170[b]	2.5	300	50 – 83	10^{17}
PE	polyethylene	209[b]	2.25	370	68 – 90	10^{17}
PC	polycarbonate	164[b]	3.0	380	68	10^{17}
BeO	beryllia	257	6.7	140	6.4	$> 10^{14}$
^{58}Ni	–	346	–	–	–	–

[a] No data available.
[b] Calculated for deuterated polymers.

Table 5.1: General physical properties extracted either from data sheets provided by the material producers or from available material databases [74], where: V_F - Fermi potential, ε - dielectric constant, $U_{br.}$ - dielectric strength, CTE - coefficient of thermal expansion, R - resistivity.

In most cases first the resistivity and dielectric strength was measured, then test diamond coatings would be deposited on small samples and the composite tested again for electric properties. Independently, neutron and Hg compatibility of chosen materials was measured at ILL Grenoble. For the thermoplastic polymers instead of diamond coating, possibilities to coat them with deuterated polymers were successfully studied.

5.2.1 Electric tests with small samples

The electric properties of the chamber wall material are essential for the experiment because of the stringent limit for leakage currents and the high electric field gradient foreseen in the system (>15 kV/cm). Both types of properties were measured with small samples using a high-voltage vacuum chamber. In the following section the setup used for tests and standard methods of high resistivity measurements are described first, then some information about high-voltage breakdown, especially flashover is presented. Finally, the results are shown.

5.2.1.1 Setup

Figs. 5.1 and 5.2 demonstrate the scheme and a picture of the apparatus that was used for tests. In the vacuum chamber, shown in the photograph, one can see a
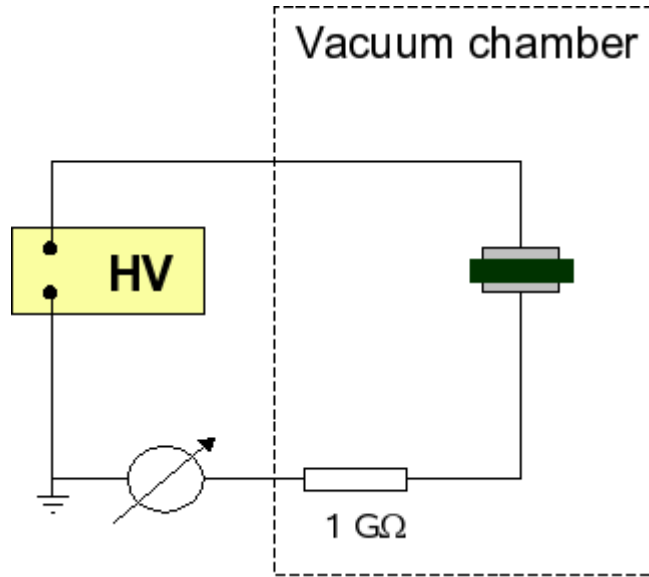
Figure 5.1: The simplest setup for resistivity measurements.

typical sample (Si_3N_4) with electrodes attached, mounted on a PVC support structure. Vacuum quality was monitored on a full range gauge connected to the system. Measurements were typically done at 10^{-5} – 10^{-4} mbar pressure. In all configurations high-voltage is provided to the electrode with a special BNC cable, entering the chamber via a vacuum-tight high-voltage feedthrough. On the ground side, the signal from the ground electrode enters the ammeter after passing a limiting resistor (R=1 GΩ, blue in the picture). Some pieces of Teflon insulation are used around critical parts of the circuit. Concerning the external readout and the high-voltage power supply, different arrangements were used for resistivity and dielectric strength measurements. Both configurations are described below in corresponding sections.

5.2.1.2 Resistivity measurements

Resistivity, called also volume resistivity, ρ, expressed in $\Omega \cdot$ cm, is determined by measuring resistance, then converting to (volume) resistivity, by taking geometric considerations into account. Surface resistivity, ρ_s, sometimes also an important property, is addressed in more detail in Sec. 5.3.3.2, where the characterization of the coatings is described.

The most obvious way to measure the resistance of a sample is to employ Ohm's law,

$$R = \frac{U}{I} [\Omega],$$

and measure the resulting current while a known potential difference is applied. Since our main interest is in highly insulating materials, with resistivities better than 10^{12} $\Omega \cdot$ cm, and given the voltage limit of the available power supply, measured currents are in the regime of picoampers and below. Such a measurement is not trivial and requires a well shielded, stable setup equipped with an accurate picoammeter.
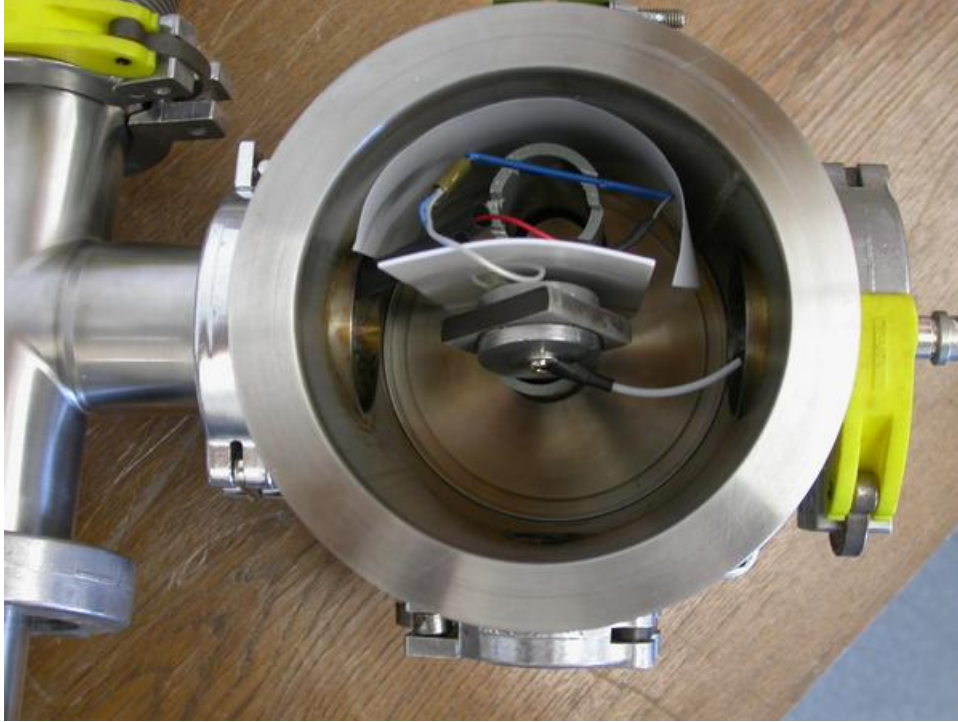
Figure 5.2: Setup for the electric tests: the vacuum chamber.

The simplest arrangement shown in the Fig. 5.1 employs exactly this idea, realized using a rectangular or cylindrical block of insulator with electrodes on the either ends. The additional resistor serves as a protection for the picoammeter in case of a high-voltage breakdown. Then the resistivity is related to the measured resistance R between the electrodes by

$$\rho = R\frac{A}{l}[\Omega \cdot \mathrm{cm}],$$

where A and l are the cross-sectional area and the thickness of the sample between the electrodes, respectively. When doing a proper measurement of a high resistance, leakage of current via paths other than a direct one across the sample becomes a problem. It happens often that some dirt or moisture accumulated on surfaces can provide a low-resistance route and affect measured resistance. One of the standard ways to overcome the difficulty is to use on the specimen an extra guard electrode, that would collect any leakage current over the surface and prevent it from being measured (see Fig. 5.3). But this method can also become a bit problematic, namely, when the sample resistance is very high, it can only be determined by measuring with an electrometer the voltage drop across a standard high resistor R (see Fig. 5.3 on the right). For more information see [76, Sec. 2] or [75, Sec. 5.7].

The most stable and reliable resistance measurement method, 4-point technique is described in detail in Appendix A. However, for highly resistive materials the four point contacts become incapable of injecting currents high enough to obtain meaningful results. To make it even worse, the necessary input resistance of the voltmeter must be greater than the resistance between the measuring tips, otherwise
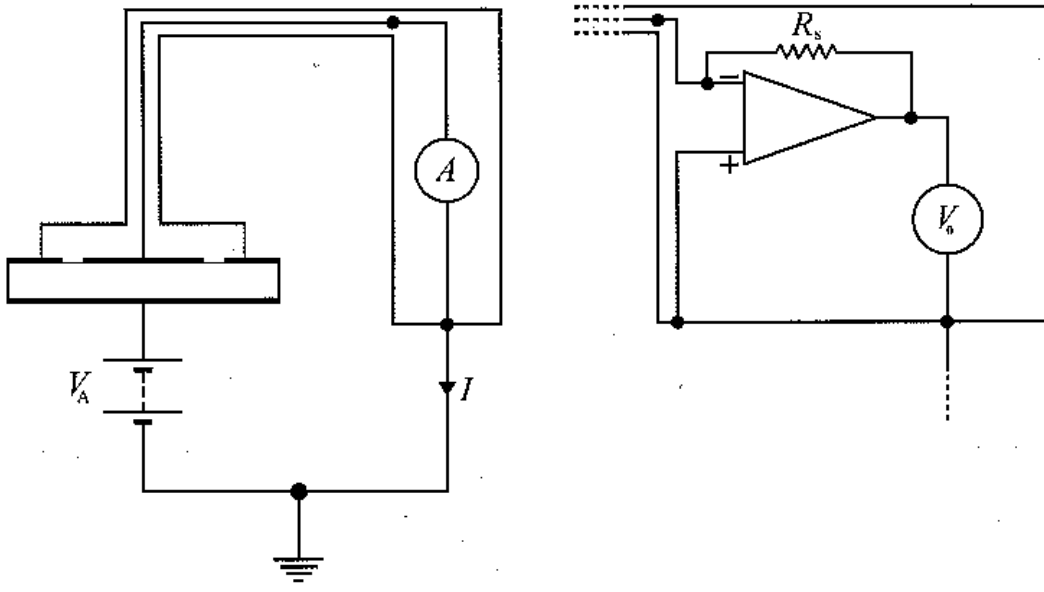
Figure 5.3: Circuit diagram for resistivity measurements by the 2-terminal method with guarding (from Ref. [75])

the current would simply bypass the specimen via the voltmeter. In a similar way, using only small electrode tips, one can use also 2-terminal methods. The problem of insufficient resistance of the voltmeter can be avoided, being replaced by the difficulty to control the exact contact area and resistance. Again, using the Laplace's equation one can derive the resistance between two hemispherical electrodes in contact with semi-infinite sample, as shown in Fig. 5.4(a), neglecting contact resistances [75, Eq. 5.54]

$$R = \frac{\rho}{\pi r_0} \quad (r_0 \ll d). \tag{5.1}$$

The result does not depend on electrode separation, indicating that the major part of the voltage drop occurs in immediate vicinities of the tips of the electrodes, which makes the outcome very sensitive only to the small sample of the material at electrode tips. That clearly affects accuracy and reproducibility of measurements.

Another configuration of similar type, with two circular electrodes is demonstrated in Fig. 5.4(b), this time the dependence on the electrode separation enters the formula

$$R = \frac{\rho_s}{\pi} \cosh^{-1} \frac{d}{2r_0}. \tag{5.2}$$

And also in this configuration measurement will be over-sensitive to the precision contact.

However, our goal is to simulate in small scale, but as realistically as possible, the experimental environment of the nEDM spectrometer. Thus, we should keep in mind, that the final application of chosen material will be an insulating cylinder located between two high-voltage electrodes. For such a configuration surface currents cannot be completely eliminated and since we are more interested in learning
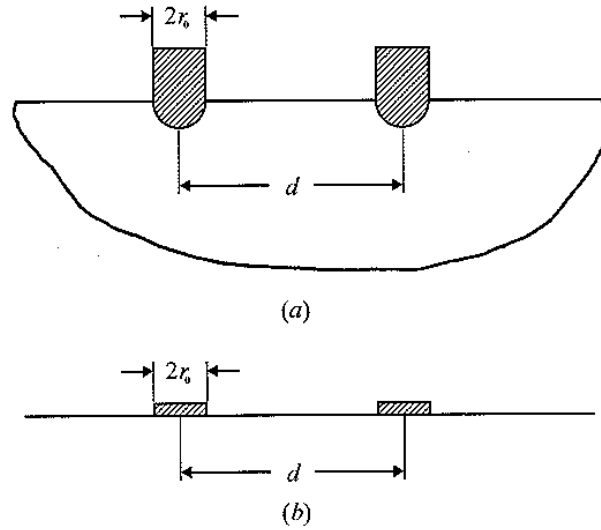
Figure 5.4: Types of 2-terminal probes: (a) hemispheres in a solid (b) discs on a surface

something about the effective resistivity than about the intrinsic material constant, it was decided to measure using the simple unguarded 2-electrode circuit, as shown in Fig. 5.1. In order to remove as much surface conductivity as possible and at the same time to reproduce normal experimental procedures of nEDM measurements, insulator samples were always carefully cleaned using ultrasonic bath: with acetone, ethyl alcohol and finally with demineralized water. To provide a good electrical contact, after cleaning and drying, thin cylindrical aluminum electrodes (20 or 30 mm diameter) were fixed to a sample with conductive glue[5], consisting of silver paste mixed with some hardener based on epoxy resin. In some cases, described later (see p. 60), only a layer of glue without a metal electrode was used. The glue requires some period of hardening at higher temperature, so typically, samples were baked in an oven for 1-2 hours at $60 - 100$ °C, as recommended by the producer. All the measurements on the samples prepared in such a way, were performed in vacuum of similar quality as the one available at the nEDM storage chamber ($\sim 10^{-5}$ mbar).

Concerning the readout electronics, for initial resistance tests a multimeter capable of measuring 200 GΩ was employed (Keithley M2000), equipped with standard set of probes. Samples with resistivities beyond that range were examined with a picoammeter and in vacuum. The vacuum chamber is closed with a stainless steel flange that acts as a Faraday cup, thus providing additional shielding and improving the stability and accuracy of the resistance measurements. The signal from the "zero" electrode is transmitted using a special double shielded triax cable, in order to reduce noise. The picoammeter (Keithley M6487) contains also a stable voltage source (up to ±505 V). This feature was used for the *alternating voltage method* (see [76, Sec. 4.4.2], [77, Sec. 3.21]), one of the built-in functions of the picoammeter. It was routinely used for estimating the resistance of the bulk insulator samples. The

---

[5]EPO-TEK® E4110 from Epoxy Technology, Inc. (www.EPOTEK.com)

general principle of this method is based on taking two current measurements – one at a user-specified test voltage and one at 0 V. By determining the current difference that results from the step voltage, it is possible to suppress the effects of background current. The accuracy claimed by the producer of the ohmmeter for this range of resistivities, is supposed to be less than 10%. Due to external noise and instability in the readout, it was possible to reach 10% accuracy only in really optimal conditions, verified after many repetitions of alternating voltage measurements.

5.2.1.3 Dielectric strength

Dielectric strength is defined as the maximal voltage that an insulating material can stand without a breakdown. However, as pointed out in [78, Sec. 8.2], "there is no direct experimental way of knowing whether an observed breakdown is or not is intrinsic, so the concept necessarily remains an ideal one, to be identified in practice only as the highest value (for a given material) obtainable after all known secondary effects seem to have been eliminated". And following the Ref. [71, Sec. 2.1], the secondary effects can be related with the choice of electrode system configuration, electrode material and treatment technique, method of voltage application, temperature and pressure, frequency of electrode and dielectric medium replacement, sample dimensions and geometry, quality of electrode contact with the dielectric, choice of the medium in which tests are performed and even data processing algorithm.

Literature values for dielectric strength given in Tab. 5.1 were supposedly measured as close as possible to the ideal, intrinsic dielectric strength, understood as a material constant. Comparing values from the table with the nEDM requirement (>15 kV/cm), it seems that any of the tested materials is actually much better than necessary. This is not the case, though. Again, just like it was in the case of resistance, the limiting problem is geometrical configuration coupled with surface effects. Therefore, instead of trying to re-confirm "intrinsic" dielectric strength of the insulators, it was more important to find their effective limit for high-voltage.

Concerning the geometrical configuration, it is not a straight-forward procedure to extrapolate dielectric strength measured using a small scale model to full size apparatus. For a breakdown voltage a non-linear scaling can be found (see [71, Secs. 6.2–6.4]), that depends on the size of the gap between the electrodes, their area and the total volume of dielectric confined in between. For instance, the dependence of the breakdown voltage on the inter-electrode gap can be written

$$U_{br} = K d^a, \tag{5.3}$$

where d is the gap size; K and a are constants that depend on the medium and exact conditions. K can vary significantly, while a is confined to the range between 0.4–0.7 and typically equals 0.5. A similar empirical scaling law can be formulated for the dependency on electrode area

$$U_{br} \approx S^{-n}, \tag{5.4}$$

where S stands for the area and n is again an electrode dependent factor, in most of the cases in the range 0.05 (Al_2O_3) – 0.1 (steel). In addition to this, the dielectric

strength is inversely proportional to the volume of the dielectric. Numerous experimental data confirms this phenomena, however the rate at which U_{br} decreases with increasing volume varies significantly, so a consistent empirical formula has not been formulated.

But the biggest and, in fact, the limiting problem in terms of HV stability is the so-called *flashover* voltage, U_{fl}, defined as the voltage at which an unintended high voltage electric discharge over or around an insulator surface occurs. The insulator itself is not damaged by flashover, no permanent conductive paths are created across its surface (this would be the case for *tracking*[6]). There are several factors that can affect flashover voltage, the most important ones are the character of electrode contact with an insulator, its orientation relative to the electric field lines and dielectric properties of the solid insulator and ambient medium. The following empirical formula attempts to summarize this dependence [71, p. 172]

$$U_{fl} = k \left(\frac{\Delta}{\varepsilon} \right)^{0.45} \left(\frac{l}{l_0} \right)^{0.2}, \tag{5.5}$$

with k being an empirical constant, Δ thickness of the dielectric, ε the dielectric permittivity of material. The meaning of l and l_0 lengths from the formula is explained in Fig. 5.5. One can conclude, that higher U_{fl} is achieved in arrangements with surfaces parallel to electric field lines. Another important observation is that insulators with smaller surface capacitance C_{sp} (thus smaller ε) perform better,

$$U_{fl} \sim C_{sp}^{-n}, \tag{5.6}$$

which is easy to understand: higher capacity can accumulate more charge, which can later feed the flashover discharge.

Remaining conditions, such as the insulator surface quality and the character of the junction with electrodes are not discussed here in detail, for more information see [71] or [72].

All tests have been performed using the setup described in Sec. 5.2.1.1 on the same samples that had been prepared and used before for resistivity measurements, for details of sample treatment see Sec. 5.2.1.2. All the results are summarized in the following section.

5.2.1.4   Results

As shown in Tab. 5.2, ultra low expansion quartz glass (Corning 7972) with a specified resistivity close to 10^{17} $\Omega \cdot$ cm happened to be the most resistive material of all tested. Sapphire and normal quartz glass (Corning 7980) are slightly worse. Si_3N_4 is more or less an order of magnitude less resistive. The lowest values, already close to the

---

[6]Tracking is one of the consequences of partial discharges in the insulator. The repetitive discharges eventually cause permanent chemical changes within the affected dielectric. Over time, partially conducting carbonized trees are formed. This exerts greater stress on the remaining insulation, leading to further growth of the damaged region, resistive heating along the tree, and further charring. This eventually culminates in the complete dielectric failure of the insulation.
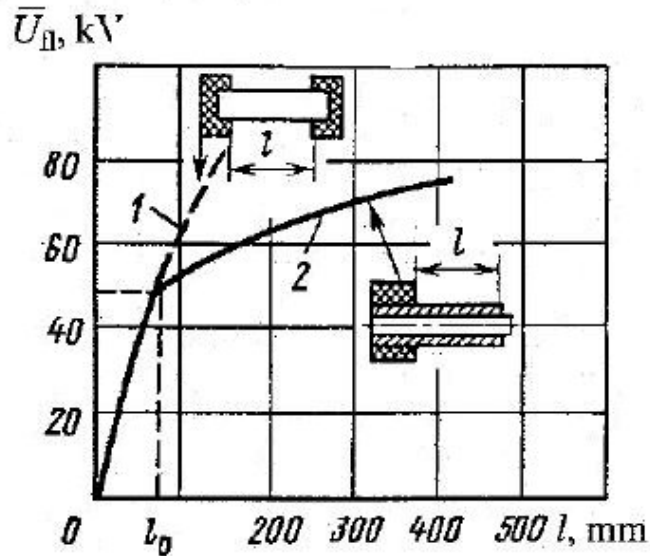
Figure 5.5: Dependence of U_{fl} on flashover path length of solid insulation in air for configurations with dominant (1) tangential or (2) normal electric field components (from Ref. [71]). For small distance l between the electrodes (up to l_0), curves for both arrangements with prevailing normal and tangential components of the electric field vector coincide. For large l, the first configuration is characterized by a low rate of increase in U_{fl} with increasing l.

minimum of 10^{15} $\Omega \cdot \text{cm}$ required for nEDM experiment, have been measured for AlN. All the materials seem to be acceptable, at least in terms of the resistivity, but to be on the safe side those which are only slightly better than it is necessary, should not be seriously taken into account. In case of AlN, the information obtained from the measurements was of greater importance and practically eliminated this substrate.

Concerning the setup for measuring $U_{br.}$, a transparent Plexiglas flange was used instead of the steel one, in order to be able to see possible sparks inside the vacuum chamber. Since in that case high voltage was much more important than accuracy, a separate high voltage source[7], achieving 12 kV, and a less accurate ammeter[8] were used. The described setup has an intrinsic limitation: even though the HV power supply could provide ±12 kV, it was impossible to make any reliable or reproducible tests for voltages higher than 10 kVbecause of sparking around the HV feedthrough insulation. All samples tested, in vacuum and after proper cleaning could stand the highest value without any dependence on its polarity. Given different sizes of the samples, namely different thicknesses and different area of electrodes, one obviously gets different results for all of them. Therefore, the results are to be understood only as lower limit for dielectric strength, however it is remarkable, that they are already sufficient for the nEDM chamber even as they are. It is important to keep in mind, though, that the electric properties do not scale linearly with the sample size, so large

---

[7]type HCL 35-12500 from F.u.G. Elektronik GmbH
[8]Keithley M485

scale tests are necessary for a reliable determination of $U_{br.}$ and ϱ.

Material	Resistivity $\rho\ [\ \Omega \cdot \mathrm{cm}]$	U_{br} [kV/cm]	Thickness [cm]
Si_3N_4	$5.9 \cdot 10^{15}$	17	0.6
AlN	$2.4 \cdot 10^{15}$	30	0.3
Al_2O_3	$11 \cdot 10^{15}$	25	0.3
Corning 7972 (ULE)	$71 \cdot 10^{15}$	21	0.5
Corning 7980 5F	$19 \cdot 10^{15}$	15	0.5
Y_2SiO_5	–	–	0.5

Table 5.2: Results of resistivity and dielectric strength measurements. Resistivities are given with 10% accuracy, U_{br} should be understood as a lower limit (see text). The sample area varied between $4\,\mathrm{cm}^2$ and $9\,\mathrm{cm}^2$.

5.2.2   Co-magnetometer compatibility

During the ILL cycle #144 the ^{199}Hg compatibility of Si_3N_4 was tested. More detailed information on the working principle of the ^{199}Hg co-magnetometer is given in Sec. 3.2.5 and 5.4.4, where the relevant tests for deuterated polymers can be found. For this short discussion it is enough to remember that the co-magnetometer is actually polarized vapor of ^{199}Hg atoms, which occupy the storage volume simultaneously with the UCN. The ^{199}Hg atoms polarization lifetime, τ_{Hg}, and the possibility to maintain the polarization on a high level for the entire storage time (typically 130 seconds) is essential for its operation. Mercury is depolarized mostly due to wall reflections and due to interactions with magnetic dipoles/polar molecules at the material surface. Some materials are better in that respect, some are worse. Unfortunately, with exception of the limited comparison given by May [55, Tab. 2.51], little is known from the literature.

The main idea of the test was to introduce a significant amount of Si_3N_4 into the storage chamber, covering the bottom electrode, and investigate its influence on τ_{Hg}. Seven $10 \times 10 \times 0.9\,\mathrm{cm}$ large Si_3N_4 plates were polished on the bottom side (to minimize the slit between the plates and the electrode) and thoroughly chemically cleaned and baked [79]. Cleaning was done first for 10 minutes in so-called "Piranha" mixture[9], then for another 10 minutes in mixture of $1\times H_2O_2 + 1\times NH_4 + 5\times H_2O$ at 70°C, for the next 10 minutes at the same temperature in $1\times H_2O_2 + 1\times HCl + 6\times H_2O$, and finally for half an hour in a buffer oxide etching solution (BOE) in a 9:1 ratio. This is a standard procedure used for silicon substrates. The plates were then baked at ~155°C in vacuum for 4 days and eventually vented with D_2O vapor and dry nitrogen. Finally, the Si_3N_4 plates were transported to ILL, put on the bottom electrode (as shown in Fig. 5.6) and the nEDM spectrometer was closed and pumped in the usual way.

It turned out that after introducing the Si_3N_4 plates to the chamber, τ_{Hg} dropped from ~30 to ~7 seconds. After removing the plates the polarization lifetime came

---

[9]$1\times H_2O_2 + 2\times H_2SO_4$
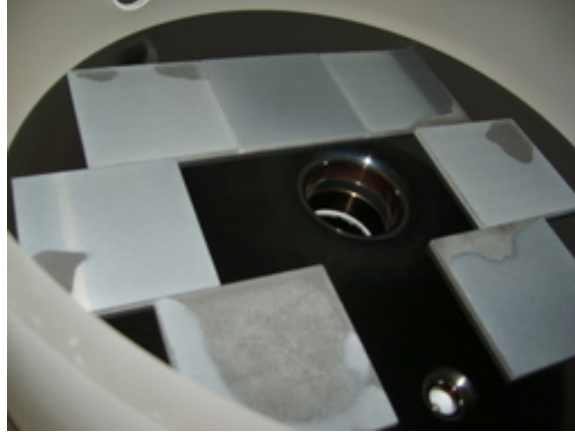
Figure 5.6: Si_3N_4 plates distributed on the bottom electrode surface. The picture was taken just before closing the chamber and performing the ^{199}Hg compatibility test (see text).

back to about ∼20 seconds, which is typically a minimal value observed with our setup (quartz insulator and DLC-coated electrodes).

Therefore, we concluded that Si_3N_4 depolarizes ^{199}Hg so much that it cannot be used for the insulating chamber, if uncoated. It remains, though, one of the options as the substrate for a diamond coated chamber.

5.3   Diamond coating

Diamond is considered to be possibly the best material for the nEDM chamber coating due to its high Fermi potential, high electrical resistivity and because it is non-magnetic. The Fermi potential of pure diamond is 304 neV, inferior only to ^{58}Ni (346 neV), however, because of the slightly smaller density of chemical vapor deposited (CVD) diamond within the top layer of the coatings, one should expect a correspondingly smaller, although still very promising, value of that parameter. Diamond-like carbon (DLC) coatings, used for the ultra-cold neutron source at Paul Scherrer Institut, can contain up to 95% of the diamond-like sp^3 phase, resulting in Fermi potential close to that of pure diamond. DLC is relatively cheap and easy to produce, unfortunately, there is one major drawback, which makes this material completely unsuitable for the nEDM storage chamber, namely, its resistivity is not high enough, due to a considerable content of the graphitic sp^2 phase. In principle, the resistivity and dielectric strength requirements (15 kV/cm) could be fulfilled with CVD diamond, since, as it was already reported in [80], film resistivities in the range $10^{11} - 10^{15}\,\Omega\cdot$cm should be possible to achieve, with a typical example of $5\cdot10^{12}\,\Omega\cdot$cm reported in [81]. The value is worse than for the natural diamond (up to $10^{16}\,\Omega\cdot$cm for type IIa [82]) due to the polycrystalline structure of CVD diamond, with large number of defects, smaller grain size [83] and effectively higher contribution of the surface conductivity.

Last but not least, we were aware that even with CVD diamond coatings one could

expect some problems, such as formation of conductive or semi-conductive layer on the substrate (see [84, 85, 86]), contamination of the diamond film during the process with a conductive admixture [87] or regeneration of a graphite-like surface on the coating [88]. In addition to this, there was quite some information available in the literature on CVD diamond resistivity measured *along* the film, but only very little about the same parameter as measured *across* its surface, which is crucial for our application, because of the risk of electric leakage between the HV electrodes. The latter property has been extensively studied only for completely different environment and for semi-conductive types of CVD diamond (especially doped e.g. with boron, see [89, 90]).

The difficulties mentioned above were the main motivation to study electric properties of CVD diamond on various substrates and to optimize CVD process parameters. It was planned to perform the tests first on a small scale and then, if the results would be promising, to proceed towards a fully diamond-coated insulator of the high-voltage chamber.

5.3.1   Chemical vapor deposition (CVD)

In general, chemical vapor deposition involves a gas phase chemical reaction occurring above a solid surface, which causes deposition onto that surface. Typically, as shown in Fig. 5.7, it requires thermal (hot filament), plasma (microwave, DC discharge) or a combustion flame activation of gas phase carbon-containing precursors (normally 1% CH_4 + 99% H_2).

To initiate diamond growth on non-diamond substrates (*heteroepitaxial growth*) one has to pre-treat them in a special way either by (1) mechanical structuring of the substrate surface or (2) 'seeding' with nm-sized diamond crystallites to provide sufficient number of crystallization centers. Then the substrates are put into the reactor, heated to the appropriate temperature and the gas mixture is introduced at a controlled rate. The chemical deposition process itself can be described in a very simplified way as follows (see Fig. 5.8). First, the plasma is created, using any of the techniques shown in Fig. 5.7. It consists partially of gas phase radicals: H and CH_3, which play here the essential role. Then, atomic hydrogen abstracts from the surface of the substrate, which is initially completely saturated with hydrogen, a H atom, forming H_2 and leaving a reactive gap behind. In most of the cases the gap reacts with another H atom, but sometimes, if it reacts with a CH_3 radical, a carbon is added to the lattice. A reaction between two chemically adsorbed methyl groups adjacent to each other locks them into the diamond lattice. Basically, one can consider the whole process to be catalyzed by excess atomic H. The resistivity of a coating can be influenced with proper doping, e.g. addition of boron turns diamond into a semiconductor, while appropriate addition of nitrogen can significantly enhance its resistivity [80]. However, if the nitrogen content is too high, the resistivity of CVD diamond decreases dramatically [91].
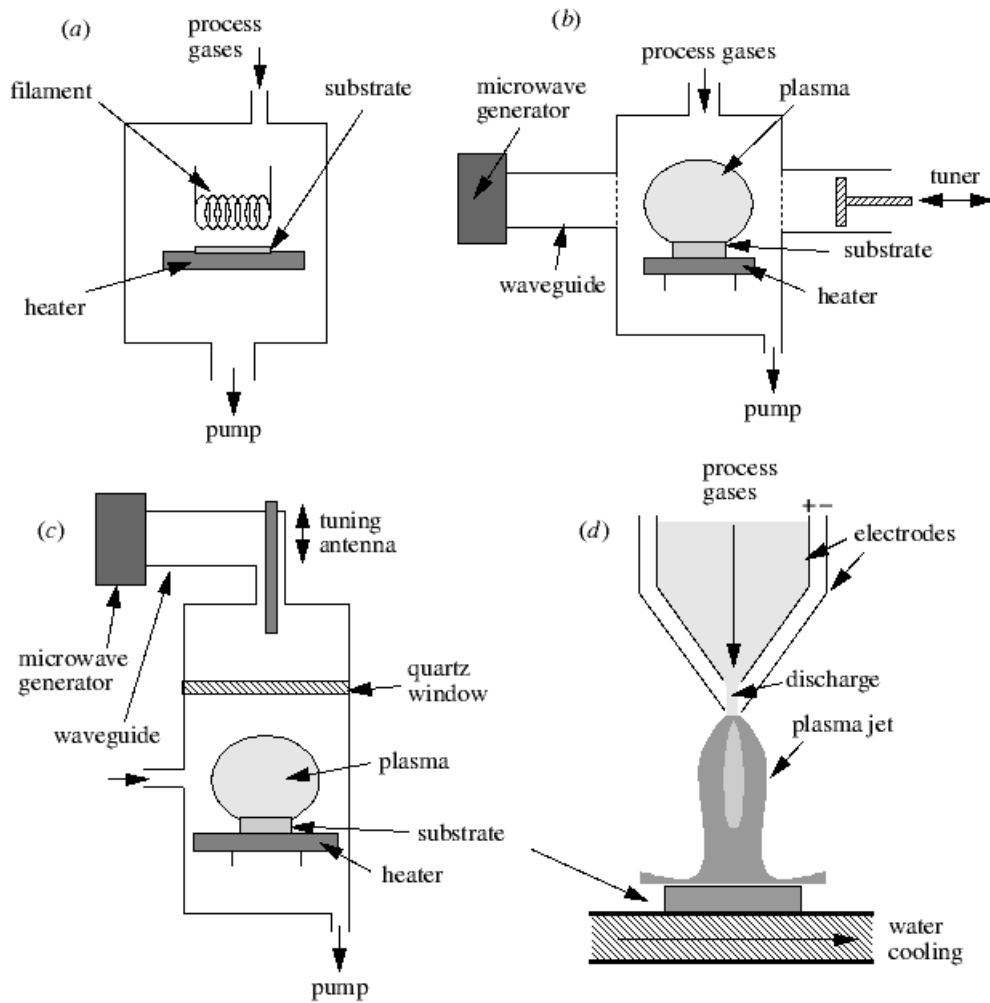
Figure 5.7: Examples of some of the more common types of CVD reactor (figure from Ref. [84]). (a) Hot filament, (b) 'NIRIM-type' microwave plasma reactor, (c) 'ASTEX-type' microwave plasma reactor, and (d) DC arc jet.
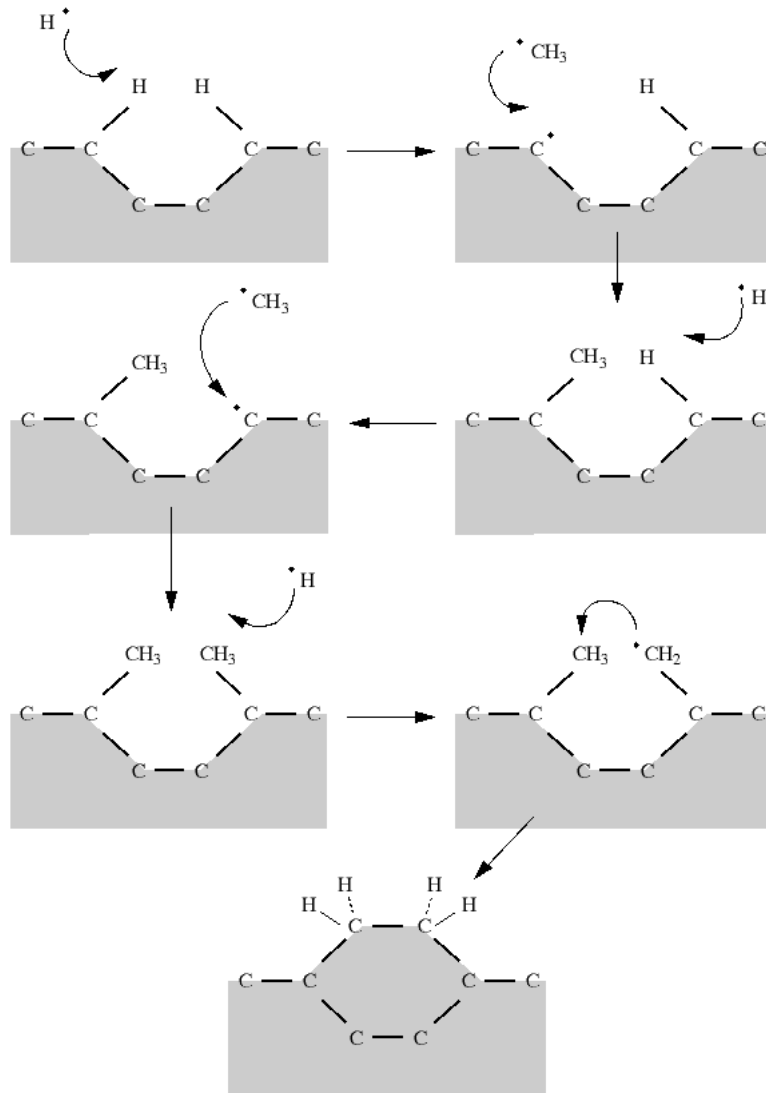
Figure 5.8: Mechanism of the chemical vapor deposition process (figure from Ref. [84]).

5.3.1.1   Hot filament CVD (HFCVD)

HFCVD is potentially the most suitable one for our application, because of its advantage in terms of scalability for the deposition over large area substrates [92] and the possibility to coat three dimensional structures [93], both features obviously necessary, with regard to the nEDM chamber size and geometry. It produces good quality polycrystalline films at a growth rate of 1 μm/h (strongly dependent on the exact conditions). That is why it was decided to experimentally test the feasibility of this technique for the nEDM chamber application.

Concerning the samples investigated (of the same type as had been used earlier for resistivity measurements), first they had to go through the standard pre-treatment, namely, nanometer-sized crystallites were embedded into the surface (diamond powder). Then the samples are put into the reactor, a few centimeters beneath the filaments, which are tungsten wires electrically heated to around 2200°C. The process gases (99% H_2 + 1% CH_4) are introduced into the chamber at controlled rates, in order to maintain the desired conditions inside. Since the hot tungsten filaments induce creation of atomic hydrogen, only the front side of a sample becomes coated with diamond, contrary to the other sides, which can get conductive, because of graphitic phases build up on the surface in absence of atomic H. This unwanted feature can be removed with mechanical polishing or sandblasting. Much more dangerous for the electronic properties are thin (in the range from 10 nm to 1 μm) layers of amorphous carbon or semi-conductive carbides built up between the substrate and the actual diamond [86]. Moreover, tungsten from the hot wire eventually also reacts with gas radicals and forms carbide, thus it is hard to completely avoid the contamination of the coating with the filament material.

The intention was to tune all the parameters of HFCVD process (temperature, gas mixture, substrates) in order to obtain the most resistive films possible. The sample coatings were prepared by Fraunhofer IST, Braunschweig [94], using a test reactor free of boron contamination.

5.3.2   Conductive interface layers

Since we found evidence for conductive interface layers, some literature-based introduction related with the topic is given below. Considering the chemical composition of the substrates containing Si, Al, Y and the CVD gas mixture (CH_4 + H_2), one can think about some candidates for the conductive phase, e.g. silicon carbide (SiC), pure Si or some unspecified amorphous or graphitic carbon phase. It is very unlikely that contamination with carbonized filament material (tungsten), normally present in the coating at the level of few ppm (by mass) [87], or some additional phases formed by metal oxides present in the substrate as sintering aids would cause such an effect.

5.3.2.1   Possible mechanisms

It is well known that carbide formation during the initial stages of CVD on substrate materials like Si, Mo, W and Ta precedes and accompanies the nucleation [85]. Some authors even claim that carbide can be considered as the glue, which enhances the

adhesion between the substrate and the coating and making carbide formation necessary to obtain an adherent heteroepitaxial coating. It is supposed to concern also non-metals, including Si-containing compounds such as SiO_2 and Si_3N_4 [84]. Others claim that also an intermediate layer of diamond-like amorphous carbon or graphite can play the same role, namely, relief the stress at the interface, caused by lattice mismatch or contraction. The thickness of such interlayers can vary from several angstroms, up to a few micrometers in extreme cases (Ti, Mo), with typical value of a few nanometers [85]. Some theoretical models propose formation of two interlayers on the substrate, first a carbidic one (SiC) and then an amorphous one (DLC) [95]. Some proposed mechanisms of the carbide layer creation assume that β-SiC[10] is formed from a thin layer of SiO_2, which inevitably covers the surface of Si_3N_4, others expect rather graded interlayers of SiC_xN_y [96]. In general, the literature concerning CVD on silicon nitride presents conclusions which are often unclear or contradictory and, in principle, there is no strong experimental evidence corroborating any of the models. A comprehensive summary of different approaches to the subject is given in [97], the general conclusions can be stated as follows:

- SiC can be formed on the interface at least for various process conditions and, when created, it strongly enhances adhesion of the coating [98]

- It is not clear whether an adherent coating can be produced without formation of a carbidic layer.

- Apparently, in some cases, the coating may grow from diamond 'seeds' rather than from the substrate, producing a negligible chemical bond at the substrate/coating interface and resulting in solely mechanical bonding mechanism.

5.3.2.2   Thermodynamic calculations

Thermodynamic equilibrium calculations are a standard tool used to estimate the rate of possible reactions of the substrate surface with the gas phase species and are widely quoted in the literature, also in the papers concerning specifically N_2-doped CVD [99, 100] or Si_3N_4 (one of our substrates [95]). When used properly, it can provide extremely helpful hints concerning the type of solid phases created and deposited during the CVD process. For this project, the analysis has been performed at Fraunhofer IKTS [101], using one of the commercially available codes (FACTSAGE with database FACT53 and SGSL, see Ref. [102]). It is worth mentioning that this type of modeling also has some intrinsic limitations, for instance, it does not take into account the real non-thermal property of the catalytically activated gas mixture; it is only assumed that the hot vapor acts solely as supplier of reactive species and that no kinetic barriers exist (which is normally the case at temperatures at which the coating process takes place).

Table 5.3 presents results of the thermodynamic calculations and shows what phases are built on different type of substrates at 0.01 mbar pressure in the atmosphere consisting of 50% H_2 and 50% CH_4 (molar proportions). One can conclude that

---

[10]β-SiC has the cubic crystal structure.

Substrate	Temperature range [°C]	Possible phases
Si_3N_4	500 – 850	Si_3N_4/ SiC, C
Al_2O_3	500 – 1000	Al_2O_3, Al_2CO, C
$MgAl_2O_4$	500 – 1000	$MgAl_2O_4$/Al_2O_3/C
$Y_3Al_5O_{12}$	500 – 1000	$Y_3Al_5O_{12}$, C, $YAlO_3$
$3Al_2O_3 \cdot 2SiO_2$	500 – 950	SiC, Mullit; Al_2O_3, C

Table 5.3: Results of thermodynamic calculations [101].

in the normal HFCVD conditions, thus without the nitrogen admixture, conductive or semiconductive layers can be expected on Si_3N_4 and presumably on other silicates such as SiO_2 or $3Al_2O_3 \cdot 2SiO_2$ (mullit), which is also quite interesting, since commercially available Si_3N_4 contains 6% Al_2O_3 and 4% Y_2O_3, which form intergranular glass phase. A similar result for slightly different deposition conditions (p=40 mbar) has been presented by Buchkremmer-Hermanns [95]. Therefore it seems that – although nobody has ever experimentally proven the presence of SiC layer after conventional low pressure CVD on this class of substrates – their creation is presumably inevitable. However, in different conditions, it does not have to be the case. As it was theoretically and experimentally demonstrated by Rozbicki [98] at atmospheric pressure (using combustion flame CVD) Si_3N_4 is thermodynamically stable up to 1350°C and a layer of β-SiC can be created only at temperatures exceeding this limit. On other substrates (Y-monosilicate, YAG and sapphire) carbides are not to be expected even in standard low pressure conditions. It is impossible to conclude, though, from equilibrium calculations, whether some kind of conductive graphite or amorphous carbon layer could be created or not.

The presence of nitrogen in the gas mixture during the deposition processes (performed for this work) completely changes the situation. Fig. 5.9 shows a phase diagram for a system of Si_3N_4, SiC and C at gas mixture with admixture of some N_2 [101]. Nitrogen shifts the equilibrium in such a way, that the thickness of the hypothetical SiC layer would be reduced; the higher its partial pressure, the more difficult is the formation of the carbide. Therefore, varying the N_2 pressure within the range, where the CVD diamond deposition is possible might be a good means to avoid the conductive interlayer.

To conclude, according to thermodynamic calculations there is a way to vary the CVD process parameters, either changing the temperature and pressure or the composition of the gas mixture, in such a way that conductive carbide layers are not created. However, there is no information about possible graphitic or amorphous phases. Besides, given the fact that virtually no experimental evidence unambiguously corroborating the model simulations has been published, it is not clear either, whether the *equilibrium* state analysis can fully describe the entire complexity of a CVD process, involving the physics and chemistry of plasma, surface effects, etc. Nevertheless, it gives enough hope and motivation to study in detailed experimental way the properties of CVD diamond coatings and optimize them for the nEDM chamber application.
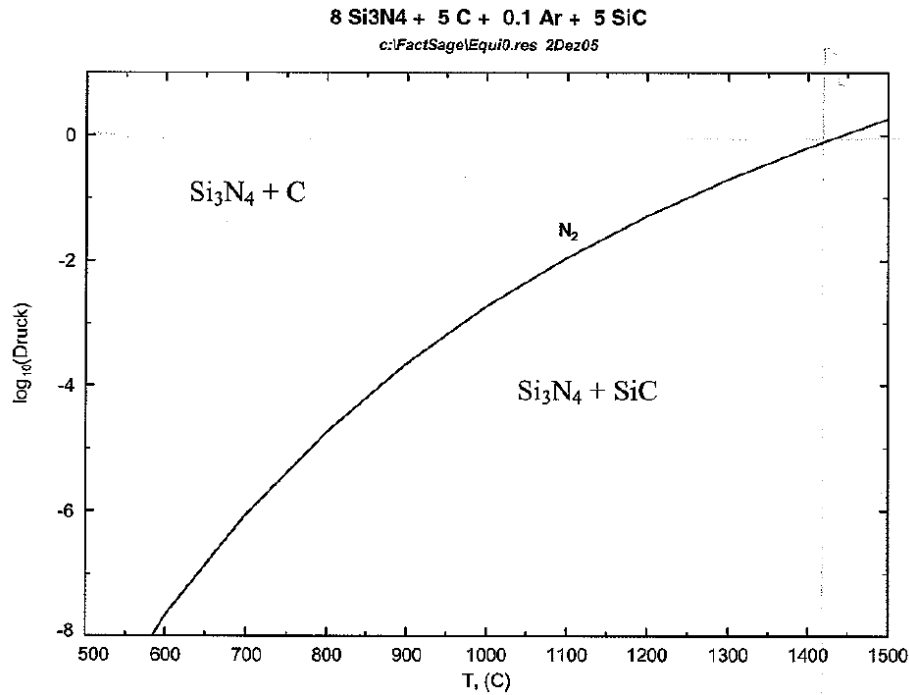
8 Si3N4 + 5 C + 0.1 Ar + 5 SiC

c:\FactSage\Equi0.res 2Dez05

Figure 5.9: N_2 partial pressure as a function of temperature for $SiC/Si_3N_4/C$ system [101].

5.3.3 Characterization procedures

5.3.3.1 Elemental composition

Hydrogen contamination   Before the regular tests with ceramic diamond-coated samples were performed, it had to be proven that surface layers of CVD diamond did not contain too much hydrogen. The hydrogen content is critical in terms of ultra-cold neutron loss and in order to reduce the UCN loss probability per wall reflection, one has to keep it on a low level. A standard experimental technique used for that purpose is elastic recoil detection analysis (ERDA) [103]. Thanks to M. Suter it was possible to perform the measurement at ETH Zürich using He ions from the tandem accelerator. Since only the surface was in the range of the measurement, we used a diamond coated silicon wafer as a sample. Because it was already shown [104] that DLC is a good UCN reflector, for the sake of comparison, we also examined two DLC-coated substrates (aluminum and stainless steel). In addition to this, mica standard was measured to provide the calibration ($\sim$9.5% at. hydrogen concentration). The results show clearly that the H content of CVD diamond is comparable with the one of DLC, it is even slightly better (lower), as visible in Fig. 5.10. Therefore, CVD diamond is a good candidate for storage applications with ultra-cold neutrons.

5.3.3.2 Electrical properties

An extension of the techniques used in Sec. 5.2.1 was necessary to estimate the insulating properties of HFCVD diamond. After a basic examination with a standard
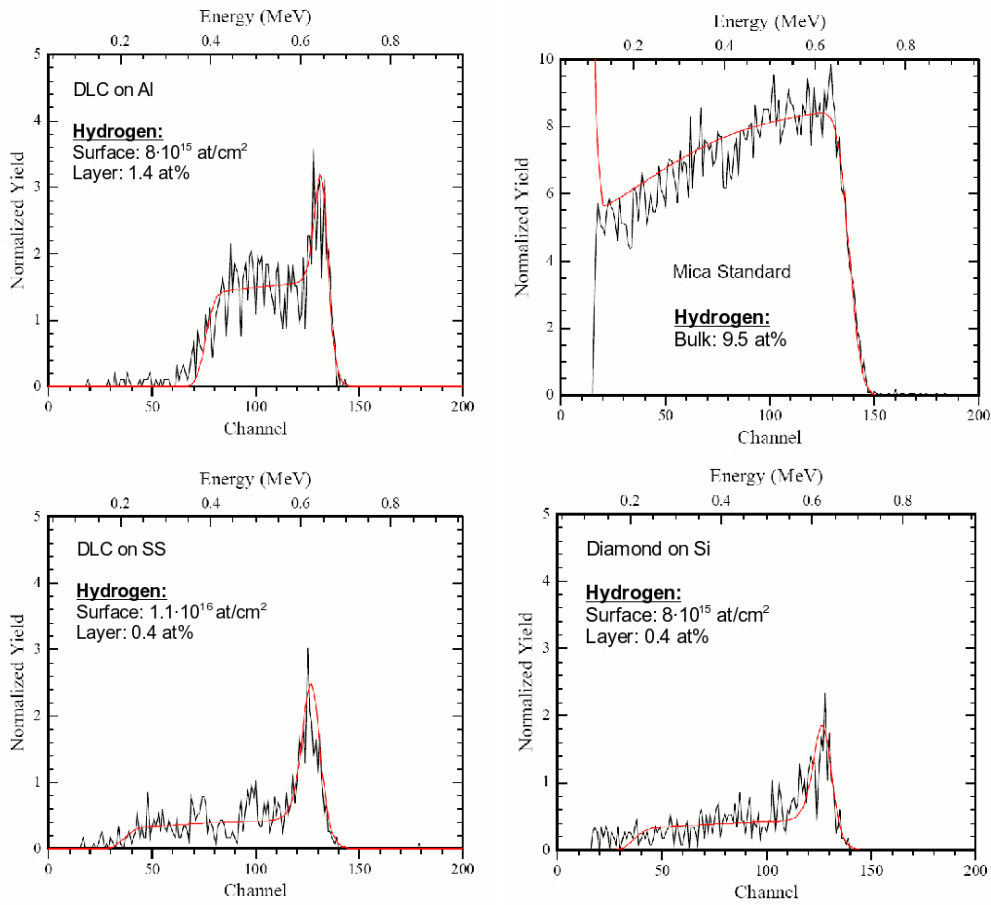
Figure 5.10: ERDA profiles of the hydrogen content in DLC (vacuum arc deposited ta-C) and CVD diamond coatings (see text). 10 channels correspond to 30 nm of depth. The hydrogen content reaches the maximum at the surface of the coating and then gradually decreases with the depth [105].

ohmmeter (up to 200 MΩ), those samples which revealed any conductivity (within the device range) were additionally treated to remove conductive surface layers. Once this was done with Corona discharge treatment (available in Fraunhofer IST), in the next step, remaining conductive (graphitic or amorphous) layers on the uncoated sides or the backside were mechanically removed with sandblasting or grinding. In order to clean the samples, they were washed with acetone and alcohol in an ultrasonic bath. Then, more accurate resistance measurements were done in vacuum, using the same setup as for the substrate tests (see section 5.2.1.1), but this time to measure the surface resistivity.

The *surface resistivity* ρ_s is a more appropriate parameter for characterizing current flow over a surface or a thin coating and is defined as the resistance between opposite edges of a unit square. Because of considerable amount of confusion present in the literature concerning that subject (see [106]), it is worthwhile to state clearly that the resistance across a square is independent of the size of the square [107] and

that the proper unit of surface resistivity is simply Ω. Since in reality a conductive surface must have some finite thickness t, what is actually measured is only an *effective* surface resistivity, which is related to the true (volume) resistivity of the layer by

$$\rho_s = \frac{\rho}{t} [\Omega]. \tag{5.7}$$

The simplest types of surface resistivity measurements require two electrodes in a few basic arrangements. One of them involves using two concentric ring electrodes and is very similar to the setup presented in Fig. 5.3, but now with bottom electrode used for guarding. The resistance R between the top concentric electrodes is then given by

$$R = \int_{r_1}^{r_2} \left(\frac{\rho_s}{2\pi r} \right) dr, \tag{5.8}$$

where r_1, r_2 are the radii of the inner and outer electrodes, respectively. Thus

$$\rho_s = 2\pi r \ln \left(\frac{r_2}{r_1} \right). \tag{5.9}$$

The serious problem in accurate measurements of resistivity is the contact resistance between the measuring tips and the sample. Even for very resistive samples high contact resistivity or non-ohmic character of the contact can bias the measurement. To reduce contact resistance one can evaporate or paint electrodes directly on the surface of the specimen using a suitable silver dispersion (that method was chosen), which gives much better effects than relying on pressure contact only.

Nevertheless, because of the anticipated very high resistance of diamond coatings it was decided to use a 2-terminal method. If the diamond is not resistive enough for the nEDM chamber application, then one does not have to care too much about the accuracy. On the other hand, if the resistivity is as high as it is required, it should be somehow estimated, which would be technically very difficult using 4-terminal techniques. Moreover, the problem of conductive interface layer under the diamond coating, which arose and had to be faced, made the interpretation of 4-point measurements of surface resistivity impossible (see Sec. 5.3.4). Therefore, the three following arrangements were utilized:

1. between both sides of the sample: to simulate the current flow along the composite, as in the planned high-voltage chamber, see Fig. 5.11(a)

2. between two small circular electrodes glued on the surface of the diamond coating: to measure the surface resistivity of the coating, see see Fig. 5.11(b)

3. between electrodes glued on two holes drilled through the coating with a diamond drill or blasted with grinding powder (carborund): to check on the conductive interface layer, see Fig. 5.11(c)

The voltage employed for the tests varied between 10 and 500 V, both polarities were used. Small circular electrodes glued on the coating (see Fig. 5.11) are essentially dried drops of the conductive glue, with a typical diameter of 2-3 mm and 10 mm
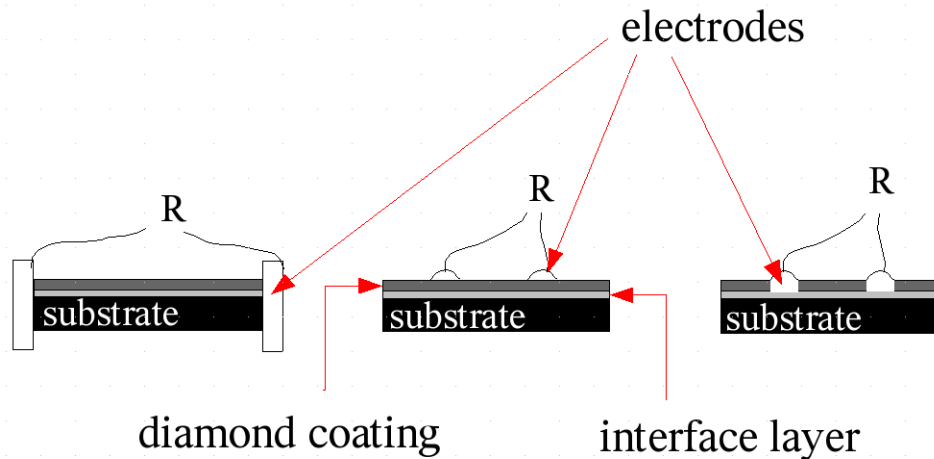
Figure 5.11: Three configurations used for the resistivity measurements (see text).

of spatial separation. In all cases the same two component epoxy-based glue was applied to contact the electrodes with the coating, each time after gluing the sample had to be heated in an oven for some time to dry the glue (typically 1 – 2 h at 60 – 100 °C). Some samples were prepared and measured more than once because of poor or questionable quality of electrical contact.

5.3.3.3   Structural analysis

Various experimental techniques have been employed to examine the samples. In most cases, first they were checked with scanning electron microscopy (SEM) and optical microscopy to get some information about the structure of the coating surface, its roughness and homogeneity, size of crystallites and potential pinholes. The thickness of the coating was independently estimated by means of electron backscattering measurements. With Raman spectroscopy it was possible to test the diamond quality and search for possible graphitic or amorphous impurities of the film. All Raman measurements were performed on a Dilor LabRam spectrometer, with the light at 632.8 nm produced by a HeNe laser (25 mW of power). X-ray diffraction (XRD) and grazing incidence diffraction (GID) measurements[11], provided additional information about the crystalline phases present in the samples. Finally, transmission electron microscopy (TEM) was used to identify accurately the composition of the substrate/coating interface. All these experimental methods are traditionally used for characterization of diamond and diamond-like coatings (see e.g. [86]).

X-ray Ray Diffraction (XRD)   The diffraction of electromagnetic radiation provides a class of methods for structural analysis of crystalline solids, including powder diffraction, the technique that was used for this work. Constructive interference of X-rays by the electrons within atoms arranged in a crystal structure of interplanar

---

[11]made with Seifert® XRD 3003 PTS-HR diffractometer.

spacing d, satisfies the diffraction condition according to the Bragg equation

$$n\lambda = 2d\sin\theta, \tag{5.10}$$

where n is an integer and λ the wavelength of radiation. In general, the position of the intensity maxima gives information about the size and the shape of the unit cell, whilst the width of the maxima can be used to evaluate the size, orientation and strain of grains in polycrystalline materials. Each crystalline solid produces its own line spectrum and both the positions (values of the scattering angle θ) and the intensity of the lines are characteristic of that particular phase and the pattern, thus providing a fingerprint of the material. Then it is already possible to perform an exact identification of the phases present in the sample.

Grazing incidence XRD (GID) uses small incident angles for the incoming X-ray, so that diffraction can be made surface sensitive. If one stays below the critical angle of the surface material studied, the radiation does not penetrate into the material and only an exponentially damped evanescent wave is established for a short distance (typically tens of Å) into the material. Therefore Bragg reflections are only coming from the surface structure. An advantage of GID is that the electric field at the critical angle is amplified locally by a factor of four, therefore the GID signal is stronger. In our case it means that the coating and the interface between the coating and the substrate are much better visible, exactly as it is desired in our case.

5.3.4 Results

The following section describes in detail all three HFCVD processes performed at Fraunhofer IST in 2006 and the characterization of diamond coated samples. Examination of each batch of the coated substrates is discussed separately, since the parameters of CVD reactions were varied (see Tab. 5.4). At the end, a separate section contains some additional information about the common problem of all the processes: a conductive interface layer under the diamond coating.

Process	$T[°C]$	$p_{N_2}[\text{mbar}]$	$t[\text{h}]$	Remarks
Test	900-950	$2 \cdot 10^{-3}$	36	ramping up in full gas mixture
I	650	$1 \cdot 10^{-3}$	40	2h at 610 °C and ramping up only in H_2
II	650	$2 \cdot 10^{-3}$	60	same as Process I

Table 5.4: Parameters of the CVD processes: T - substrate temperature, p_{N_2} - nitrogen partial pressure in the reactor, t - deposition time.

5.3.4.1 Test process

The first diamond coated Si_3N_4 samples were available for tests at the end of November 2005. The only change of the process, as compared with standard HFCVD procedure at Fraunhofer IST, was the addition of nitrogen to the gas mixture (99% H_2 + 1% CH_4), since it is known that diamond layers doped with N_2 reveal up to three

orders of magnitude higher resistivity (see e.g. [80]). The N_2 pressure inside the reactor reached $2 \cdot 10^{-3}$ mbar and the temperature of the substrate during the process was ramped up to $900 - 950°C$. The eventual coating thickness was between 8 and 9 µm.
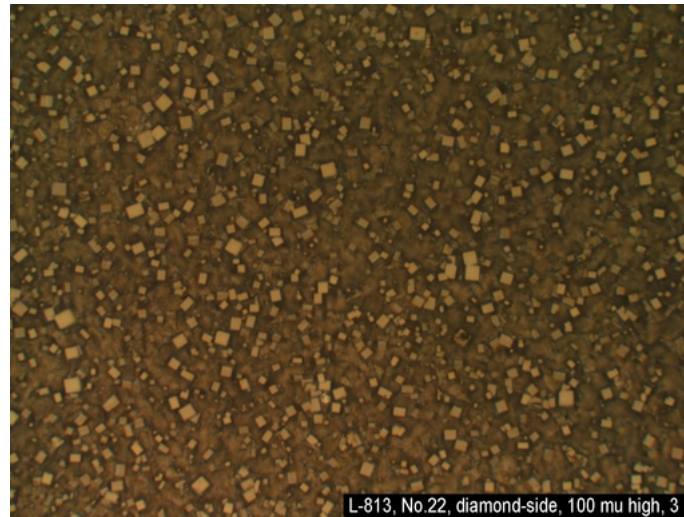

Figure 5.12: Optical microscopy, 100 µm side vertical extension.

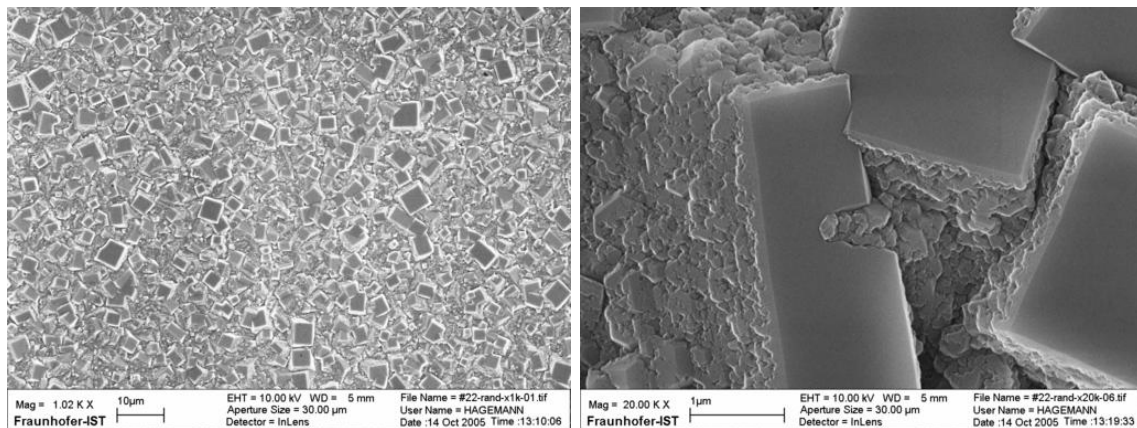Figure 5.13: Scanning electron microscope pictures: HFCVD diamond coating from the test process magnified 1000 and 20000 times, see also scale in the pictures

First, the coatings were examined with optical microscope, SEM and Raman spectroscopy to prove that the content of the sp^3 phase was sufficient. Figs. 5.12, 5.13 show the surface structure, with clearly visible and relatively large (up to several microns) oriented cubic crystallites. The ultimate proof of the diamond character of the coating is given in Fig. 5.14, because the presence of the line at 1332 cm^{-1} is a signature of high quality diamond (sp^3 fraction is practically 100%). The relatively large background under the 1332 cm^{-1} line is characteristic for Raman spectroscopy at visible wavelengths and largely disappears for the UV light.
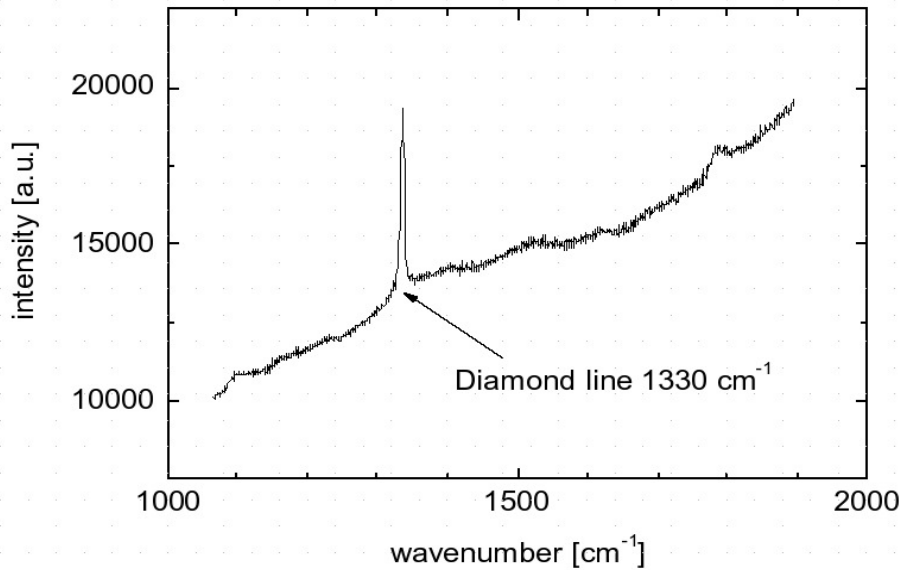
Figure 5.14: Raman spectrum of HFCVD diamond coating

Unfortunately, tests of electrical properties of the first samples were quite disappointing. As expected, the uncoated sides of the samples were conductive on the level of kOhms, however, even after the conductive phases had been carefully removed with sandblasting, the resistance measured between both sides of the sample (1st configuration, Fig. 5.11) was only 2 MΩ. At the same time, the resistance measured along the coating (2nd configuration) varied between 1.7 TΩ (for 10 V of applied voltage) and 68.5 GΩ (at 500 V). To check, if there was a conductive interface layer responsible for that inconsistency, two holes were drilled through the coating, electrodes glued into the holes to contact the possible interface and the resistance measured again (3rd configuration, Fig. 5.11c). The resulting resistivities of 32 MΩ (rectangular sample) and 22.5 MΩ (circular sample) confirmed the hypothesis of a conductive interface layer.

Also the aforementioned dependence of resistance on the applied voltage can be explained by the presence of the conductive layer. Since in such a situation the current flows mostly along the interface layer, the main voltage drop occurs across the actual diamond layer, which is only few microns thick. So, as it is shown in Fig. 5.15 (see also Ref. [108]), what is actually measured is not the *surface resistivity* of the coating, but directly the *(volume) resistivity*, given by a simple formula independent of electrode spacing (contrary to Eq 5.2)

$$\rho = R \cdot \frac{A}{t} \cdot \frac{1}{2} [\Omega \cdot \text{cm}], \qquad (5.11)$$

where, as before, t stands for the thickness of the insulator layer and A is area of the
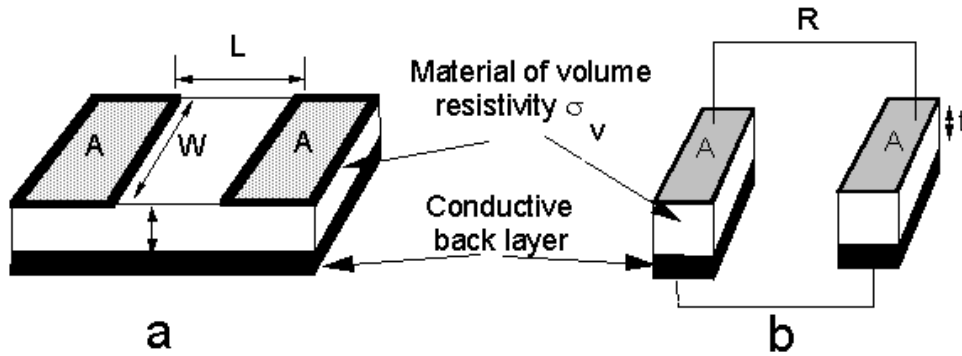
Figure 5.15: Conductive interface layer model and the equivalent circuit (from Ref. [108]).

electrodes. As a consequence, the electric potential gradient experienced by the diamond coating is very big and for voltages greater than 10 V ($10 \, V/10 \, \mu m = 10^4 \, V/cm$) it can already excess the effective dielectric strength of the coating, which, because of the polycrystalline structure of HFCVD diamond and especially the significant contribution of grain boundaries, may be lower than the value for natural diamond. The reduction of resistance at 500 V can be qualitatively explained as a partial HV breakdown.

Using our simple model we can try to estimate the resistivity of the insulating part of the coating. Assuming that the coating thickness is 8.5 μm with a maximal uncertainty of 0.5 μm, that the electrode diameter is 3.5 ± 0.5 mm and taking 1.7 ± 0.5 TΩ, which is the value of resistance measured at 10 V, one gets for the volume resistivity of the diamond coating

$$\rho = (9.62 \pm 5.58) \cdot 10^{13} [\Omega \cdot cm].$$

Therefore, a clear conclusion from the electrical tests was the existence of an unspecified conductive layer of unknown thickness between the (resistive) CVD coating and the resistive ceramic substrate. At the same time the resistivity of the diamond itself, estimated as shown above seemed to be promising and motivated the next step of research. According to the thermodynamic analysis prepared by Fraunhofer IKTS (see Sec. 5.3.2.2) one of the possible explanations could be formation of semi-conductive SiC interface at the initial phase of the process, because of too high temperature of the substrate. As it is shown in Fig. 5.9, the point corresponding to the test process parameters lies not far from the region where creation of the carbide is possible. Insufficient accuracy of the substrate surface temperature control, some fluctuation of the temperature at the initial phase of the diamond growth or some unspecified local phenomena at the surface might influence the thermodynamical balance and cause the problem. Another idea was that perhaps at the very beginning of the process, still at smaller temperature and with insufficient amount of H_2 in the gas mixture, some amorphous carbon phase could form on the substrate surface.
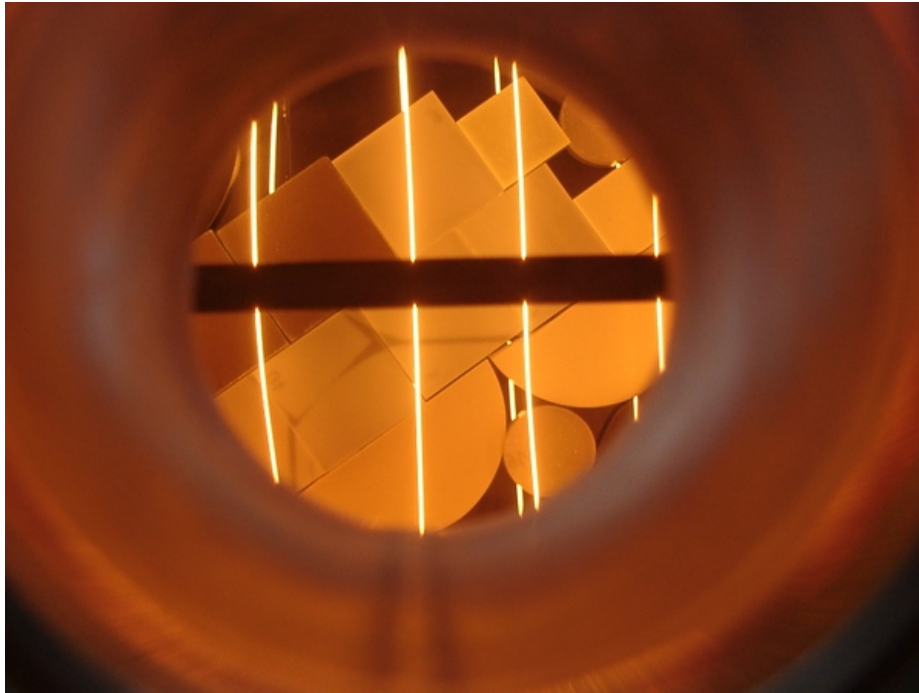
5.3.4.2   Process I

Figure 5.16: HFCVD process. The hot tungsten filaments are clearly visible above the substrates.

After the test process, in order to avoid the unwanted interface layer, it was decided to introduce a number of changes to the reactor and coating procedure. To lower the temperature and possibly solve the problem, the HFCVD reactor was modified, namely, the distance between the filaments and the substrate was increased. The substrates were kept for 2 hours at 610°C in pure H_2 atmosphere, then the temperature was slowly ramped up and at 650°C both CH_4 and N_2 were introduced. The hope was that the excess of atomic hydrogen during the initial phase of the process would etch away all graphitic or amorphous stuff and one could be sure that later, after ramping and admixing both gases, the actual CVD process would start in optimal conditions. The nitrogen partial pressure was kept so as not to impede diamond formation. The resulting growth rate was far from optimum for the CVD diamond growth (4 μm in 60 h). At the same time the N_2 content corresponded to a "safe" region in the phase diagram, much further away than before from the border between both phases, as shown in Fig. 5.9. Finally, eight new substrates were coated, on which from the thermodynamical point of view, creation of conductive or semi-conductive interfaces was possible to avoid. Two silicon wafers were also coated and utilized later for UCN transmission measurements.

The first thing observed after the deposition was that unfortunately the diamond film partially delaminated on 3 substrates (sapphire, YAG, $MgAl_2O_4$). Apparently the adhesion was not sufficient to prevent cracking of the coating during cooling down (see Figs. 5.18, 5.19). Therefore, all three materials were not taken into consideration
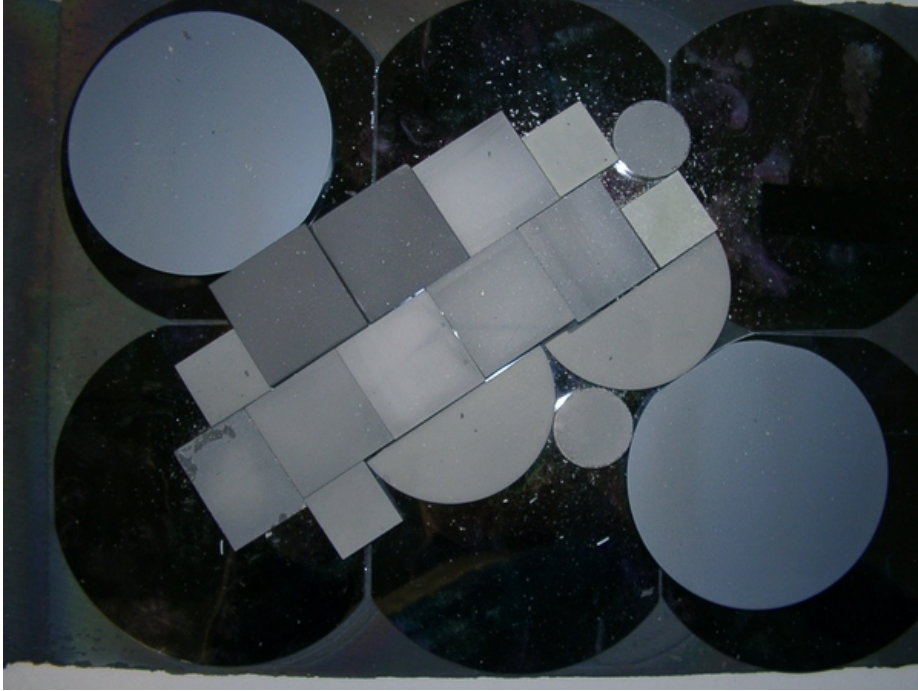
Figure 5.17: Diamond coated samples just after the HFCVD process, on some of them the coating has delaminated. White dust visible inside the chamber consists of oxidized parts of tungsten filaments and pieces of delaminated diamond film.
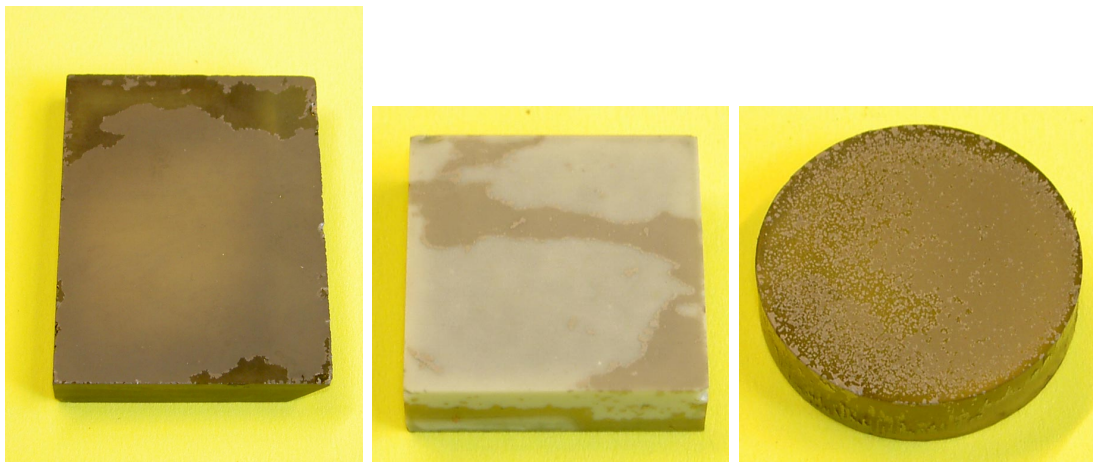

Figure 5.18: Delaminated diamond HFCVD coating, Process I. Starting from the left: sapphire (#8), YAG (#12), $MgAl_2O_4$ (#16).

for further tests. For the other samples, the coating thickness was measured with electron backscattering technique (using calibrated ^{14}C and ^{147}Pm sources) and was between 2 and 4 µm.

It was not the end of surprises. This time all the samples except one (#9), revealed a surface conductivity on a level of mega ohms (similar phenomena were described also in [109, 110, 111, 80]). As explained in the literature, surface conductivity of diamond
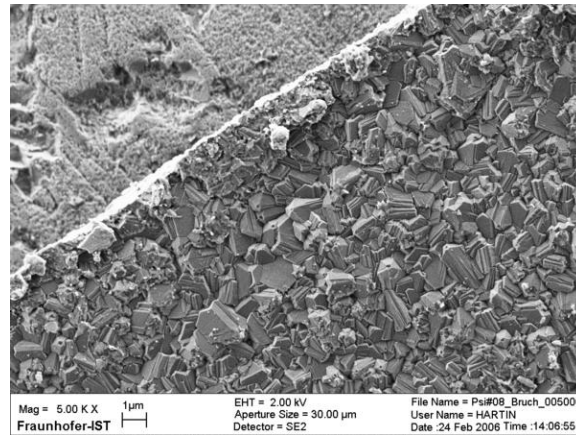
Figure 5.19: Delaminated diamond HFCVD coating, Process I. Sapphire (#8) magnified 5000 times with scanning electron microscope.

coatings is strongly related with the presence of dissolved hydrogen in the film and specifically by hydrogen-terminated bonds. It is not the only proposed mechanism, though, some authors also propose ideas based on space charge limited currents or on the characteristics of the coating morphology itself (for a review, see [112] and [113]). Fortunately, by various types of oxidation treatments the highly resistive diamond surface can be recovered, since no surface conductivity exists on oxidized diamond surfaces. To this end two methods were tried: corona discharge treatment (both in air and oxygen atmospheres) and thermal annealing. Discharge treatment was performed on half of the samples at the Fraunhofer IST after the CVD process, thermal annealing was tried later at PSI for the other half of the samples (baking for several hours at 400°C in an oven with air atmosphere). Both methods proved to be successful, except for both Si_3N_4 samples, on which corona treatment had almost no effect, and thermal annealing improved the resistance by only an order of magnitude, to about 80 MΩ. Nevertheless, the best value reached was not sufficient to perform further tests, i.e. to search for the conductive interface layer, which would have resistance very similar to the surface, making the entire investigation inconclusive. The hypothetical explanation of the (as compared to other samples) poor efficiency of Si_3N_4 oxidation treatments is tentatively related to its relatively high roughness. Examination with an optical microscope showed, that diamond coated Si_3N_4 had around 13 μm of height difference between "peaks" and "valleys" of the surface. For the other samples, the difference did not exceed $6 - 7$ μm. Assuming that the surface resistivity phenomena is caused by hydrogen present in top layers of the coating, one can speculate that higher roughness might have reduced the oxidation efficiency during the treatment (at the bottom of "valleys" and slits), which resulted in some residual conductivity.

Comparing the SEM pictures of process I coatings with those from the test process (Fig. 5.13), they look much different: crystallites are clearly smaller than before, more irregular and not oriented. Possibly, this can be explained by the low temperature of the process, much lower than optimum, which is beyond 800°C. Also the addition of
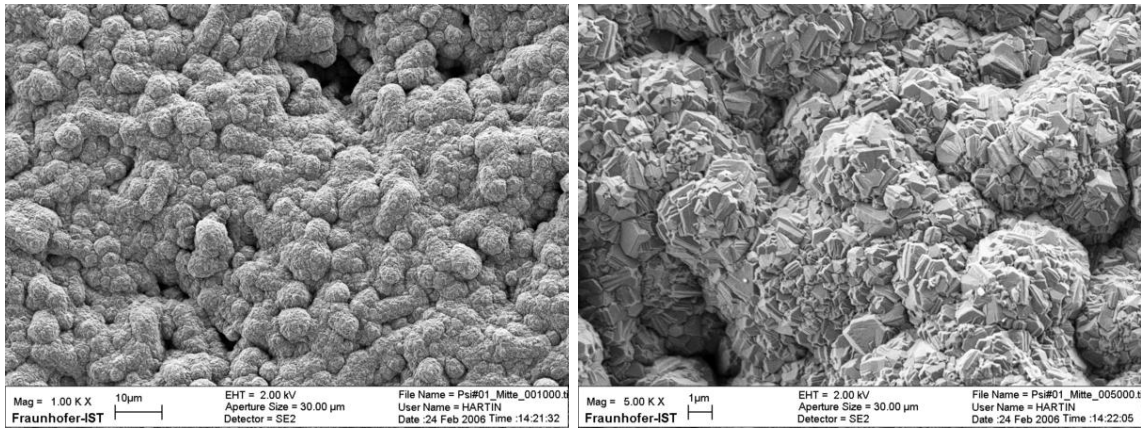
Figure 5.20: Scanning electron microscopy: Si_3N_4(#1, process I) magnified 1000 and 5000 times.
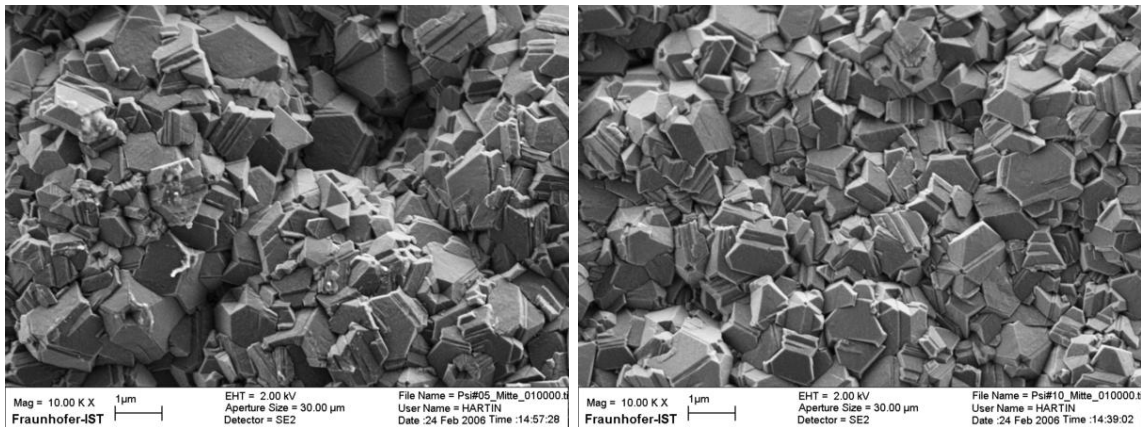

Figure 5.21: Scanning electron microscopy: ULE glass (#5) and Corning 7980 (#10) from the process I magnified 10000 times.

nitrogen can cause such an effect, as described by several authors (see e.g. Ref. [99]). Although during the test process the N_2 concentration was a factor of two higher, the growth rate was higher and high quality polycrystalline diamond was produced. Apparently, the optimal temperature for the diamond growth balanced the effect of nitrogen on the growth rate and the coating morphology.

Substrate	#	Corona	Annealing	$R_{surface}$ 10 V	$R_{surface}$ 500 V	$R_{interface}$	$\rho\,[\Omega \cdot cm]$
Si_3N_4	1	yes	yes	80MΩ		68MΩ	
	2	no	yes	30MΩ		30MΩ	
Y_2SiO_5	3	no	no	0.5MΩ		—[a]	
	4	yes	no	>200MΩ		1MΩ	
ULE	5	yes	no	20GΩ	0.2GΩ	85MΩ	$1.6 \cdot 10^{10}$
	6	no	yes	> 200MΩ		—[b]	
Al_2O_3	7	delamination (see Fig. 5.18)					
	8						
Corning 7980	9	no	no	5.98GΩ	4.37GΩ	110MΩ	$7.3 \cdot 10^{11}$
	10	yes	no	13GΩ	4.1GΩ	—[b]	$8.6 \cdot 10^{11}$
YAG	11	delamination (see Fig. 5.18)					
	12						
AlN	13	no	yes	>200MΩ		—[b]	
	14	yes	no	>200MΩ		25MΩ	
$MgAl_2O_4$	15	delamination (see Fig. 5.18)					
	16						
Si	17	used for UCN transmission tests					
	18						

[a] Impossible to measure because of the residual surface conductivity (see text).
[b] Not measured.

Table 5.5: Electric properties of diamond coatings (Process I). For the substrate suppliers, see page 41.

Table 5.5 summarizes the results of the electric tests. The columns with measured resistances correspond to the results obtained using configurations 2 and 3, respectively, see Fig. 5.11. If only the multimeter was used to determine the resistance, only the lower limit is given (>200 MΩ). Where two values are given, they correspond to two extreme voltage values used for the measurement with the more sophisticated ohmmeter (Keithley M6487, see Sec. 5.2.1.1). The result is usually calculated from Ohm's law, employing the voltage provided by the power supply and the measured current. It turned out that, again, the resistivity of the diamond coatings or, in fact, diamond coatings with conductive interface layers located underneath, was strongly dependent on applied voltage. In the Tab. 5.5 the first (higher) surface resistance value is usually obtained using 10 V and the second (lower) one with 500 V. On all samples examined (with the exception of Si_3N_4 which could not be checked because of the surface conductivity) an interface layer was found, which was much more conductive than the diamond coating itself. In other words, the problem that had already been discovered after the test process (see Sec. 5.3.4.1), was not solved; changing the process parameters and trying new substrates did not help. Actually, it seems that not only the conductive interface layer has been created, but also the resistivity of the diamond film itself has decreased, which is shown (in the last column Tab. 5.5, employing Eq. 5.11 and the same model as for the test process). Comparing the last

column of the table with the resistivity obtained after the test process, it is clear that the new coatings are almost two orders of magnitude worse. It is not clear, though, whether this fact has been caused only by too small amount of nitrogen added during the process or maybe also by their more than a factor of 2 smaller thickness. It is possible that thinner CVD coatings simply behave in a different way, because of effects associated with crystallite boundaries and grain sizes. The nucleation process starts from single diamond seeds randomly distributed over the surface and only after some time a uniform film is formed from diamond "islands", see also Fig. 5.23. Therefore, it is likely that the resistance of diamond coating does not scale linearly with its thickness, at least at the beginning. Also, the smaller size of the crystallites and their irregular shape (compare Figs. 5.13 with 5.20) can introduce some additional effect on the resistivity, due to possible surface conductivity on some diamond grains.

5.3.4.3 Process II

The only change for process II was the pressure of nitrogen, again the same as for the test process. Only those substrates were used, which were successfully coated during process I without delamination. It should improve the resistivity of the diamond film, and eliminate the interface layer due to different thermodynamic conditions. The risk was, of course, that the growth rate would decrease or that the nucleation would not start at all. Fortunately, it was not the case, and in a reasonable time 2 – 4.7 μm of diamond were deposited. Once again, the surface resistivity of diamond was observed and removed with corona discharge treatment at Fraunhofer IST. Discharge in oxygen and synthetic dried air atmospheres had been tried on separate samples, but no difference between both types of treatment was recognized later.

After the standard procedure of characterizing electrical properties, the results presented in Tab. 5.6 were achieved. First of all, the already known dependence of the resistance on the applied voltage was observed for each type of substrate (column $R_{surface}$). Then the interface layer was directly contacted and, as before, much higher conductivity was measured (column $R_{interface}$). Estimating the coating resistivity with Eq. 5.11 gave higher values than for the Process I. This time it ranged from roughly 10^{12} to 10^{14} $\Omega \cdot cm$, so closer to the outcome of the test process. Since the coating thickness is similar to the one obtained in process I, one can conclude that the resistivity change observed before was related to the different nitrogen content in the gas mixture.

Unfortunately, the most critical problem of the interface conductivity has not been solved at all. In order to unambiguously identify the conductive phase that gives the troubles and possibly avoid it in future, we used: Raman spectroscopy, X-ray diffraction and transmission electron microscopy. The results are to be discussed in the following section.

5.3.5 Interface layer identification

The principle of the XRD method was already described in Sec. 5.3.3.3. We decided to use it for our Si_3N_4 samples as a technique potentially sensitive for large contri-

Substrate	#	$R_{surface}$		$R_{interface}$	$\rho\,[\Omega\cdot\mathrm{cm}]$
		10 V	500 V		
Corning	1	15GΩ	0.1GΩ	45MΩ	$1.42\cdot10^{12}$
7980	2	>200MΩ		–	
ULE	3	4.5GΩ	50MΩ	0.16MΩ	$4.54\cdot10^{11}$
	4	>200MΩ		–	
AlN	5	12TΩ	240MΩ	80MΩ	$8.43\cdot10^{14}$
Y_2SiO_5	6	250GΩ	60MΩ	3.0MΩ	$9.13\cdot10^{12}$
Si_3N_4	7	2TΩ	0.6GΩ	0.5MΩ	$2.11\cdot10^{14}$
	8	>200MΩ		–	

Table 5.6: Electric properties of deposited diamond coatings (Process II).

butions of semi-conductive silicon carbide crystalline phase. The first measurement was performed in a standard configuration with large angle of incidence. The data was analyzed using Search&Match software[12], which identifies components of a multi-phase diffraction pattern matching it to a standard database [13]. The dominant part of the spectrum consisted of two different phases of Si_3N_4, SiO_2 and silicon aluminum oxide nitride, which were matched successfully. Also two peaks of synthetic diamond were found in the diffractogram, but no traces of silicon carbide.
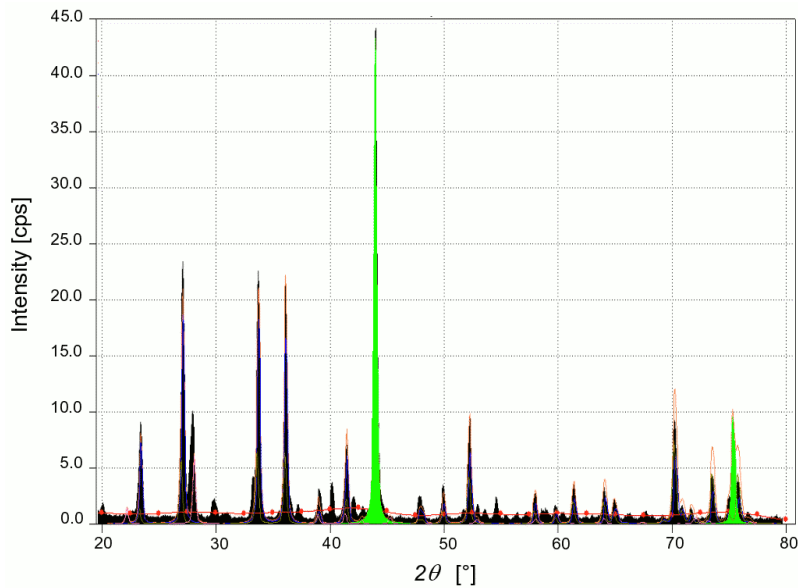

Figure 5.22: X-ray intensity (in counts per second) vs. scattering angle 2θ. Measured for a diamond coated Si_3N_4 sample (Test Process) in grazing incident angle configuration (GID). The figure depicts raw data (black), fitted background (• connected with a line), diamond peaks fitted to the data (green) and fitted profiles for other identified crystalline phases (see text).

---

[12]http://www.crystallographica.com
[13]Powder Diffraction File, http://www.icdd.com

We decided to use the GID configuration in order to be more sensitive for the coating and its direct vicinity. The result is shown in Fig. 5.22, this time diamond peaks are the dominant feature in the spectrum. Because the same phases as before are still visible in the diffractogram with somewhat lower intensity, one can conclude that indeed the measurement should be also sensitive for the interface between the diamond coating and the substrate. Although, also this time no trace of any SiC crystalline phase has been identified, the existence of a very thin and/or amorphous layer of SiC cannot be excluded completely.

The transmission electron microscopy characterization of a diamond coated Si_3N_4 sample was possible thanks to E. Müller (ETH Zürich). For TEM measurements a very thin slice of the sample (with some substrate, the coating and the interesting region in between) is first prepared, so that electron transmission through the remaining thickness is feasible, thus identification of elements in the sample (as electron transmission/scattering strongly depend on Z). Figure 5.23 shows our region of
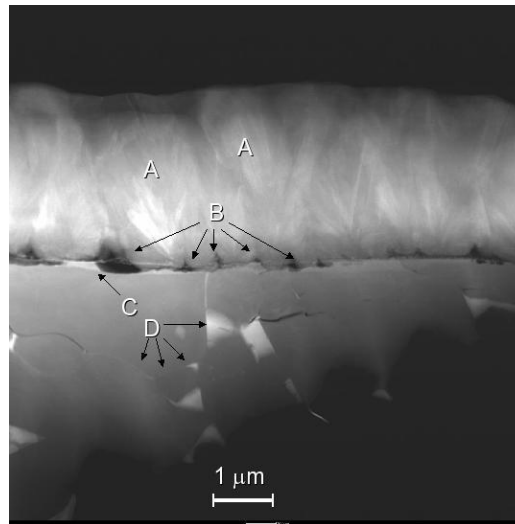
Figure 5.23: TEM picture (Z-contrast imaging) of the Si_3N_4 sample #7 (Process II). The diamond layer consists of large polycrystalline grains (A), which get broader towards the top of the layer. At the interface to the Si_3N_4 there are some holes (B), because the diamond grains do not fill all the space. In the Si_3N_4 a granular structure is visible. Along the grain boundaries as well as in the holes at the grain etches, heavier atomic species have accumulated (C) [114].

interest: clearly visible diamond at the top and the Si_3N_4 substrate at the bottom. Interesting features are the holes between the diamond grains at the interface and the accumulation of heavier (larger Z) material in the same region.

Energy dispersive X-ray spectroscopy (EDX), which is one of the TEM device features, aims at identifying the atomic composition of a material and is particularly sensitive to heavier elements. Preliminary low resolution EDX results, indicate that heavier material grains inside the substrate contain predominantly Ti, Y and Al. It is known that Si_3N_4 contains some yttrium and aluminum oxide additives (see p. 41), but the presence of Ti was suprising. It is likely that heavier materials might have

filled some of the holes in the bottom part of the coating.

Another TEM-related method, electron energy loss spectroscopy (EELS), has historically been a more difficult technique but is in principle capable of measuring atomic composition, chemical bonding, valence and conduction band electronic properties, surface properties, and element-specific pair distance distribution functions. EELS tends to work best at relatively low atomic numbers, where the excitation edges tend to be sharp, well-defined, and at experimentally accessible energy losses and is especially well suited to identify and distinguish various forms of carbon. So it is a perfect way to search for another suspect, which is graphite or amorphous carbon. Indeed, a tiny trace (on the sensitivity limit) of amorphous carbon was observed near the interface layer, only in some spots, though. Therefore it is hard to conclude unambigously, whether the amorphous carbon is (exclusively) responsible for the observed conductivity. Some trace was also found on the top of the coating, this is, however, believed to be a preparational artifact.

5.3.6 Fermi potential of diamond

A $1\,cm^2$ sample of stand-alone MWCVD diamond[14] was used in a cold neutron reflectometry (CNR) measurement to determine the Fermi potential of synthetic CVD diamond. The measurement was performed at the AMOR instrument at PSI. More details on the experimental setup and applied data analysis are published in a recent paper [115]. Similar technique is also described in detail in Sec. 5.4.1, where it is used to measure V_F of deuterated polymer coatings.

The measured Fermi potential of MWCVD diamond is $286 \pm 32\,neV$. The value is in good agreement with a theoretical prediction for natural diamond ($304\,neV$). The measurement accuracy is not excellent, so a significant influence ($\sim 10\,neV$), e.g. due to lower than natural density of the coating, cannot be excluded. However, even in that case the material would be still superior to other possibilities available for our application (see Tab. 5.1).

5.3.7 Summary and conclusions

Diamond coatings produced in all three HFCVD processes did not satisfy the requirements of the nEDM experiment. Some substrates (Al_2O_3, YAG, spinel) have been rejected, since it became clear that the diamond film deposited on them easily cracks and delaminates. In the other cases, although, the diamond itself seemed to be resistive enough (with resistivities $>10^{12}\ \Omega\cdot cm$), it was not possible to avoid a conductive interface layer between the diamond itself and the substrates.

There is some indication, comparing the results of the processes I and II, that the lower nitrogen partial pressure utilized for the process I leads to a lower resistivity of the diamond film itself (10^{10} – $10^{12}\ \Omega\cdot cm$). Unfortunately, the exact reason of the conductivity has not been unambiguously determined. Presumably the interface layer consists of silicon carbide or some graphitic phase or amorphous carbon. According

---

[14]from Fraunhofer IWM, Freiburg, Germany.

to the thermodynamic analysis, the hypothesis about some carbonic phase seems to be more likely, because:

- varying the CVD process parameters had no clear effect and did not eliminate the interface layer

- there was almost no difference between different substrates, in contrary to what was expected from the calculations.

On the other hand, it is not clear how such an amorphous carbon layer could be deposited in the presence of atomic hydrogen. The results of XRD measurements and transmission electron microscopy, which could have provided some additional information, were unfortunately inconclusive and did not provide strong evidence for either hypothesis. Pursuing that mystery further would require considerable effort and at least several more time and cost consuming CVD processes, with no guarantee of success (since there was no convincing idea for the future improvements). In addition, the problem to develop a HFCVD reactor suitable for the actual insulator ring would still require a technical solution.

Therefore, the proposal to use HFCVD diamond as the insulator ring coating was abandoned and we moved on to the next option (see below).

5.4 Deuterated polymer coatings

5.4.1 Fermi potential of DPE and DPS
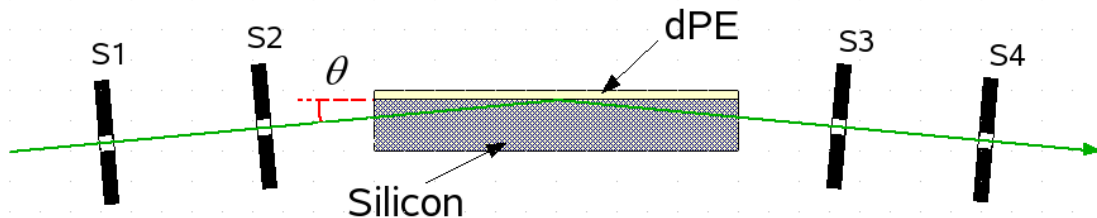
Figure 5.24: Scheme of the cold neutron reflectometry setup. The silicon slab has dimensions $10 \times 5 \times 1 \, \text{cm}^3$ and attenuates the neutron beam by $\sim 20\%$. Measurements were performed over the angle range from $0 \leq \theta \leq 0.8°$.

The Fermi potentials of thin DPS (deuterated polystyrene) and DPE (deuterated polyethylene) coatings on silicon substrates were measured by means of cold neutron reflectometry (CNR, as introduced first by [116, 117]). We have used this method recently to determine the Fermi potential of various materials [115, 118, 119] and found good agreement with the results obtained with other methods. This method measures
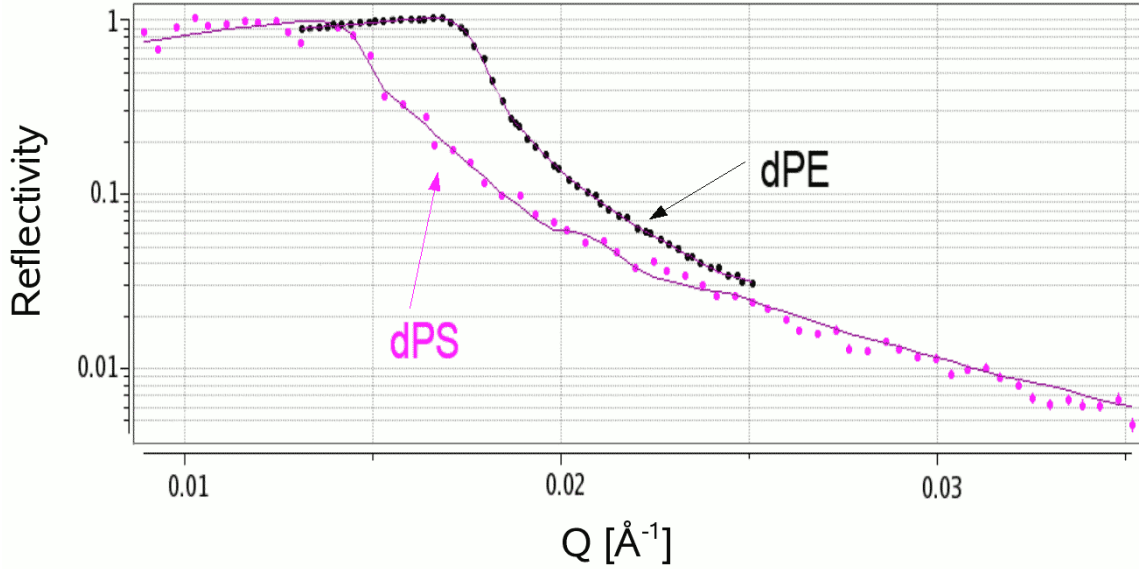
Figure 5.25: Cold neutron reflectivity vs. momentum transfer for DPS and DPE. The measured points are compared to the results of the fits (described in the text) which, after taking into account systematic uncertainties, yield $V_F(\mathrm{DPS}) = (161 \pm 10)$ neV and $V_F(\mathrm{DPE}) = (214 \pm 10)$ neV.

the critical angle for total reflection of cold neutrons for grazing incidence where the velocity component normal to the surface becomes comparable to the velocity of UCN. The grazing angle condition (e.g. the critical angle for DPS is $\sim 0.33°$) calls for smooth, mirror-like surfaces in order to retain good angle definition. Since straightforward coating techniques usually do not produce such surface qualities, the arrangement used here differs from that described in Refs. [115, 118] in that the collimated neutron beam was reflected from the coating-substrate interface, and not from the coating-air interface. In this way one can exploit the close-to-perfect surface of silicon substrates. The principle of the setup is given in Fig. 5.24. The experiments were performed at the Narziss instrument of SINQ [120], using cold neutrons with wavelength $\lambda = 4.97$ Å. Figure 5.25 shows the reflectivity curves for DPS and DPE, where the angle θ has been replaced by the momentum transfer according to $Q = \frac{2\pi}{\lambda} \sin 2\theta$. Fitting these curves allows determining the scattering length densities (i.e. the term $N \cdot b$ in Eq. 2.1) from which the Fermi potentials can be extracted. We used two openly available analyzing routines, Parrat32 [121] and Reflfit [122] which gave consistent results within the uncertainties given in Tab. 5.7. In the analysis we used a 3-layer model consisting of Si ($V_F = 54$ neV, i.e. $\varrho = 2.329$ g/cm^3), the coating in question and an air layer at the backside. The uncertainties for V_F are completely dominated by the absolute angle accuracy (about $0.01°$) with which the sample surface can be reproducibly adjusted with respect to the collimated neutron beam. The resulting systematic error is several times larger than the other errors combined (statistical errors of the fitting procedure, potential reduction of the density of Si at the interface due to contamination and dust).

Calculated values of the Fermi potentials (Tab. 5.7, column 3) depend on the material composition and its density. For deuterated material layers prepared by evaporation of solutions the density may not be exactly the same as that for the solid precursor material, moreover, for thin films the density is known to be lower than for bulk material. Therefore, we measured the densities of thin film witness samples using a pycnometer, see column 2 of Table 5.7. The results agree with expectation, when typical density values for high-density PS ($\varrho = 1.06$ g/cm^3) and PE ($\varrho = 0.94$ g/cm^3) are scaled up by replacing hydrogen with deuterium. The Fermi potential values calculated from these densities using Eq. 2.1, modified to include the contributing atomic species i.

$$V_F = \frac{2\pi\hbar^2}{m_n} \sum_i d_i \frac{N_A}{M_i} b_i, \tag{5.12}$$

where N_A is the Avogadro constant and M is the molar mass. The calculated values are consistent with those extracted from cold neutron reflectometry measurement, as given in column 3 of Tab. 5.7.

Material	ϱ [g/cm^3]	V_F (calc.) [neV]	V_F (meas.)[neV]
DPS foil	1.146 (22)	170 (3)	161 (10)
DPE foil	1.071 (19)	209 (4)	214 (10)

Table 5.7: Material parameters for DPS and DPE: material density ϱ, Fermi potential V_F calculated from measured density with Eq. 5.12 and Fermi potential measured directly by means of cold neutron reflectometry.

5.4.2 DPS coated chamber

After the attempt of making a diamond coated insulating storage chamber had failed and after Si_3N_4 had turned out to be incompatible with Hg co-magnetometry, we finally focused on thermoplastic polymers. Their good insulating properties and HV resistance are well known (see Tab. 5.1), in addition to this, some polymers have been already successfully used together with the Hg co-magnetometer (see the previous section). Deuterated PS and PE have Fermi potentials above 160 neV(see Sec. 5.4.1) and are expected to have low losses. That is how the idea of manufacturing a thermoplastic polymer ring, coated from inside with a thin layer of deuterated polymer of the same species, emerged. Of course, deuterated compounds are only available in small quantities, so a full size DPS ring cannot be afforded. On the other hand, the same chemical character of the substrate ring and the coating should guarantee best-possible bonding between them and helps to avoid problems with delamination or HV stability, which is, in general, very sensitive to insulator inhomogeneities.

Although DPE has higher V_F than DPS, we decided to use a DPS coated PS ring for several other reasons. Firstly, PS is more rigid and mechanically stable, which makes it a better candidate for machining within stringent tolerances, given by the existing electrodes. Secondly, the DPS coating can be deposited at room temperature, in contrast to DPE, which requires elevated temperatures, leading to

additional technical complications in the process. Furthermore, as it is known from the simulations (see Tab. 4.3), increasing V_F from the DPS to the DPE value, would not give any substantial gain in statistics. Thus, for Phase II of the project it simply does not pay to use DPE. However, for Phase III it might be worth the additional effort.[15].

Instead of commercially available 'normal' PS[16], we decided to use a special HV grade, Rexolite. Rexolite 1422 is a cross linked (with divinylbenzene) polystyrene plastic, produced by C-LEC Plastics Inc. (U.S.). Its mechanical and optical properties are approximately equal to those of normal polystyrene or acrylic. Concerning the chemical stability, alkalies, alcohols, aliphatic hydrocarbons and mineral acids have no effect on the material. Aromatic & chlorinated hydrocarbons (benzene, toluene, xylene, styrene, chloroform, CCl_4) and acetone cause swelling and can solve it. Rexolite has outstanding electrical properties and is widely used as an insulator. The temperature range recommended by the supplier is between -60 and $100°C$. The outgassing of a Rexolite piece was measured to be about $3 \cdot 10^{-7}$ mbar $\cdot$ l/s/cm^2 after 5 days of pumping at room temperature (RT).

5.4.2.1   Small scale tests

The feasibility of coating PS rings with DPS was first tested on a small scale in a dedicated setup. Test PS and Rexolite rings scaled by about 1:5 (inner diameter 94 mm, outer diameter 100 mm, $1-3$ cm height) were produced together with fitting aluminum electrodes of 15 cm diameter. The electrodes had rounded edges and grooves, just as the real ones at ILL, and an additional hole in the center (for vacuum reasons), see Fig. 5.26. After machining, each element of the setup was thoroughly ultrasonically cleaned in isopropanol, demineralized water and finally dried in nitrogen (from a dewar). The electrodes were additionally rinsed with acetone at the beginning.

A ~ 200 l large vacuum tank equipped with an oil-filled HV feedthrough and a quartz window was also cleaned with IPA. Vacuum of the order of $5 \cdot 10^{-4}$ or better was typically reached within a couple of hours. The chamber was usually vented with dry nitrogen from a tank, to limit the exposure of the copper parts to humid air.

At various stages one of the three following HV power supplies was used: bipolar 60 kV Heinzinger, positive 60 kV F.u.G. and bipolar 130 kV Spellman. The HV connector inside the chamber was connected with the "top" electrode using 5 mm thick copper wire. In order to avoid sparking, both ends of the wire were bent such that sharp edges were not exposed. Similar to the setup presented in Sec. 5.2.1.1, the bottom "ground" electrode was connected via a 1.4 GΩ HV resistor [17] to a picoammeter, for current monitoring. Optionally, the analog output of the picoammeter and

---

[15]High or Ultra-High Molecular Weight PE (like Polystone PE) could be an interesting candidate for the ring substrate material, due to somewhat better mechanical (1.2 GPa Young modulus) and electrical properties.

[16]PS is typically available with plate thickness < 3 cm; specially ordered plates with 6 cm thickness contained a large amount of air bubbles and could not be used.

[17]Two cylindrical resistors of type 1000.200 from NICROM Electronic, connected in series.
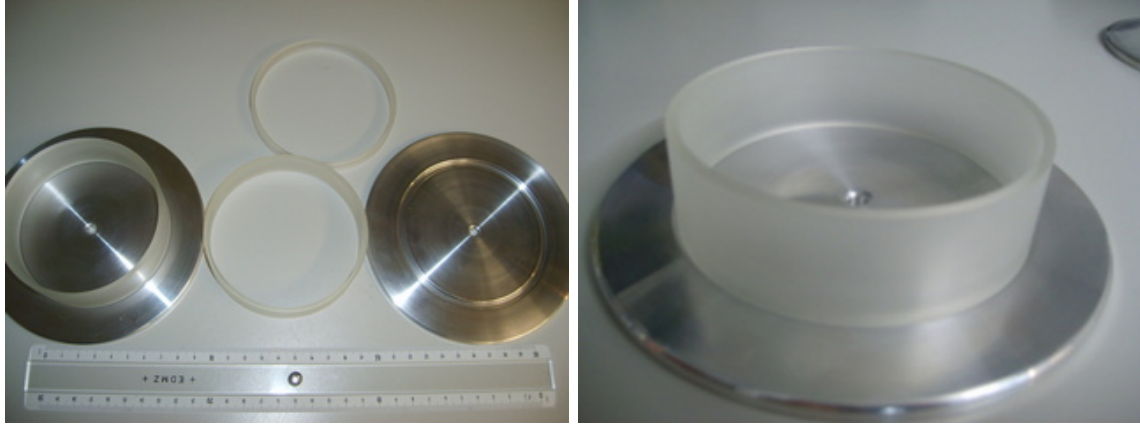
Figure 5.26: Small aluminum electrodes and polystyrene sample rings for HV tests.

a digital scope could be used for real time data visualization. A DAQ module[18] was adapted to control the power supply and monitor the current with a PC, with communication via USB. In order to electrically decouple the HV power supply from the DAQ electronics, a dedicated module was designed and constructed, which replaced direct connections with isolation amplifiers, optocouplings and relays [124].

After several hours of HV training and a few flashover discharges, uncoated PS and Rexolite rings could stand the highest voltage available (130 kV at both polarities) with low currents (< 200 pA) and rare sparking (several per day, visible by eye). Since the grooves in the electrodes were 2 mm deep, the electrode distance for the 1 cm high ring equals 6 mm and thus, the maximum field gradient was 217 kV/cm.

Given the encouraging results, the rings were coated with PS or DPS, baked at $\sim 60°$C in vacuum for about ten hours and tested again. The HV performance was usually worse after the coating; stable operation was possible at 70 kV over the gap (which corresponds to 117 kV/cm). The vacuum baking time and the 'quality' of the coating turned out to be critical. Any dust particles trapped in the PS would potentially initiate discharges and permanent damage of the insulator at high-voltages.

The resistance of a DPS-coated Rexolite ring was estimated. From the fit shown in Fig. 5.27, the value of $R = (1.26 \pm 0.05) \times 10^{16} \, \Omega$ can be extracted, which, for a 1 cm high ring, translates to a resistivity $\rho = (4.62 \pm 0.16) \times 10^{17} \, \Omega \cdot \text{cm}$. The sudden drop in measured resistance above 20 kV(~ 33 kV/cm) might be speculatively attributed to different contribution of surface and bulk conductivities to the total conductivity at different voltages.

The promising results achieved from the small scale tests encouraged us to proceed with production of a full size Rexolite insulator for the nEDM experiment.

5.4.2.2 The insulator

The insulator ring was machined from a Rexolite block of about $600 \times 600 \times 155$ mm^3 [125]. The geometry and dimensions of the old Sussex/RAL/ILL quartz ring were used with one minor change; in order to achieve better mechanical stability of the

---

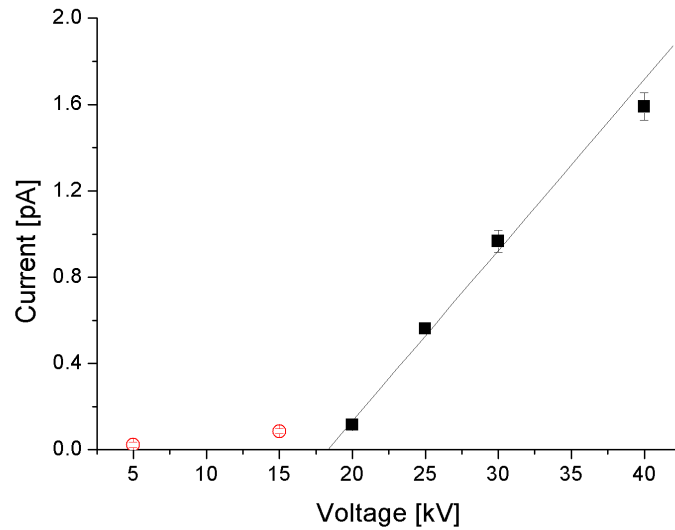[18]Based on SCS2000 and Midas system [123], developed by the PSI electronics group.

Figure 5.27: Leakage current measured at several voltages for a small DPS-coated Rexolite ring. The first two points were not included in the fit, which yields an estimate $\rho = (4.62 \pm 0.16) \times 10^{17}\,\Omega \cdot \mathrm{cm}$.

inserted DPE coated quartz windows and prevent them from falling into the chamber, additional limiting apertures were added to the holes.

Rexolite is brittle, but also somewhat plastic: the finished piece could be compressed easily by several tenths of a millimeter without relaxation. This lead to problems with the support during turning and with the overall 'roundness'. The requirement on the surface roughness of the end faces was $R_a < 0.8\,\mu$m, in order to minimize gaps between the insulator and the electrode surfaces. As already mentioned (see p. 48) good contact with the electrode improves the overall HV stability and increases the flashover voltage.

As it was later inspected with a coordinate-measuring machine, the flatness achieved was slightly above 20 microns: 25 μm of maximal variation over ten points measured at the top end face and 23 μm over 8 points at the bottom end face. The non-parallelity of the end faces, important with respect to the field homogeneity requirements, was 15 μm over 50 cm diameter. On average the height was 150.07 mm, the inner diameter 470.41 mm and the outer diameter 498.32 mm. More details on exact dimensions of the insulator are available in the internal report [126].

5.4.2.3   Coating process

Previous application of DPS reported a manual coating technique using some kind of spatula with a quickly drying solution of DPS in d-toluene [127,55] or dipping in such a solution [128]. The first method was considered critical because the coating uniformity cannot be controlled sufficiently and there would be a high risk of introducing bubbles or voids. The latter method requires a large amount of expensive solution.

Therefore a new "rotating lake" principle was developed: the insulating cylinder was clamped tightly between two plates and supported such that the whole setup could be rotated with an electric toy motor around the cylinder axis, which was supported horizontally. The exact amount of DPS solution necessary to produce the desired layer thickness was inserted via a hole in one end plate, and the DPS lake which had formed at the bottom was then made to cover the entire inner surface of the cylinder by rotating the setup. After evaporation of the solvent one is left with a uniform coating.

Of course, the window holes in the cylinder need to be closed by some properly shaped plugs to facilitate uniform flow of the solution around the hole regions. Also, in order to avoid the contamination of the inside of the window holes and both end faces, a tight seal had to be used around the plugs and between the insulator and the clamped plates. Initially, gaskets made out of soft PVC were used. Unfortunately, PVC contains large amounts of plasticizer, which is soluble in toluene and makes the coating soft and sticky. The lesson was learned in October 2007 and since then 0.05 mm thin PTFE foil has been used to separate the PVC gaskets from the solution.

In practice we proceeded as follows: the Rexolite ring was thoroughly cleaned after machining in an ultrasonic bath with isopropanol and outgassed in vacuum at room temperature. It was then mounted in the rotation setup (see Fig. 5.28) in a cleanroom while trying to eliminate dust by blowing air in combination with a piezo-electric antistatic pistol[19], as suggested by Golub [70]. The DPS base material [20] was cut manually into small pieces and dissolved in either normal analysis-grade toluene or d-toluene[21]. We prepared two mixtures in order to minimize on the (expensive) d-toluene consumption, one with DPS in toluene (0.5 g DPS in 0.15 l toluene) and one with DPS in d-toluene (1 g DPS in 0.075 l d-toluene); at room temperature it took about 3 days for the DPS to dissolve completely. Since no specific tests had been performed concerning the UCN loss with either normal toluene or d-toluene, we thought it safe to use d-toluene for the top layer. In addition, the application of two independent layers reduces the probability of holes. To eliminate dirt particles the mixtures were passed through 4 micron pore PTFE filters.

In the first coating step we applied the DPS/toluene mixture and initially rotated the ring at about 3 rpm. The 4 windows were airtight sealed by mylar for the first few rotations and then replaced successively by cleanroom tissues to get some air exchange, but at the same time prevent dust particles (and flies[22]) from getting trapped in the coating. The DPS "lake" at the bottom evaporated after about 120 min. The rotation speed was increased to about 20 rpm for the next 16 h. The resulting surface appeared dry and hard. The setup remained in the cleanroom without rotation for another 8 h and was then disassembled, so the insulator could be outgassed in vacuum (64 h). With a known amount of DPS in the solution and the measured mass of

---

[19]Zerostat 3 obtained from Milty, normally suited to clean phonograph records.

[20]98 at-% deuterated, obtained from Armar Chemicals.

[21]98 at-% deuterated, obtained from Armar Chemicals.

[22]The cleanroom, which is a dust-free environment by definition, does not necessarily have to be completely fly-free. Not always, at least. That allowed one of our cleanroom flies to successfuly test the fresh DPS coating as an efficient fly sticker.

Figure 5.28: The coating device being adjusted for good 'horizontality' (left). The Rexolite ring is being rotated with some DPS solution inside until the solvent evaporates (right).

residual DPS, which remained on the gaskets and clamped plates, the average coating thickness was estimated to be 1.8 μm.

In the second step we applied in a similar way the DPS/d-toluene mixture, resulting in an additional 3.9 micron of DPS (5.7 μm thick in total). The surface appeared dry after one hour, but was kept in air for another 16 h before transfer into vacuum for outgassing (140 h). Except for a few larger particles/defects there was no indication of bubbles or defects in/on the coating visible by eye. The surface had a dull glaze; this was specific for the Rexolite substrate, the same coating on PS (Tekaren®) produced more shiny surfaces.

5.4.2.4   Outgassing

During the coating process the base material gets soaked with toluene and water, which leads to heavy outgassing in vacuum. It can cause serious problems when directly used in the experimental apparatus, as the high-voltage performance and the ^{199}Hg vapor polarization lifetime are very sensitive to "bad" vacuum and get bad very quickly as soon as the chamber entrance is closed for the storage. This behavior was actually observed with the insufficiently outgassed insulator in December 2007 (see Fig. 5.29, blue diamonds). The pressure reached at the end of outgassing at room temperature, $1.2 \cdot 10^{-5}$, can be translated into an outgassing rate of $2 \cdot 10^{-7}$ mbar l/s/cm^2. Based on this we expect a pressure increase in the storage trap of about $2.3 \cdot 10^{-3}$ mbar after 100 s, which is a typical storage time.

From the previous unsuccessful coating attempt (curve 'a' in Fig. 5.29) we knew the outgassing rate, which was sufficiently good to operate the nEDM apparatus. In order to reduce the outgassing, a dedicated heat-conditioning vacuum chamber was used, as the temperature turned out to be a critical factor for the conditioning speed. After cleaning with IPA the chamber was pre-conditioned for 2 days at 120°C. Then the temperature was ramped down to 60°C, considered as a safe value for polystyrene, and the insulator was inserted into the chamber for next couple of weeks. Eventu-
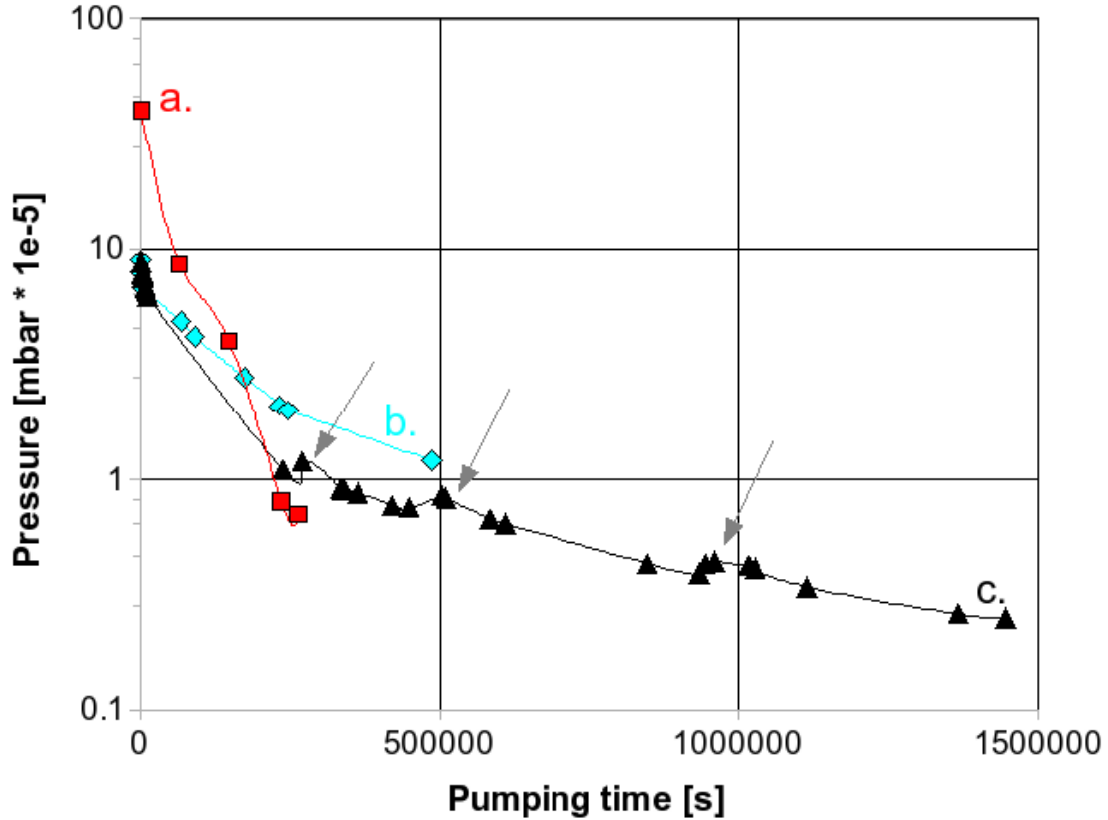
Figure 5.29: Vacuum conditioning curves: (a) first unsuccessful coating (contaminated with the plasticizer from PVC) in October 2007 at 60°C (red □), (b) the good coating outgassed in vacuum at 20°C in December 2007 (blue diamonds) and (c) vacuum-baking at 60°C in February 2008 (black △). The three "bumps" (marked by arrows) in the last curve occurred each time when the temperature was elevated (by about 2°C).

ally $2.5 \cdot 10^{-6}$ mbar was reached, which corresponds to $5 \cdot 10^{-8}$ mbar l/s/cm^2. This resulted in pressure conditions in the nEDM experiment similar to those observed with the quartz insulator used before.

5.4.3   DPE coating for the optical windows

As already mentioned (see Sec. 3.2), mercury vapor co-magnetometry is an important feature of the nEDM spectrometer and allows to correct for the effects of varying ambient magnetic fields on the stored neutrons. Polarized ^{199}Hg vapor is injected into the storage volume and spin flipped by $\pi/2$, just after the same happens with neutrons. It samples the same volume as the neutrons and, due to the constant $\mathbf{B}_0$ field, it also experiences precession with the corresponding Larmor frequency. All changes of the Hg precession frequency indicate some change of the field inside the storage volume; this information can then be used to correct the neutron data anal-

ysis. The measurement of the Hg frequency is performed with a circularly polarized light beam at 253.7 nm, passing through the storage volume via two optical windows mounted in the chamber wall. The Hg precession frequency (and thus the field, $\omega_L = \gamma B$) can be directly extracted from the modulation of the beam amplitude, which is constantly monitored with a photomultiplier (for the details of the setup, see [55, Sec. 5.2.5], [60, Chapt. VII]). On top of the requirements listed in 5.1, some additional properties are needed for the windows: a) long term resistance against UV light, b) high transmission and low depolarization at 253.7 nm, c) 'optical' quality surface to avoid distortion and scattering of the light beam.

The material that has been successfully used so far was quartz, either UV grade fused silica or HSQ-300, which is the same grade as the old quartz storage ring. The disadvantage of any type of quartz (also glass) is its low Fermi potential of 94 neV. Given the size of the windows ($\sim$20 cm^2 each, around 0.3% of the total trap surface) it is clear, that during the precession time all the UCN with energies > 94 neV, initially trapped because of the improved chamber wall material (and bouncing the walls $\sim$20 times per second), would eventually escape through the windows. In other words, improving the Fermi potential of the chamber wall makes sense only if the Fermi potential of the windows is also improved.

As for the storage ring itself, two other candidates were considered: diamond and deuterated polystyrene. The technology of producing microwave CVD (MWCVD) diamond windows of that diameter, although expensive, is well under control[23] and used for synchrotron applications. MWCVD provides stand-alone diamond windows, allowing to avoid problems with conductive interface layers, described in the previous section. Unfortunately, the light transmission at 254 nm is around 50% for one window only, mostly due to the diamond refraction index (2.4, resulting in 30% reflection), but also due to the scattering at grain boundaries of polycrystalline material and due to thickness dependent absorption. Given the dielectric constant of diamond (5.7, much different from that for quartz or for PS, see Tab. 5.1) and the available thickness of diamond windows (about 0.5 mm), it might be also quite problematic to mount them in the storage ring without inducing major electric field inhomogeneities. The second candidate, DPS, is not resistant against intense UV light and even after long-term exposure to direct sunlight becomes brownish, brittle and cracks. Although it has been already tested in the old apparatus with some success [127,60], long-term stable operation of the system requires a more reliable alternative.

Deuterated polyethylene (DPE) turned out to be the solution. Its thermal and electrical resistivity and high voltage properties are similar to those of polystyrene, moreover it is resistant against UV light, which was proven with a simple test. After a week of exposure to radiation from a Hg spectral lamp[24], no changes were observed in a sample PE film, while under the same conditions a similar size PS sample was heavily damaged. DPE is soluble in acetone, toluene and similar aromatic solvents (like e.g. xylene and decaline) and DPE coatings can be easily produced on a normal quartz optical window e.g. by spin coating. Also the Fermi potential of DPE is higher than for DPS, which was confirmed experimentally. However, (D)PS is still

---

[23]http://www.diamond-materials.com
[24]Hg(Ar) Model No. 6035 from LOT-Oriel Instruments

superior to (D)PE in terms of mechanical properties. The higher Young modulus of PS ($\sim$3.5 GPa compared with 0.8 GPa for PE), makes it possible to machine the material within the stringent tolerances.

In the following sections the optimization and characterization of window coatings are described.

5.4.3.1 Spin coating

Spin coating is a standard procedure to apply uniform thin films on flat substrates, widely used e.g. in lithography. An excess amount of the relevant solution is placed on the substrate, which is then rotated with a spinner at high speed in order to spread the fluid by centrifugal force. As the fluid spins of the edges of the substrate, a thin film remains, flowing slowly outward from the center. The volatile solvent evaporates, increasing the viscosity of the film and reducing the radial flow. Eventually, the relative motion of the deposited film ceases and the spinner is stopped. If necessary, the residual solvent can be evaporated in an oven. In detail, the process is very complex and difficult to model, due to many possible mechanisms to consider (fluid inertia, surface tension, Coriolis force, solvent volatility, heat transfer, shear stress, turbulent effects; with all the parameters being functions of time). A comprehensive review of various theoretical approaches to the problem can be found in the literature [129].

In particular, spin coating for polymeric coatings, including also PE, was studied in detail resulting in an optimized method for production of perfectly clear and transparent PE films of desired thickness (0.03 – 2 μm). Mellbring et al. [130] investigated the thickness and quality of high-density polyethylene (HDPE) coatings as a function of deposition temperature, rotation speed and the PE concentration in the solution. Wirtz et al. [131] further extended the study to low-density polyethylene (LDPE) and fine-tuned the method for thin (100 – 200 nm) optically clear coatings on glass. Both authors used PE solved in decalin ($C_{10}H_{18}$, boiling point: $\sim$190°C), spincoated at temperatures within the range of 100 – 180°C. They pointed out that the coating thickness was proportional to the temperature and the concentration of the polymer solution. The spinning rate had only a minor influence on the film thickness, however the best results with respect to smoothness and absence of macroscopic defects were obtained at 2000 rpm. In general, thinner films (below 300 nm), deposited at lower temperatures, were more uniform and free of radial striations, with typical roughness of around $R_a = 12$ nm.

We employed the recommended procedure with some specific changes to produce deuterated coatings. Since the availability of deuterated decalin is limited, we decided to use either toluene-d8 or o-xylene-d10. At the very beginning also undeuterated compounds were used in order to reproduce some typical results from the literature with our spin coater[25]. For initial tests we used 1 mm thick Suprasil substrates, ultrasonically cleaned with acetone, 2-propanol and demineralized water. As advised, not only the solution, but also the substrates and a glass syringe, used to apply the coating, were always preheated in an oven to the same temperature as the solution.

---

[25]Type Delta 6 RC TT from Süss MicroTec Litography GmbH.

Necessary precautions associated with handling hot, volatile, boiling, flammable and toxic chemicals were taken, in addition to this, we had to keep the transfer time of hot substrate from the oven to the spinner below 10 seconds. About 2 ml of hot solution would be then applied to the substrate to entirely wet its surface, additional 2 – 3 ml would be added during the initial phase ($\sim$10 s) of spinning (which was 60 seconds in total).

It was quickly learned, that toluene evaporates too fast (boiling point 109°C), resulting in inhomogeneous, opaque coatings. With o-xylene (boiling point 144°C) and using 5% or 1.5% PE concentration we managed to elevate the deposition temperature to about 130°C and achieved clear transparent coatings, 100 – 200 nm thick. After mastering the technique we switched to deuterated compounds[26] and, due to the higher density of DPE, had to optimize the deposition parameters again. Since it was already impossible to rise the temperature further, the concentration of the polymer solution was decreased. Eventually, satisfactory results were obtained at 140°C and 2000 rpm.

Finally, DPE coatings were applied to 1 cm thick UV grade fused silica windows (50 and 57 mm diameter), to be used in the UCN storage chamber. Because of the larger substrate diameter, we had to use especially made aluminum rings to fix the windows to the chuck of the spin coater. Again, the settings had to be modified slightly to compensate for the slower cooling rate of thick UVFS windows. The final $\sim$75 nm thick coatings were deposited at 130°C and 1000 rpm, using 8 ml of 0.75% solution.

5.4.3.2 Transmission and depolarization measurements

Light transmission and depolarization at the wavelength corresponding to the Hg spectral line used by the co-magnetometer (253.7 nm), are crucial parameters of the windows. Due to the relatively small difference of refraction indices of quartz and PE (both around 1.5), Fresnel reflection losses of the coated window are similar as for the uncoated one (around 8%). On the other hand, polymers typically show high absorption for UV light. Absorption is proportional to the thickness of the coating and for thicknesses below one micron the expected value is of the order of a few percent. Using a UV-Vis-NIR spectrometer[27] we measured the transmission spectra of DPE-coated windows and of the old windows from the RAL/Sussex nEDM experiment, see Fig. 5.30. The best transmission was measured with Suprasil ($\sim$92%). One of the old nEDM windows and the new UVFS windows show about 1% worse performance. PE-coated Suprasil samples, depending on the coating quality, transmit 85 – 90% of light. Finally, the other old nEDM window and a new HSQ300 quartz window give 83% and 70%, respectively.

Concerning light polarization issues, contrary to amorphous LDPE, high-density polyethylene undergoes crystallization during spin coating, forming potentially optically anisotropic and birefingent oriented crystals [132]. Therefore there is a certain risk of either depolarizing the Hg light or introducing some spurious polarization

---

[26]from ARMAR Chemicals AG, Döttingen, Switzerland.
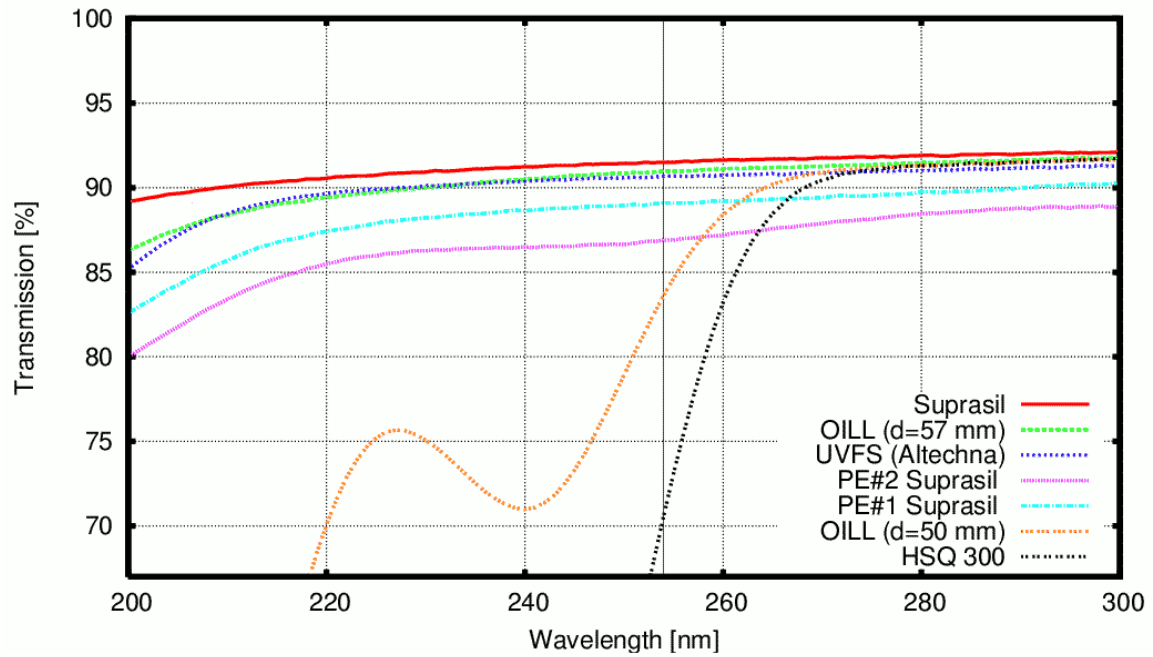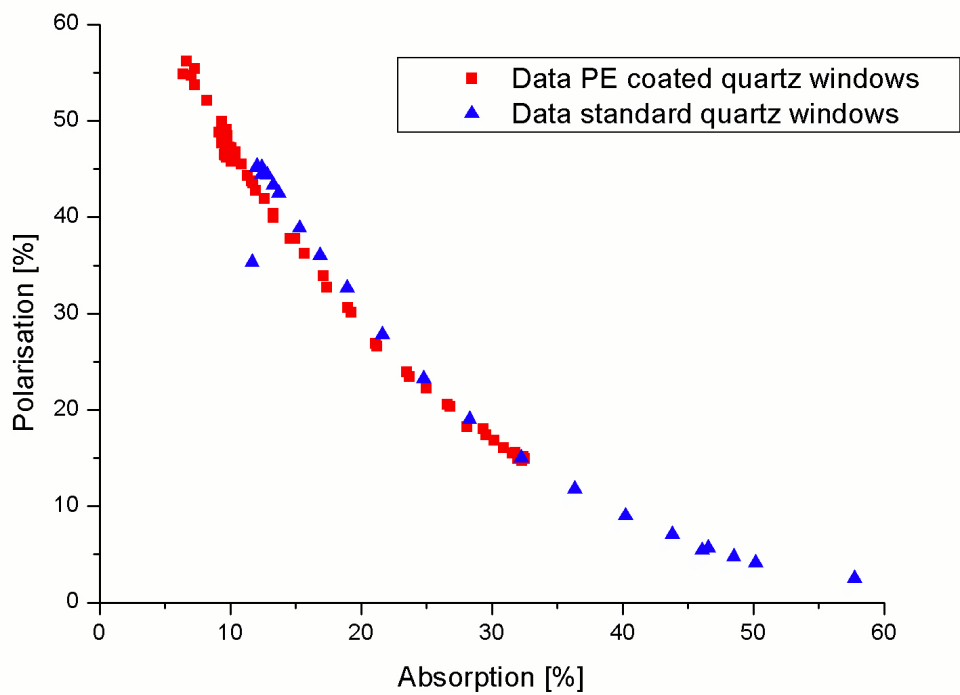[27]type Cary 500 Scan from Varian, Inc.

Figure 5.30: Transmission at 253.7 nm.

Figure 5.31: Hg performance vapor polarization vs. absorption for the standard quartz windows ($\triangle$) and the DPE coated quartz windows ($\square$).

changes. This motivated a series of measurements with the DPE coated windows in situ, using the nEDM spectrometer at ILL. Depolarization of the analyzing beam could result in lower measured absolute value of ^{199}Hg vapor polarization or lower amplitude of the analyzing light modulation, which can be translated directly into signal to noise ratio. We observed no difference in signal to noise ratio between old uncoated quartz windows and the new DPE-coated ones, in both cases that parameter fluctuated around 600. A good benchmark for the co-magnetometer performance sensitivity to a possible depolarization effect is given by a measurement of the dependency between the observed ^{199}Hg polarization and the absorption. In particular, it shows what level of polarization can be achieved in the optimal absorption range (10 – 20%). Again, results for uncoated and coated windows are very similar (see Fig. 5.31) and demonstrate that DPE with a Fermi potential of 214 neV can be used.

5.4.3.3   Surface profiles

The surface structure and thickness of the coatings were investigated using a profiler[28]. It is important for the DPE layer to be uniform and free of holes, which for the UCN with energies higher than V_F of the quartz substrate would act as UCN absorbers and which would increase the effective loss probability per bounce for the remaining UCN. Moreover, since it is necessary that the neutrons interact only with the coating, it has to be thick enough to keep the transmission into the substrate on a safe level. The UCN transmission through the DPE film due to quantum tunnelling corresponds to a standard quantum-mechanical problem of the (one-dimensional) finite potential barrier. Also, the earlier discussion concluded with Eq. 2.25 can be applied here, as in the $V_F \to 0$ limit the formula directly reduces to the finite potential barrier solution:

$$|T|^2 = \left[1 + \frac{V_F'^2 \sinh^2(\beta d)}{4E(V_F' - E)} \right]^{-1} . \tag{5.13}$$

We neglect the absorption and up-scattering effects, since we are only interested in finding a minimal coating thickness, which would sufficiently suppress the tunnelling effects. Since the problem was treated one-dimensionally, the solution is valid for UCN, which collide with a wall at normal incidence. Transmission curves for DPE are given in Fig. 5.32. Normally, a transmission limit of the order of 10^{-6} is considered safe, since typical loss probabilities for materials used in the experiment are of the order of 10^{-4}.

In order to check the coating thickness, profiles of the samples over an artificially produced scratch were measured. The raw quartz substrate is clearly visible at the bottom of the scratch, thus giving a reference for the thickness estimate (see Fig. 5.33). The coating is more or less homogeneously distributed over the substrate and thickness measurement both in the center and near the edges give similar results of around 75 nm. Several 300 μm long linear scans were performed in various locations on the sample and except for the artificially made scratch, no holes were found. Rough examination with an optical microscope indicated that the coating

---

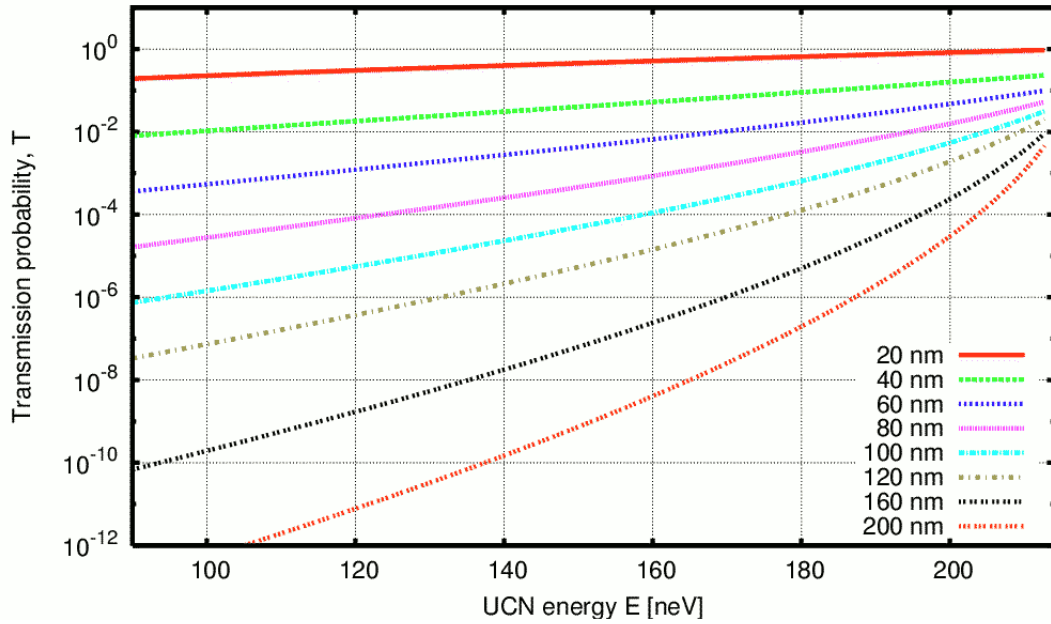[28]type Dektak 8M from Veeco Instruments, Inc.

Figure 5.32: Transmission probability calculated for various thicknesses of DPE foil as a function of UCN energy at normal incidence. Curves were calculated using $|T|^2$ from Eq. 5.13.

was free of major defects. In some spots, especially near the rotation center of the substrate, characteristic wavy structures are visible (of $\sim$10 nm amplitude), see e.g. Fig. 5.33(a).

From the Fig. 5.32 one can find relevant transmission (loss) probabilities. The UCN spectrum in the storage chamber is limited by the Fermi potential of the insulator wall, which can be either quartz (90 neV) or e.g. DPS (161 neV). Looking at the curve for $d = 80$ nm for both limiting energies one obtains roughly 10^{-5} for quartz and 10^{-3} for DPS. However, since the window area corresponds to only 0.3% of the total trap area, relatively higher loss probability at the DPE coating will not contribute significantly to the overall storage performance of the chamber. For the DPS coated insulator it would contribute additional $10^{-3} \cdot 0.3\% \approx 3 \cdot 10^{-6}$, which is in present configuration completely unmeasurable. In reality, the transmission is further suppressed by collisions at incidence angles from the full range.

Therefore, we can conclude that the DPE coated optical windows have all the necessary properties for the nEDM experiment. The compatibility with the Hg vapor co-magnetometer was proven experimentally and from the analysis of the coating surface it is also clear that it is free of holes and sufficiently thick to guarantee good storage parameters for UCN.

If only materials with Fermi potential e.g. around 200 neV were used for the insulator coating (which is still possible in the future), it would be necessary to increase its thickness, otherwise the losses would become more severe (see Fig. 5.32). In any case, coating thickness of about 200 nm should be sufficient to keep the losses on the safe level. Such an increase in the coating thickness might require deposition

(a)

(b)
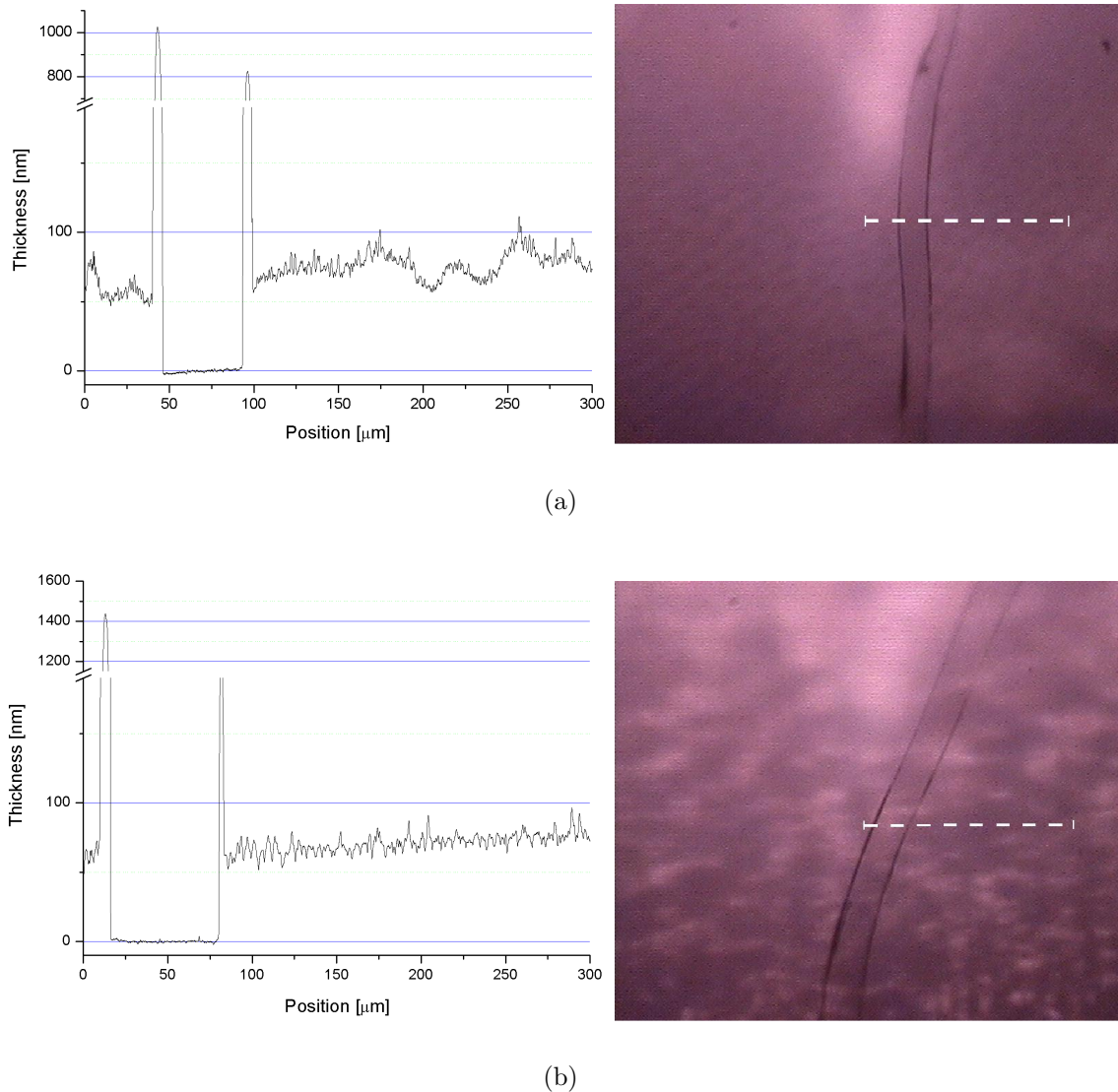
Figure 5.33: Two examples of depth profiles of DPS coatings measured with a profiler together with microscopic pictures of the corresponding regions (white dashed line depicts the scanning path); measured (a) at the center of the window and (b) 15 mm off the center. In both cases, the flat bottom area of the scratch is clearly visible both in the picture and in the profile. Spikes measured at both sides of the scratch are believed to be measurement artifacts and do not change the main conclusion that the coating is approximately 75 nm thick over the entire surface of the window.

temperature in the range of 140 – 190°C and, in consequence, solvents with higher boiling temperature (such as e.g. decalin with $T_B \approx 188°C$).

5.4.4   Tests at ILL

The main objective of the ILL measurements was the comparison between the quartz and DPS-coated Rexolite storage chambers in terms of neutron storage, compatibility with the mercury magnetometer and the HV performance.

The very first coating attempt in October 2007 had failed because of the problems with the DPS layer. Plasticizer from PVC gaskets used in the coating device got solved in the mixture of d-toluene and DPS and contaminated the coating. About 30% of the final product acquired jellylike consistency and did not stick well to the substrate. Nevertheless, the insulator was outgassed in vacuum (at 60°C, see Fig. 5.29) and tested at ILL. The vacuum performance and the compatibility with the ^{199}Hg co-magnetometer were satisfactory, however, because of the coating quality and poor HV stability it was decided to remove the coating by machining and coat it again.

The second coating attempt in December 2007, this time with additional Teflon foil separating the gaskets from the solution, resulted in a good hard quality coating, which was then outgassed at room temperature. The final commissioning of the new insulator for the storage chamber was performed at ILL in two steps in December 2007 and April 2008. In December it turned out that because of heavy outgassing from the insulator, the parameters of the ^{199}Hg-vapor magnetometer were far from the optimum and HV could be applied only when the neutron shutter in the chamber was kept opened (providing more access for pumping). Nevertheless, at least the measured storage and depolarization properties for the UCN were already encouraging. Fortunately, as described in the previous section, the outgassing problems could be solved and in April 2008, during the ILL cycle #150, the expected performance was reached, as described further down.

After measuring basic characteristics of the old quartz insulator of the nEDM spectrometer, it was replaced with the new one, equipped with DPE coated optical windows (see Fig. 5.34). The system was pumped, resulting in satisfactory conditions
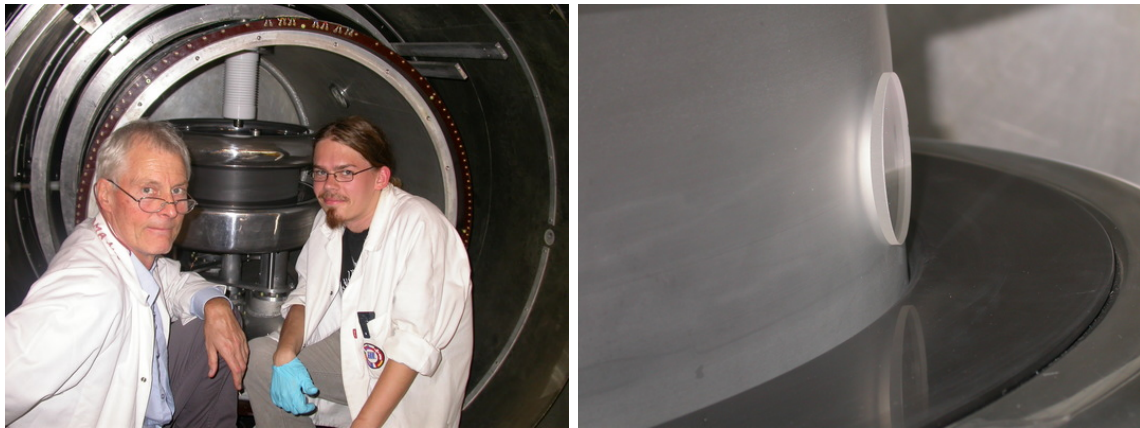
Figure 5.34: DPS-coated Rexolite chamber mounted at the nEDM setup. On the right, one of the DPE-coated windows inserted into the hole in the insulator.

after several hours ($p \approx 5 \cdot 10^{-5}$ mbar in the vacuum tank). Evidently the outgassing

from the plastic insulator was not an issue anymore and its overall vacuum behavior was as good as for quartz.

UCN storage We started with measuring the basic parameters of the chamber in terms of the UCN storage, namely storage and neutron polarization time constants.Following the normal measurement procedure (described in Sec. 3.3) but without the actual neutron precession phase (no neutron RF signal), we first measured the number of UCN stored as a function of the storage time, as shown in Fig. 5.35. The measurement was performed for both orientations of the main guiding magnetic field $\mathbf{B_0}$. The decrease in the number of UCN during the storage is dominated by

ILL Cycle	Material	$\mathbf{B_0}$	A_1	τ_1	A_2	τ_2	χ^2
#149	quartz	$\downarrow$	16323 (1264)	36 (6)	11212 (1884)	166 (23)	0.14
	DPS		17639 (1482)	34 (10)	18695 (2790)	136 (13)	0.47
#150	quartz	$\downarrow$	13120 (392)	43 (3)	7307 (484)	176 (7)	2.59
	DPS	$\uparrow$	14480 (464)	34 (3)	13487 (404)	195 (4)	2.80
	DPS	$\downarrow$	15828 (413)	31 (2)	13541 (323)	197 (4)	1.63

Table 5.8: UCN storage parameters of both insulators tested, fitted with a function $N_{\mathrm{UCN}}(t) = A_1 \, \mathrm{e}^{-t/\tau_1} + A_2 \, \mathrm{e}^{-t/\tau_2}$. See also Fig. 5.35.

the losses due to wall reflections, with a small contribution from the neutron decay process. Faster UCN make more reflections, so are more likely to be lost than the slower ones. Thus, in the most general form, the decay curve is a sum of exponentials corresponding to different velocity classes, each one with its own storage time constant. However, since fitting the storage data already with a sum of only two exponentials, $N_{\mathrm{UCN}}(t) = A_1 \, \mathrm{e}^{-t/\tau_1} + A_2 \, \mathrm{e}^{-t/\tau_2}$, gives reasonable χ^2 values, we decided to use it for characterization. The first time constant, τ_1, can then be attributed to a population of fast UCN, which are lost, because their energies are higher than the Fermi potential of the trap walls. The second time constant, τ_2, corresponds to the slower UCN, which survive. The parameters of the fits from Fig. 5.35 are summarized in Tab. 5.8. Clearly, the higher initial total number of UCN at the beginning of storage ($A_1 + A_2$) for DPS, indicates that due to its higher Fermi potential, more neutrons were accumulated in the chamber during the filling phase. The time constants for DPS are, given the accuracies, essentially consistent with those measured for quartz, which means that the losses are roughly the same for both materials. For the nEDM measurement, the most critical value is the absolute number of UCN after the storage time of typically 130 s. There is an 80% gain in the cycle #150 data, while the cycle #149 showed only a 25% gain.

Since the performance of the system and especially the overall number of measured neutrons had changed since the 2005 measurements, which were used to fine-tune the parameters of the GEANT4-UCN model, the simulation was again used to reproduce the results from #150 and find the most realistic loss probabilities per wall collision η. Several elements of the system have been exchanged, also our knowledge of the UCN guide quality has improved [133], which leads to a new updated properties table
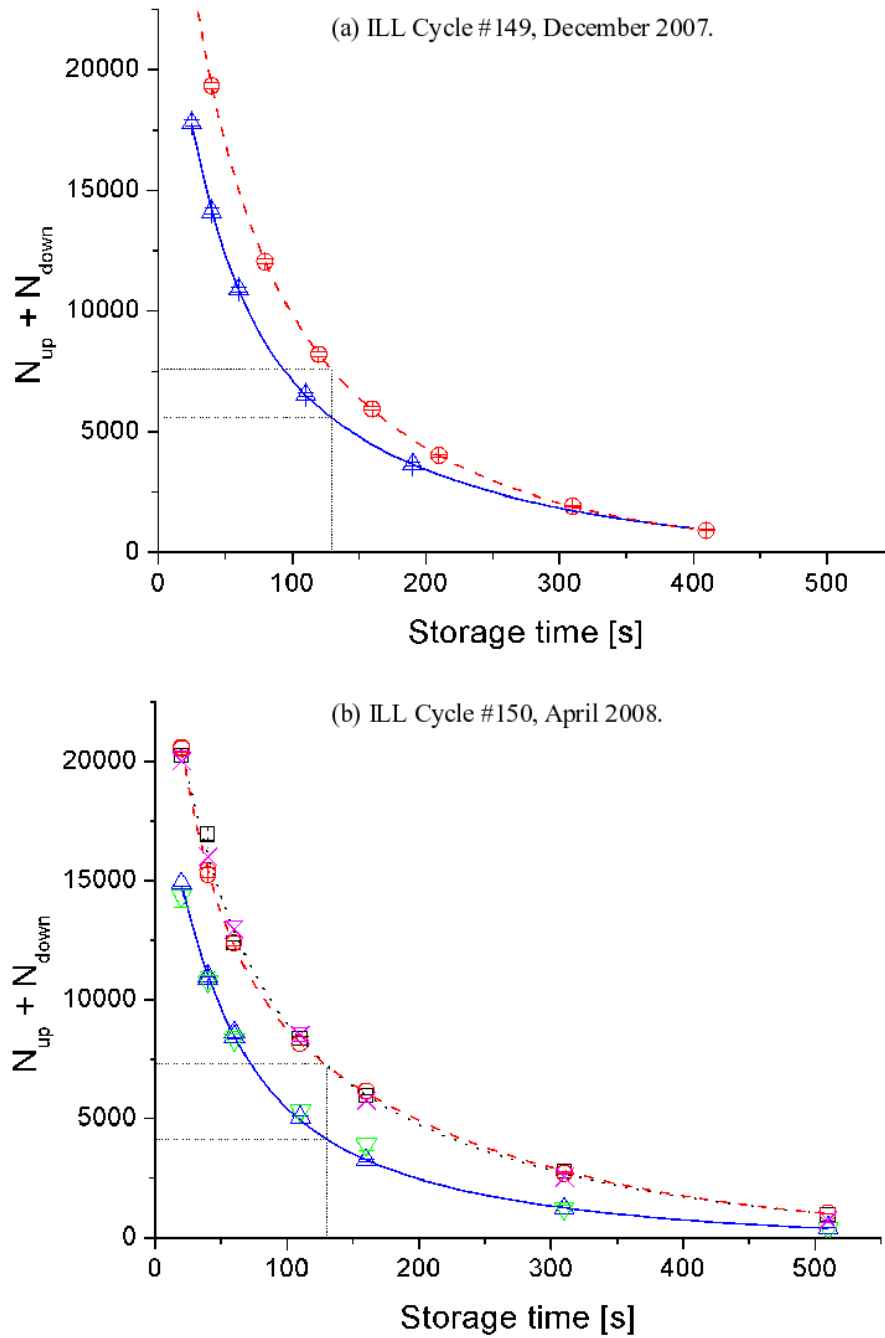
Figure 5.35: Total number of neutrons (both spin orientations) vs. storage times for the quartz insulator (blue $\triangle$) and the DPS-coated insulator. Storage curves are fitted with a sum of two exponentials. Concerning case (b), the DPS data for both magnetic field orientations: $B_0 \uparrow$ (black $\square$, dotted line) and $B_0 \downarrow$ (red $\circ$, dashed line) were taken two days after the quartz results had been obtained. The simulation results for (b) are also presented, both for quartz (green ∇) and DPS (magenta $\times$); see text for more details.

Part	Material	V_F [neV]	$\eta \cdot 10^4$	p_{diff}
Quartz Chamber	Fused Silica	90	4.5	0.1
	DLC	240		
DPS Chamber	DPS	162	3.0	0.1
	DLC	240		
Horizontal guide	NiMo	318	2.0	0.03
Vertical guide (bottom)	NiMo	318	2.0	0.03
Vertical guide (top)	Be	250	2.0	0.05
Polarizer	Fe	88	4.0	0.1

Table 5.9: Validated parameters of the model of the nEDM spectrometer at ILL: the Fermi potential V_F, loss probability per wall collision η and diffuse reflection probability p_{diff}.

(Tab. 5.9). Both quartz and DPS storage chambers were simulated (see Fig. 5.35). The Fermi potentials and diffuse reflection probabilities from Tab. 5.9 were assumed and for each case a series of storage curves for varying η of the storage volume was simulated. The best agreement with the measured values have been found with $\eta = 4.5$ for the quartz and with $\eta = 3.0$ for the new DPS insulator, reflecting the improved storage parameters (see Fig. 5.35).

The neutron polarization decay data are shown in Fig. 5.36(a). As before, no neutron RF pulse was applied during a cycle. In this case, already an exponential fit with a single time constant, T_1, can be used. By extrapolating the measured polarization asymmetry to $t = 0$ and taking the square root, one can estimate the analyzing power of the magnetized foil used in the experiment ($\approx 90\%$). Similar T_1 values were obtained for both orientations of the magnetic field. Values of a similar order have been also reached with the quartz insulator. However, since it tended to vary in time from one to another reactor cycle, it is hard to conclude, which chamber is better in terms of UCN depolarization. Definitely, T_1 values on this level are sufficient for a decent nEDM measurement.

The neutron depolarization time constant T_2 is related to polarization losses during the precession phase and it is mostly determined by the homogeneity of the magnetic field inside the storage volume and not by the wall collisions, as it is the case with T_1. It can not be directly associated with the quality of the insulator ring (unless magnetic inhomogeneities are introduced), nevertheless must be measured and maximized in order to conduct the Ramsey procedure. The precession phase is essential for the determination of T_2, therefore RF pulse at the neutron resonance frequency were applied close to the beginning and to the end of the storage time. Results are presented in Fig. 5.36(b) and again the data were fitted with single exponentials. As it was to be expected, the results are similar to those for the quartz insulator. T_2 for the "up" orientation of the $\mathbf{B_0}$ field is slightly worse, as it has usually been observed also before. In context of the nEDM experiment, one can already work with such values. However, given the values reported by the RAL/Sussex collaboration, it is clear that it could be still improved to about 600 s. The sudden drop of the T_2 value several years ago is probably related with a violent vacuum breakdown, which
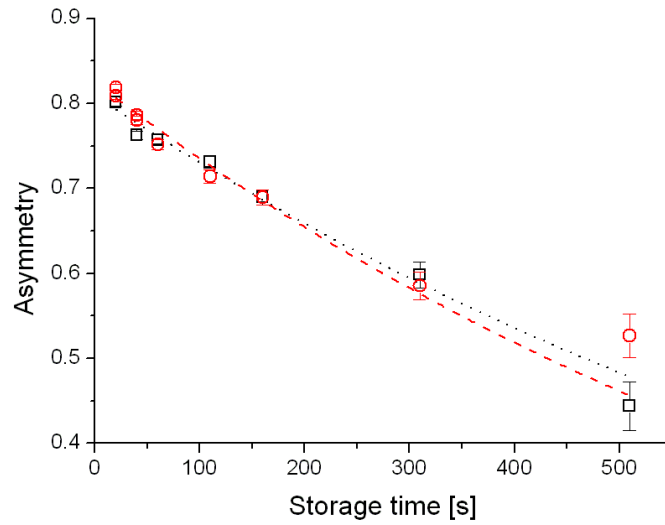
(a)
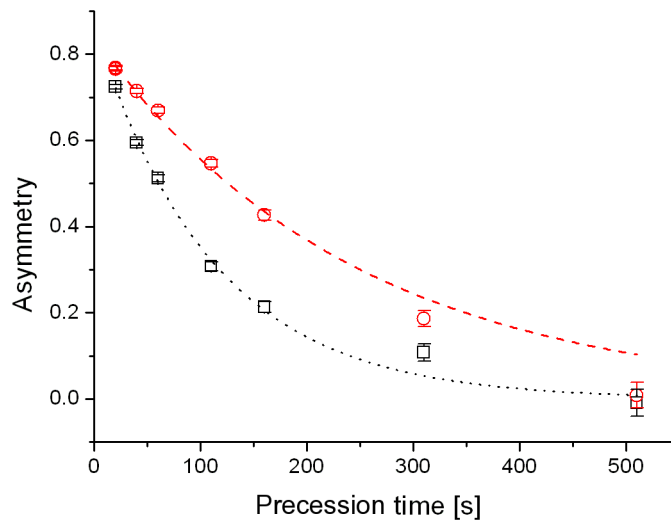
(b)

Figure 5.36: Spin up/spin down neutron asymmetry measured as a function of (a) the storage time and (b) the precession time. Data were taken with the DPS-coated insulator for both magnetic field orientations: $B_0 \uparrow$ (black $\square$, dotted line) and $B_0 \downarrow$ (red $\circ$, dashed line). Single exponential functions were fitted to the points (see text) and used to extract (a) T_1 and (b) T_2 time constants. T_1 values obtained from the fits are: 969 ± 54s (for $B_0 \uparrow$) and 861 ± 42s (for $B_0 \downarrow$). Results for T_2: 111 ± 4s (for $B_0 \uparrow$) and 243 ± 8s (for $B_0 \downarrow$).

destroyed a magnetic polarizer and possibly implanted some magnetic dipoles in the

vicinity of the storage volume. Since the value did not recover after the ring was exchanged, one can only conclude that the anomaly is located somewhere else.

ILL Cycle	Material	$\mathbf{B_0}$	T_1 [s]	T_2 [s]	$\sim\tau_{\text{Hg}}$ [s]
#149	quartz		644 (34)	116 (7)	90
	DPS	↓	588 (53)	118 (4)	50
#150	quartz	↓	770 (65)	140 (4)	45*
	DPS	↑	969 (54)	111 (4)	90
	DPS	↓	861 (42)	243 (8)	

Table 5.10: Depolarization storage parameters of both insulators tested for UCN and for the ^{199}Hg. τ_{Hg} value is approximately the maximal value achieved during normal operation of the system (i.e. with high-voltage). The result indicated with an asterisk is not representative, since it was not proceeded by the oxygen discharge cleaning ($\sim$90 s could have been probably reached with some discharge treatment).

Co-magnetometer The performance of the mercury co-magnetometer in the presence of DPE-coated windows has been already described in Sec. 5.4.3.2. But still the full DPS-coated insulator had to be tested together with the windows. The storage lifetime of the ^{199}Hg atoms is a good measure of the general tightness of the storage chamber. Of course, both neutron and Hg doors are kept shut throughout the measurement and there is a Teflon seal between the insulator and the electrodes, nevertheless, the Hg vapor still leaks through the slits at a certain rate. The value measured with the DPS-coated insulator was typically beyond 1100 s, which is significantly better than ~ 400 s obtained with the quartz insulator. So, apparently the new insulator fits better to the electrodes (or the windows are better fitted to the insulator), providing much beater sealing. In the experiment, the Hg atoms storage time should be significantly higher than the ^{199}Hg atoms polarization lifetime, τ_{Hg}, which is the most critical parameter of the co-magnetometer, as it determines its sensitivity at the end of the storage period. τ_{Hg} is completely dominated by the material on the surface of the chamber. Since the polarization decays exponentially in time, in order to be able to store neutrons for about two minutes with sufficiently sensitive magnetic field monitoring, a polarization decay time constant, τ_{Hg}, of at least 60 seconds is required. The Sussex/RAL collaboration used to take data with τ_{Hg} usually between 60 and 100 s (see e.g. [55, Fig. 9.1]). It was important to repeat that performance also with the DPS-coated insulator, especially in view of the values of τ_{Hg} given by May [55, Tab. 2.51]: 125 s for quartz, but only 80 s for DPS. Oxygen
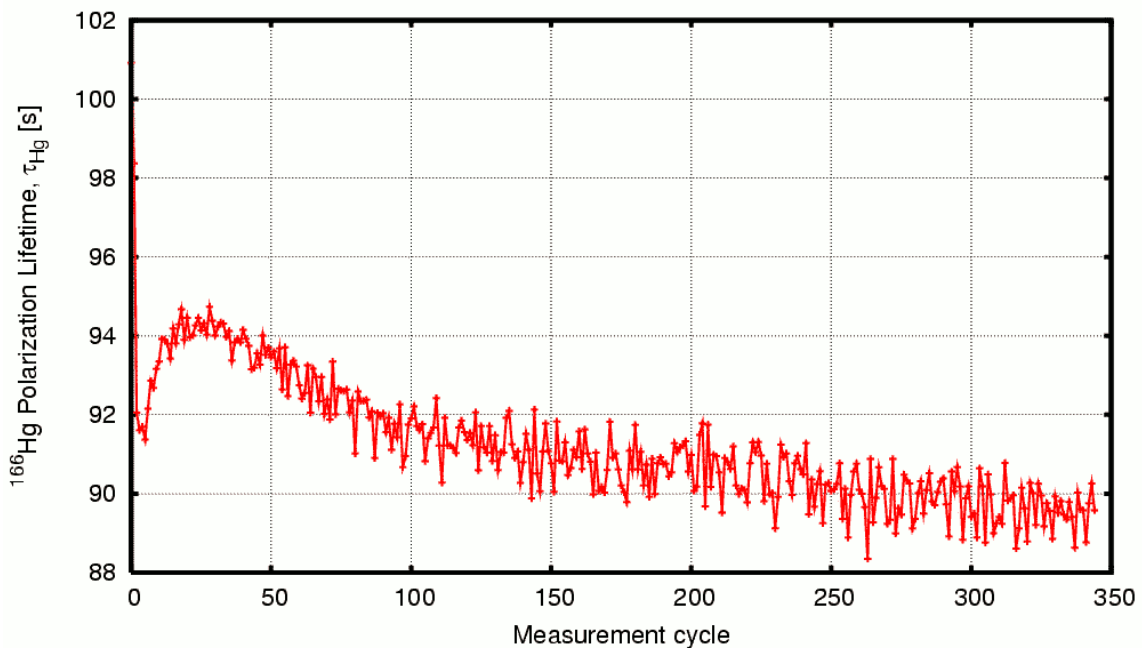
Figure 5.37: Evolution of the ^{199}Hg atoms polarization lifetime measured in a series of cycles, where each cycle takes approximately 140 s. The co-magnetometer usually needs some time to reach the stability and optimal sensitivity; in this figure first five cycles should be disregarded. High-voltage was slowly ramped from 0 to $+80\,\mathrm{kV}$ between the cycles 20 and 100.

discharge cleaning is a standard procedure used to clean the inner surfaces of the storage chamber of chemical impurities, responsible for ^{199}Hg vapor depolarization (see [55, Sec. 7.3.4.1]). We performed the discharge cleaning procedure several times over a couple of days, starting with τ_{Hg} of about 30 s and ending up with 98 s. Usually, the value decreases a little within the first quarter of an hour after the cleaning and then settles down at some level, where it remains almost stable for days. If a high-voltage spark occurs or the electric field polarity is reversed, it drops and slowly recovers or has to be recovered artificially with the discharge cleaning. In this particular case, while the voltage was being ramped to +80 kV, luckily with no sparks, the τ_{Hg} slightly decreased to $\sim$90 s, where it remained for longer. After some further HV training, with considerable number of sparks and a couple of polarity reversals, τ_{Hg} stabilized at about 70 s. The overall performance was very similar or to that with the quartz insulator or even slightly better.

High-voltage   During the ILL cycles #149 and #150 we used two manually operated unipolar HV power supplies[29], which provided $\pm$138 kV voltage and up to 200 μA current. Each time after closing the vacuum tank and pumping, a considerable amount of time and much patience is necessary to reach the maximum voltage. Flashover discharges remove dust particles, other contaminants and microscopic inhomogeneities from the insulator surface. The system must be first "cleaned" in this way before it can operate in a stable way at HV and one has to constantly monitor the current and be careful not too damage the chamber by too quick or to violent training. Within a couple of days the maximum negative voltage was reached; stable and safe operation was proven up to -125 kV (with an overnight Ramsey scan, see below). The positive polarity has always been much more problematic, also with the quartz insulator. Although +100 kV was reached, the system was not sufficiently stable beyond +90 kV (a successful overnight Ramsey scan was performed only at +80 kV). Partially it can be explained by the power supply defect (dysfunctional current limiter at positive voltages) and the way the power supply was connected to the HV cable. This feature should be definitely studied and improved in the future, since there was no means to do it during the cycle #150.

Addition into the gas system of a controlled small amount ($10^{-4} - 10^{-3}$ mbar) of Helium, which is a highly electronegative, improves the stability of the system and increases the flashover voltage. The nEDM apparatus vacuum system provides a convinient way to introduce the gas and keep its flow on a stable level and this feature has been widely used in the Sussex/RAL/ILL experiment. Also in our case, reaching voltages beyond 100 kV with Helium was much less time consuming.

Each time when too many (several) sparks occurred in a short period of time ($\sim$2 minutes), the pressure inside the storage chamber would rise, leading to higher leakage currents and general instability of the system. It is then necessary to decrease the voltage to a stable value and give it a couple of minutes to stabilize, before the voltage can be safely raised again.

---

[29]Model SL130 from Spellman, used at ILL as an "emergency" solution, after the old bipolar HV generator broke down.
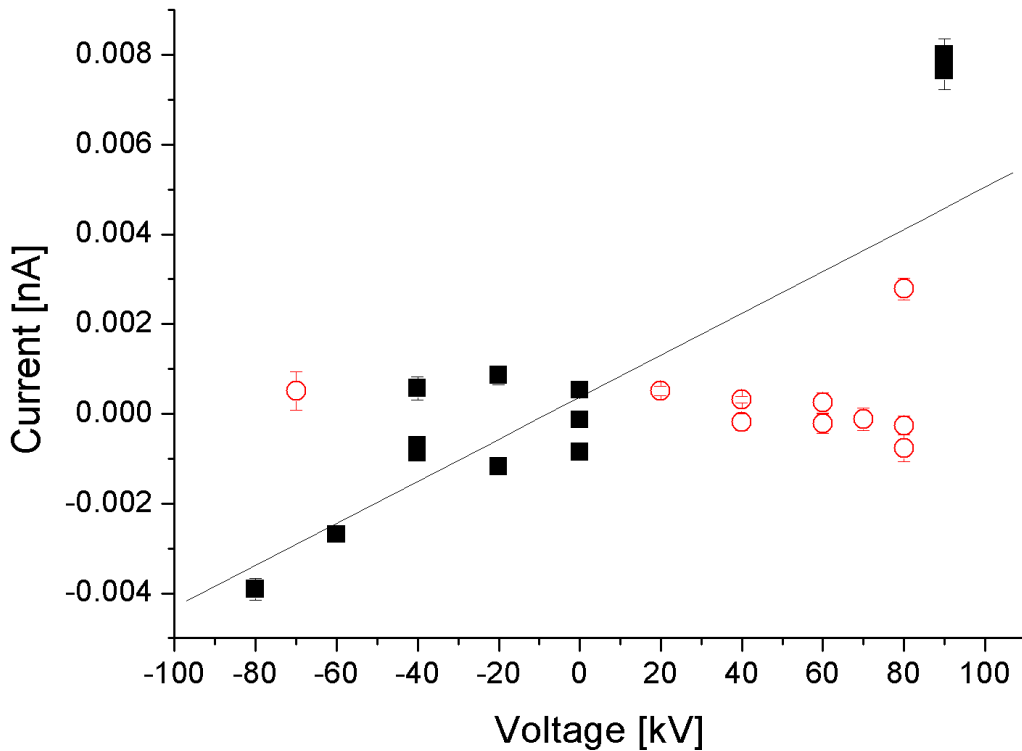
Figure 5.38: Measured current versus applied voltage for the DPS-coated insulator. Because of the problems with the general stability and reproducibility of the setup, the resistance estimate obtained from the linear fit has to be treated as a rough estimate. To obtain the most conservative estimate only the extreme points (black squares) were taken into account for the fit.

We also attempted to measure the resistance of the new chamber, using a picoammeter[30] to monitor the current flow between the bottom electrode and the grounded vacuum tank. For protection, two $700\,\mathrm{M\Omega}$ high-voltage resistors were installed in series before the device. Despite a general problem with the stability and reproducibility of the measurement, some rough resistance estimate can be made. Measured values of current plotted against the used voltage were fitted with a line (see Fig. 5.38) and a rough resistance value $R = 2.1 \times 10^{16}\,\Omega$ was extracted from the slope. This can be translated to (volume) resistivity, ρ, of the material, resulting in $\rho = 3.2 \times 10^{17}\,\Omega \cdot \mathrm{cm}$. The leakage current measurement problem has to be certainly solved in the future in order to make a reliable and precise current monitoring possible. Nevertheless, almost two orders of magnitude safety margin over the minimal requirement of $10^{15}\,\Omega \cdot \mathrm{cm}$ (see p. 40) gives us the confidence that the electrical properties of the insulator are sufficient.

---

[30]Keithley M6487.

Final tests   The final performance test was performing overnight Ramsey scans at both high-voltage polarities. In this way realistic data taking conditions are reproduced and simultaneous operation of all subsystems (co-magnetometer, shutters, high-voltage) can be tested. Several scans were performed at different positive and negative voltages and an example for $-125\,$kV is presented in Fig. 5.39.
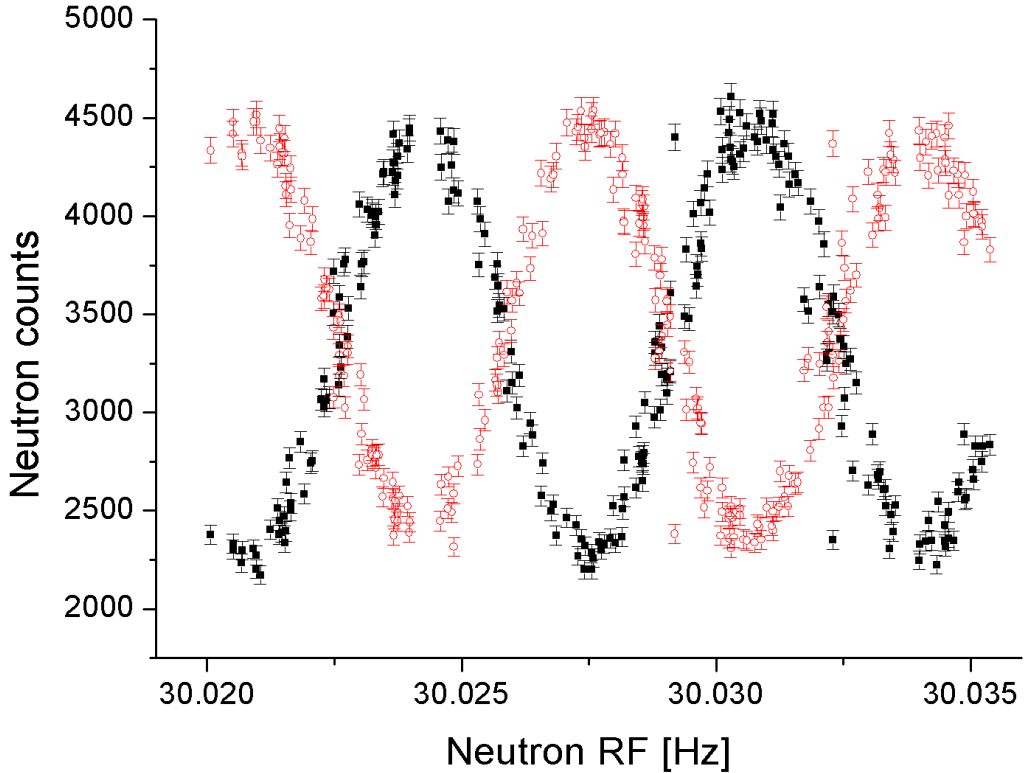
Figure 5.39: Ramsey scan #89, measured at $-125\,$kV for $150\,$s precession time. Neutron spin up and spin down counts are depicted as black squares and red circles, respectively. Two central fringes of the Ramsey resonance pattern (see also Fig. 3.1) are visible.

The data presented was corrected for the changes in the magnetic field with the co-magnetometer measurements (τ_{Hg}=70 s, Hg leakage time 1200 s, absorption $\sim$17 % and polarization $\sim$34%). The Ramsey pattern is clearly visible, which demonstrates full functionality of the system with the new DPS-coated ring at typical running parameters (T=150 s, $B_0\downarrow$) and with high-voltage applied.

5.5   Summary

In order to find the best material for the UCN storage chamber of the nEDM experiment, extensive material studies have been made. Various insulating materials,

including ceramics and thermoplastic coatings have been considered as candidates for the chamber wall and tested for electrical and other properties. In addition to this several types of high Fermi potential coatings have been developed, applicable on the inner walls of the chamber, in case the base material was not suitable for UCN storage.

An initial attempt to use hot filament CVD diamond coatings failed, because of an unspecified conductive layer present between the coating and the substrate materials. The existence of such a layer was found, but its exact nature remains unknown. Thus, diamond coatings were disregarded because of the insufficient electrical resistivity. Another material, Si_3N_4 which was promising because of its excellent electrical and HV performance and high Fermi potential, was shown to be incompatible with the mercury co-magnetometer in the nEDM experiment. Si_3N_4 causes rapid depolarization of the polarized ^{199}Hg vapor, which is used to monitor the magnetic field changes inside the chamber during the storage.

Therefore, thermoplastic polymers were investigated in more detail, in particular, an idea to use a thermoplastic insulator coated from inside with a high Fermi potential deuterated coating. While our attempts with Si_3N_4 and diamond were pioneering, the deuterated coatings had been already used in the past [127] – in a different way, though, than we did – and had been abandoned due to HV problems [134]. Finally, Rexolite (cross-linked polystyrene), was found to be suitable, due to its electrical/mechanical properties and a new method of producing DPS coatings was developed. Another polymer, DPE, was chosen for inner coatings of the co-magnetometer optical windows of the nEDM storage chamber and a spin-coating technique of producing optical quality thin coatings was optimized. The Fermi potential of both deuterated polymers was then measured by means of cold neutron reflectometry and the theoretical values were confirmed. It was the first such measurement for DPE – a very promising material, which may find a lot of applications in experiments with UCN in the future.

The material research program resulted in a new DPS-coated Rexolite chamber with two DPE coated optical window for the ^{199}Hg co-magnetometer readout. The new chamber was extensively tested at ILL in the existing nEDM apparatus. The high-voltage performance and the compatibility with the co-magnetometer turned out to be similar to those of the old quartz insulator. Due to the higher Fermi potential of DPS, more neutrons could be stored in the chamber, leading to about 50% gain in the UCN number after 130 s of storage. A conservative estimate of the new chamber resistance has been also made with a limited success, because of the measurement stability problems. This estimate is almost two orders of magnitude above the experiment requirements, which provides a good safety margin. Thus, it can be concluded, that the main goal has been reached and the new solution can be now used in the next phases of the nEDM project.

Chapter 6

Experimental limit on neutron - mirror neutron oscillations

6.1 Motivation

Recently it was pointed out [135] that no direct experimental limits exist on the time of the oscillation ($\tau_{\mathrm{nn'}}$) between ordinary matter neutrons (n) and the speculative mirror neutrons (n'). $\tau_{\mathrm{nn'}}$ is the time after which one finds with 100% probability a mirror neutron when starting initially from a neutron). An indirect limit of the order $\tau_{\mathrm{nn'}} \geq 1\,\mathrm{s}$ has been derived in [135] based on the search for neutron – antineutron (n$\bar{\mathrm{n}}$) oscillations [136]. Fast nn' oscillations with $\tau_{\mathrm{nn'}} \sim 1\,\mathrm{s}$, or at least much shorter than the neutron β-decay lifetime, could explain [135,137] the origin of ultra-high energy cosmic rays (UHCR) above the Greisen-Zatsepin-Kuzmin (GZK) cutoff [138,139] The viability of models and implications have been further discussed in [49].

We note, however, that several months after the result presented below had been published, some new data on UHCR appeared, which showed no events beyond the GZK cutoff [140,141]. Thus, the discrepancy with theoretical predictions seems to be resolved now, which obsoletes this particular aspect of our motivation. But still, even without the GZK anomaly, the mirror matter hypothesis and the possibility of nn' oscillations are not excluded. Therefore, because of its sensitivity for new physics, the search for the oscillations is worth pursuing and there are some further plans at PSI to further improve the limit using the new intense UCN source.

Possible approaches to nn' oscillation experiments with sensitivities of several hundred seconds have been discussed by Pokotilovski [142]. One approach is to search for nn' oscillations by comparing the storage of ultracold neutrons (UCN) in vacuum in a trap in the presence and the absence of a magnetic field, respectively. The essential idea is that the neutron and mirror neutron states would be degenerate in absence of both ordinary and mirror magnetic fields and nn' transitions could occur. The interaction of the neutron with a magnetic field would lift the degeneracy and suppress the transition into a mirror neutron, which, of course, does not interact with the ordinary magnetic field, nor with the trap via the ordinary strong interaction. Thus, the oscillation into mirror neutrons adds a loss channel for ultracold neutron storage. If nn' transitions occurred, the storage time constant for ultracold neutrons
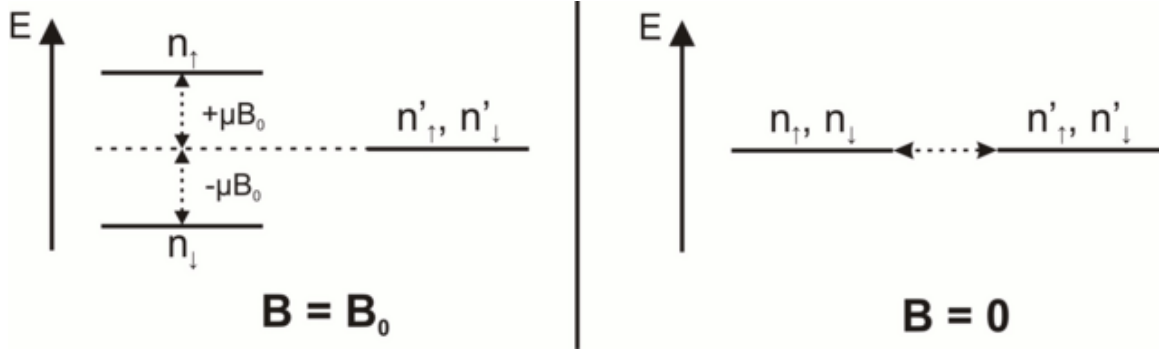
Figure 6.1: Energy scheme for the two cases: field on ($B = B_0$) and field off ($B = 0$). $n_\downarrow$ and $n_\uparrow$ denote the spin-up and spin-down neutrons; n'$_\downarrow$ and n'$_\uparrow$ the corresponding mirror neutrons.

in a trap with magnetic field would be longer than without magnetic field.

Although degeneracy and oscillations could also occur when non-zero ordinary magnetic field was compensated by apropriate mirror magnetic field, the absence of mirror magnetic fields at the location of the experiment is assumed throughout this chapter. It is an important assumption, since it is hard to arbitrarily exclude existence of such fields of extraterrestrial or terrestrial origin. One can derive only a rather weak limit on the mirror magnetic field strength from the existing limit on the amount of mirror matter inside the Earth, see [143]. Mirror magnetic fields on the Earth are often assumed to vanish in the literature (see, e.g., [135, 142]), but one can also consider their existence in some special cases [144].

One should note that this disappearance method only measures neutron loss as a function of applied magnetic field. A signal will not prove the oscillation into mirror neutrons, only that some magnetic field dependent loss channel exists. By assuming that the nn' oscillation is responsible for the loss, limits can be set on $\tau_{nn'}$. One can imagine other exotic disappearance channels for the neutron, among which only the antineutron channel is tightly constrained [136].

6.2   Formalism

The formulation of the nn' oscillation is analogous to the evolution of other simple two state systems such as spin $\frac{1}{2}$, $K^0\bar{K}^0$, or $n\bar{n}$ mixing (see, e.g., [145, 146]). The energy difference between neutron and mirror neutron states due to magnetic field interaction with the neutron magnetic moment μ_n is $\mu_n B$ (see Fig. 6.1). All the other physical characteristics (mass, decay width, gravitational potential) are exactly the same for both ordinary and mirror neutrons. The time evolution of such a two state system is given by the effective Hamiltonian

$$H = \begin{pmatrix} \frac{p^2}{2m_n} - \mathrm{i}\,\frac{\Gamma}{2} + V & \delta m \\ \delta m & \frac{p^2}{2m_n} - \mathrm{i}\,\frac{\Gamma}{2} + V' \end{pmatrix}, \tag{6.1}$$

where Γ is the decay width and the splitting, $\delta m = \tau_{nn'}^{-1}$, determines the oscillation time. The mixing between both states would emerge from the effective six-fermion interaction $G(udd)(u'd'd')$, with a dimensional coupling constant $G = 1/M^5$ (where M is the relevant mass scale), leading to $\delta m \sim (10\,\text{TeV}/M)^5 \times 10^{-15}\,\text{eV}$. Theoretically, the effective interactions can be induced via exchange of extra heavy states between the mirror and the ordinary sector [137, 49]. In absence of the mirror potential V', the energy difference between both states is simply proportional to the ordinary (magnetic) potential $V = -\mu_n B$. For convenience we adopt the notation of [142, 147] and define a characteristic frequency $\omega \equiv \frac{\mu_n B}{2\hbar}$ which corresponds to half the energy splitting.

The probability p for an UCN to be found as a mirror neutron after a time t can then be written as

$$p(t) = \frac{\sin^2(\sqrt{1 + (\omega\tau_{nn'})^2} \times t/\tau_{nn'})}{1 + (\omega\tau_{nn'})^2} \,. \tag{6.2}$$

The time t is limited by the free flight time t_f between two wall collisions, because each wall collision probes whether an oscillation has taken place. At the collision moment, strong interaction between ordinary neutrons and the UCN trap dominates the behavior of the system and the degeneracy is removed: the ordinary neutron interacts with the wall and is reflected, the mirror neutron leaves the storage chamber. As the strong potential was not taken into account in the effective Hamiltonian from Eq. 6.1, Eq. 6.2 cannot be applied there, either. The wall collision frequency is determined by $\frac{1}{t_f}$. Between wall collisions the effective transition rate of UCN into mirror neutrons is then given by

$$R = \frac{1}{t_f} \int_0^{t_f} \frac{dp}{dt}\, dt = \frac{1}{t_f} p(t_f) \,. \tag{6.3}$$

For a real system, which consists of a large number of UCN with various velocities, the factors on the right hand side of Eq. 6.3 must be properly averaged over the distribution of flight times between collisions during the storage time t_s:

$$R_s = \frac{1}{\langle t_f \rangle_{t_s}} \langle p(t_f) \rangle_{t_s} \,. \tag{6.4}$$

In experiments, one searches for a weak coupling, thus long $\tau_{nn'}$: so in practice $\omega\tau_{nn'} \gg 1$ in Eq. 6.2. Two limits are considered for Eq. 6.2: In the first case ("$\uparrow\downarrow$", large B-field applied either in the direction up or down), $\omega_{\uparrow\downarrow} t_f \gg 1$, many oscillations take place and the $\sin^2(\,)$ term of Eq. 6.2 is averaged to $\frac{1}{2}$ because t_f varies along UCN trajectories:

$$R_{s,\uparrow\downarrow} = \frac{1}{\langle t_f \rangle_{t_s}} \frac{1}{2(\omega_{\uparrow\downarrow}\,\tau_{nn'})^2} \,. \tag{6.5}$$

In the second case ("0", small B-field), $\omega_0 t_f \ll 1$, the n′ component grows quadratically in time during the free flight:

$$R_{s,0} = \frac{1}{\langle t_f \rangle_{t_s}} \frac{\langle t_f^2 \rangle_{t_s}}{\tau_{nn'}^2} \,. \tag{6.6}$$

Also regular losses of UCN must be considered, such as absorption and upscattering (during wall interactions or in collisions with rest gas), trap leakage and β decay. All these loss mechanisms contribute to the UCN storage time constant τ_{store} of the system; $\lambda_{\text{store}} = 1/\tau_{\text{store}}$ is the corresponding loss rate. Generally, the loss rate depends on UCN energy and for a spectrum of stored UCN the decay curve is a sum of exponentials. The total effect can be modeled by the relative populations c_i of different velocity classes, each with its own storage loss rate $\lambda^{(i)}$. After storing an initial number $n(t{=}0)$ of UCN for some time t_s in a given magnetic field one will detect the number of surviving UCN

$$n(t_s) = n(t{=}0) \times \sum_i c_i \exp[-(\lambda^{(i)}_{\text{store}} + R_s)\, t_s]\,. \tag{6.7}$$

with the simple normalization condition $\sum_i c_i = 1$. For measurements in the limits $\uparrow\downarrow$ and 0 (only the magnetic field is changed), the ratio of detected UCN becomes independent of all the regular UCN loss mechanisms

$$N_{0/\uparrow\downarrow} \equiv \frac{n_0(t_s)}{n_{\uparrow\downarrow}(t_s)} = \exp[(R_{s,\uparrow\downarrow} - R_{s,0})\, t_s]\,. \tag{6.8}$$

In the absence of other effects, neutron – mirror neutron oscillations lead to $N_{0/\uparrow\downarrow} < 1$.

6.3 The direct measurement of n-n' oscillations

We have performed UCN storage experiments at the Institut Laue-Langevin using the experimental setup of the neutron EDM experiment, described in Sec. 3.2 (see also [148, 14]). A typical measurement cycle consists of (i) a filling time of 40 s with the beam switch connecting the storage chamber to the ILL PF2 EDM beam line [2] allowing *unpolarized* UCN to enter the storage volume, (ii) different storage times t_s when the UCN isolation shutter to the storage chamber was closed and (iii) 40 s counting time with the UCN shutter open and the beam switch connecting the storage chamber to the ^{3}He filled UCN detector[1]. It was checked that further increasing the counting time did not significantly affect the number of counted neutrons. The neutron polarizing/analyzing foil was removed for the experiment. The pressure inside the storage chamber was always better than 10^{-3} mbar in order to make sure that the nn' degeneracy is not lifted by the interaction of UCN with the rest gas.

The UCN storage chamber has a volume $\mathcal{V} \sim 21$ l and a surface area of $A \sim 5400\,\text{cm}^2$. The limit for stored UCN velocities is 4.1 m/s. From kinetic gas theory, the mean free path of UCN between wall collisions is $\frac{4\mathcal{V}}{A} \approx 0.16$ m, the mean velocity is about 3 m/s [28] and, thus, $\langle t_f \rangle \approx 0.053$ s. One obtains $\omega \cdot \langle t_f \rangle \sim 1$ at a magnetic field of $B \sim 0.42\,\mu$T; the limiting cases are obtained for magnetic fields of more than a few μT ($\uparrow\downarrow$) and of less than a hundred nT (0), respectively.

Different magnetic field configurations were used: up ($B_\uparrow$), off ($B_0 = 0$) and down ($B_\downarrow$). The strength of the magnetic field was adjusted by the current through the main
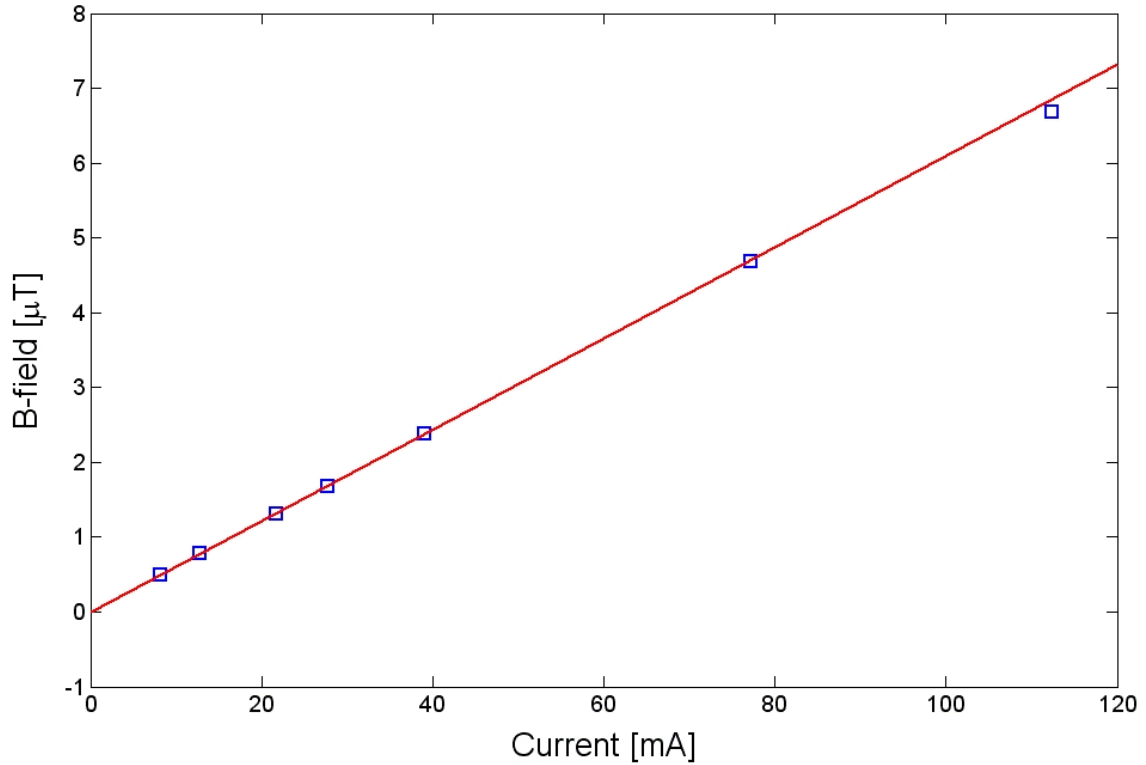
---

[1]from A. V. Strelkov, JINR Dubna, Russia.

Figure 6.2: Dependency of the B_z component of magnetic field as measured with the Hg magnetometer on the current applied to the main coil. The data were fitted using a linear function $B[\mu\mathrm{T}] = -0.0023 + 0.061 \cdot I[\mathrm{mA}]$ (red line).

magnetic field coil. The relevant measurements were taken at $|B_{\uparrow\downarrow}| \approx 6\,\mu\mathrm{T}$ (100 mA). The magnetic field (B_z, along the main magnetic field direction) as a function of the applied current was measured using the Hg cohabiting magnetometer [54] for fields between $0.3\,\mu\mathrm{T}$ and $7\,\mu\mathrm{T}$. For lower fields the Hg magnetometer could not be used. The Hg data set shows a perfectly linear dependence of the field on applied current and results in $|B_{z,0}| = 2.3 \pm 2.6\,\mathrm{nT}$ when extrapolated to zero current (see Fig. 6.2). The shielding factor of the μ-metal shield was measured to be of the order of $10^{-4} - 10^{-3}$ for all three axes (Tab. 3.1). Since the ambient field at ILL is of the order of $10\,\mu\mathrm{T}$ for each of the components, one can assume, that the residual magnetic field inside the shield has no preferred spatial direction or no dominant component, much larger than the other two. Taking the 95% C.L. upper limit for the B_z field and using it also for B_x and B_y indicates a residual absolute B-field below $13\,\mathrm{nT}$.

The zero field B_0 for the actual measurements was set by switching off the coil current and demagnetizing the four-layer μ-metal shield surrounding the storage chamber. We also used 3-axis fluxgate sensors directly above the storage chamber in order to verify that the residual B-field was sufficiently small for the purpose of our experiment (see Sec. 3.2.4 for more detail on the location of the fluxgate). The B-field configurations of the experiment were very well reproducible, in particular B_0 within less than $1\,\mathrm{nT}$. The direct limit on $|B_0|$ obtained from the fluxgates is, however, some-

$t_s\,[\mathrm{s}]$	50 (a)	50 (b)	100 (a)	175 (a)
$t_s^*\,[\mathrm{s}]$	73 ± 3 (a)	73 ± 3 (b)	123 ± 3 (a)	198 ± 3 (a)
$n(B_0)$	44317 ± 40	44363 ± 53	28635 ± 21	17015 ± 22
$n(B_\uparrow)$	44197 ± 53	44443 ± 53	28671 ± 30	17047 ± 31
$n(B_\downarrow)$	44128 ± 53	44316 ± 46	28596 ± 30	16974 ± 31
$n(B_{\uparrow\downarrow})$	44163 ± 38	44371 ± 35	28633 ± 22	17011 ± 22
$N_{0/\uparrow\downarrow}$	1.0035(13)	0.9998(15)	1.0001(11)	1.0002(18)
	1.0019(10)			

Table 6.1: Measured total UCN counts n normalized per cycle for the day sequences ((a), (b), see text) at different storage times t_s^* (with systematic error) and magnetic field configurations. $n(B_{\uparrow\downarrow})$ is the weighted average of $n(B_\uparrow)$ and $n(B_\downarrow)$, and $N_{0/\uparrow\downarrow} = n(B_0)/n(B_{\uparrow\downarrow})$.

what weaker: it was found that the connectors of the commercial devices are slightly magnetic, leading to offset fields at the location of the sensor on the order of 25 nT. Although the residual field is probably on the level of a few nT, we give a conservative limit of $|B_0| < 50\,\mathrm{nT}$, which is sufficient for our purpose here, i.e., for the limiting case "0".

Most of the measurements were performed repeating the sequence (a) (B_0, $B_\uparrow$, $B_\downarrow$, B_0, B_0, $B_\downarrow$, B_0, $B_\uparrow$) with field changes typically every 1.5 h during day time. The demagnetization procedure before B_0 measurements took about half an hour. For a given B-field configuration 16 UCN cycles were measured: 4 for each storage time of $t_s = 100\,\mathrm{s}$, 50 s, 175 s, and again 100 s. Night runs were taken for longer periods at one B-field configuration with $t_s = 100\,\mathrm{s}$. They were used to check on the long term stability of the system. It was found that drifts of the count rates were slow and on a level below 0.3% over several hours. This agrees in magnitude with changes in the reactor power, but a direct correlation could not be established, for several reasons. Firstly, the reactor power data was available only in a form of one minute averages, not necessarily coinciding with the actual filling periods. Secondly, the experiment lacked a reliable independent monitoring of the incoming beam intensity, which is certainly to be improved for the next generation experiment. The count rate drifts were sufficiently slow to be averaged out in the day runs with frequent changes of the B-field configuration. For $t_s = 50\,\mathrm{s}$ some data was taken using another sequence (b), ($B_\uparrow$, $B_\downarrow$, B_0) while checking on an unexpected count ratio $N_{0/\uparrow\downarrow}$ (see below).

The time constant for UCN to leave the storage chamber with the shutter open was measured to be $\tau_{op} = 11.4 \pm 0.6\,\mathrm{s}$. Mirror neutrons can leave the system also during filling and counting. The relevant average times t_s^* in our storage system are thus longer than the times between closing and opening the UCN shutter. One can replace t_s in Eq. 6.8 by t_s^* and, because R_s changes only weakly with t_s and τ_{op} is much smaller than t_s, one finds to very good approximation $t_s^* = t_s + 2\,\tau_{op}$. We assign a conservative systematic error of $\pm 3\,\mathrm{s}$ to t_s^*.
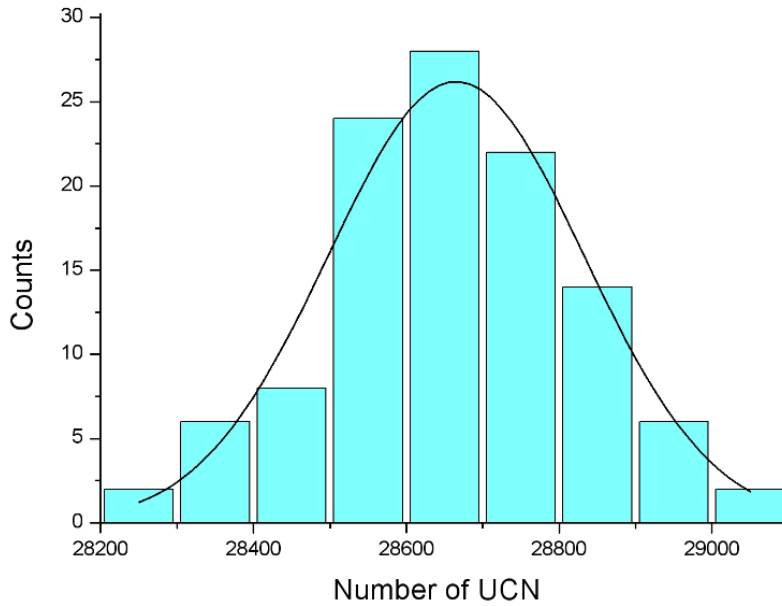
Figure 6.3: Distribution of UCN counts for 100 s storage time measurements [5]. It is consistent with Gaussian distribution (solid curve), which justifies the statistical averaging of data. Parameters of the fitted gaussian distribution, $y = A \cdot e^{-\frac{(x-x_0)^2}{2\sigma^2}}$, are: $A = 26 \pm 3$, $x_0 = 28665 \pm 18$ and $\sigma = 167 \pm 16$.

For data analysis, the results for each B-field configuration were first treated separately. The distributions of single-cycle counts $n(t_s)$ were found to be consistent with Gaussians with standard deviations $\sigma \approx \sqrt{n}$ with no additional systematics (see Fig. 6.3). The counts per cycle for each configuration were thus statistically averaged, see Table 6.1. The averaged numbers of counts show a presently unexplained tendency to a linear dependence on the magnetic field (see also Fig. 6.4). The effect we wish to limit depends on $|B|^2$ (via ω^2), so the direct average of the $+6$ and -6 μT measurement values cancels the linear systematic effect, leaving only the possible oscillation effect and any remaining quadratic systematic contributions.

The averaged numbers of UCN counts are then used to calculate the count ratios $N_{0/\uparrow\downarrow}$ according to Eq. 6.8. For 50 s storage time and sequence (a), the count ratio $N_{0/\uparrow\downarrow}$ is larger than 1 by 2.7 standard deviations, which led us to remeasure at this storage time (using sequence (b)) and corroborate that this deviation was a statistical fluctuation. Both ratios $N_{0/\uparrow\downarrow}(50\,\mathrm{s})$ are given in the table along with the obtained average. The individual results for $N_{0/\uparrow\downarrow}$ show no signal ($N_{0/\uparrow\downarrow} < 1$) within their respective error bars and, as they are independent, can be used in a combined analysis. Following Eq. 6.8, we write $N_{0/\uparrow\downarrow} = \exp[a\,t_s*]$ with a fit parameter a. The fit gives $a = (5.38 \pm 5.78) \times 10^{-6}$ s^{-1} (see Fig. 6.5). We use this value at the limit of the experimentally measured range ($t_s^* = 198$ s) to set the constraint on the neutrons which may have been lost, yielding

$$N_{0/\uparrow\downarrow}(t_s^* = 198\,\mathrm{s}) = 1.00106 \pm 0.00114\,. \tag{6.9}$$

Results with $N_{0/\uparrow\downarrow} > 1$ are unphysical for nn' oscillations. In order to derive a
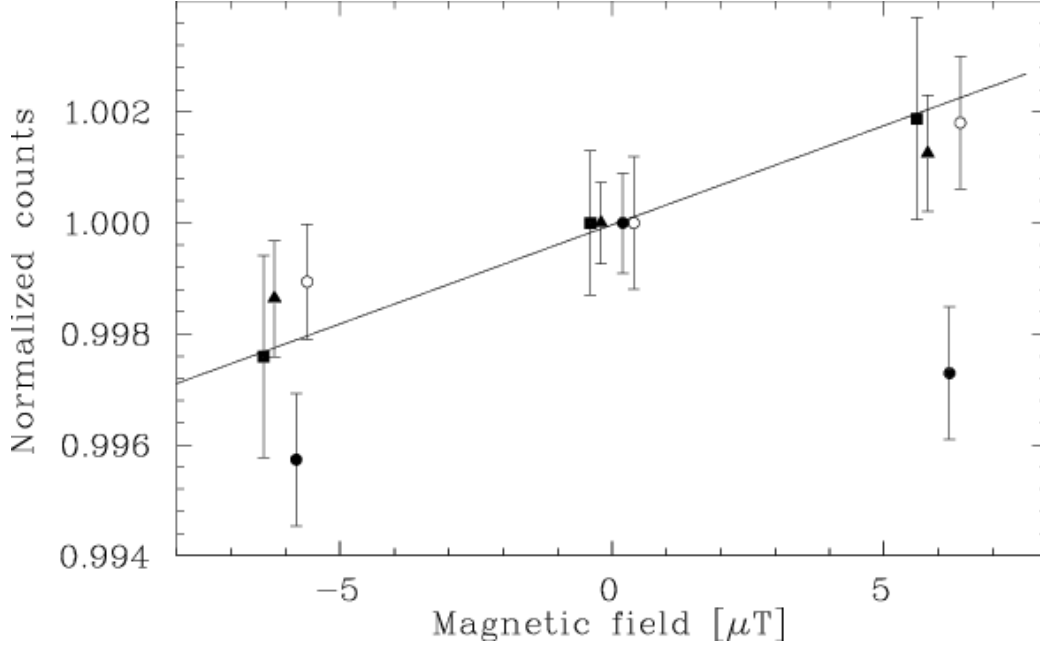
Figure 6.4: Number of UCN counts vs. the magnetic field. The counts are normalized to the "zero" field average. The points represent the data taken at storage times of: 100 s (triangles), 175 s (squares), and 50 s (full and empty circles for datasets (a) and (b), respectively). Measurements were done at -6, 0, and $+6\,\mu$T only, in the figure points are artificially spread for better visibility.

limit on $N_{0/\uparrow\downarrow}$ we adopt the Bayesian approach described by the Particle Data Group (page 305 of Ref. [8]: probability distribution set to zero for $N_{0/\uparrow\downarrow} > 1$). One obtains:

$$N_{0/\uparrow\downarrow}(t_s^* = 198\,\text{s}) > 0.99835\,\text{s}\,(95\%\,\text{C.L.}). \tag{6.10}$$

In order to derive the limit on $\tau_{\text{nn}'}$, the flight time distribution averages $\langle t_f \rangle_{t_s}$ and $\langle t_f^2 \rangle_{t_s}$ are needed as additional input. A better determination than the one from the kinetic gas theory argument given above was obtained by Monte Carlo calculations using Geant4UCN [63] (see Fig. 6.6). The parameters of the simulation (mainly material properties, such as Fermi pseudo-potential, loss probability per wall collision, and fraction of diffuse to specular reflection) have been tuned to reproduce measurements of the UCN beam energy spectrum and filling, storage, and emptying time curves of the apparatus. Excellent agreement with the measured observables is obtained, which justifies the extraction of the required flight time distributions. The averages are given in Table 6.2. The assigned systematic uncertainties were derived by varying the material parameters of the simulation, the largest influence coming from the loss probabilities per wall collision.
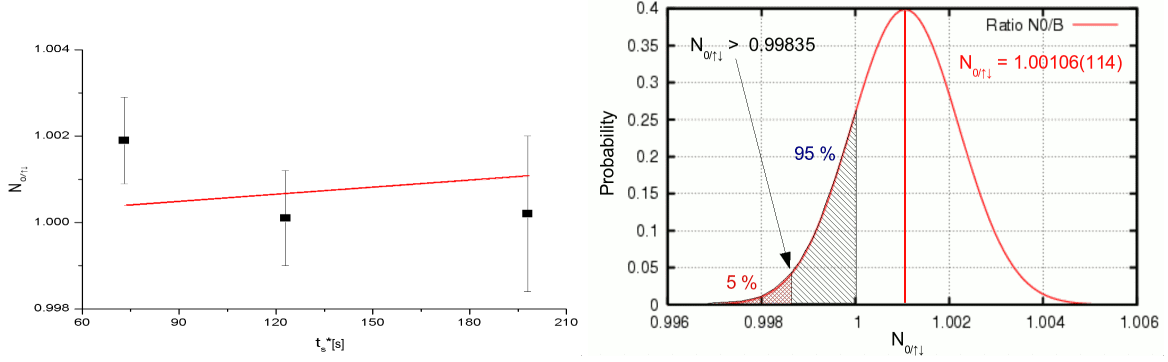
Figure 6.5: On the left, individual results for $N_{0/\uparrow\downarrow}$ are fitted with an exponent $\exp[a\,t_s*]$ (see the text for the fit parameters values). The function obtained is used to calculate $N_{0/\uparrow\downarrow}$ at the limit of the validity range, $N_{0/\uparrow\downarrow}(t_s^* = 198\,\mathrm{s}) = 1.00106(114)$. Finally, as the values greater than one are recognized as unphysical, the corresponding part of the probability distribution is disregarded and the rest is used to extract the 95%C.L. limit.
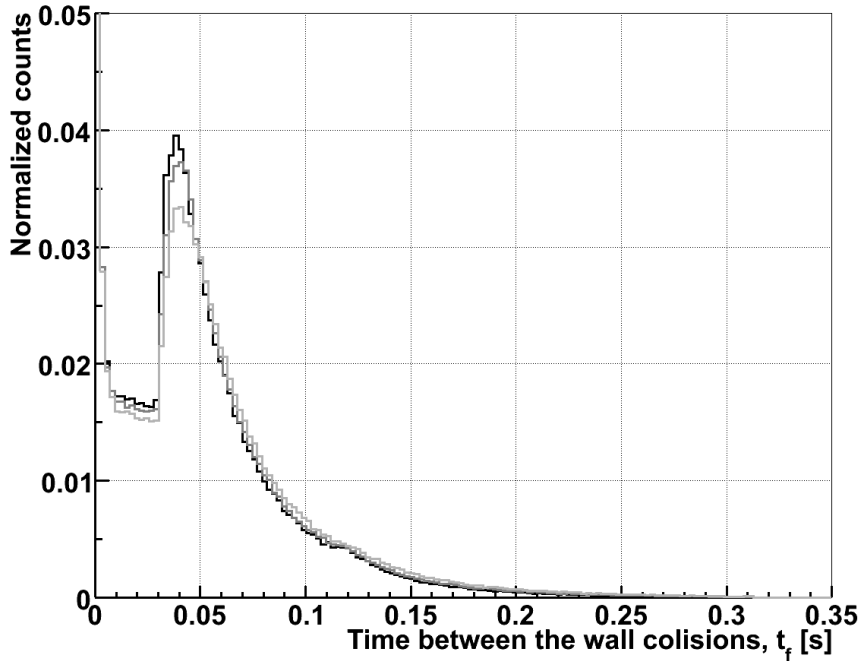
Figure 6.6: Simulated distributions of the time between wall collisions, t_f, for the relevant storage periods: 50 s (black), 100 s (dark grey) and 175 s (light grey).

6.4   Discussion and outlook

The limit on the oscillation time is obtained using the limit on lost neutrons, Eq. 6.10, and the average free flight time values (at $t_s = 175\,\mathrm{s}$, from Table 6.2) in Eq. 6.8 and solving for $\tau_{\mathrm{nn}'}$. The systematic uncertainties are taken into account for the limit

$t_s\,[\mathrm{s}]$	50	100	175
$\langle t_f \rangle_{t_s}\,[\mathrm{s}]$	0.0498(5)	0.0515(5)	0.0543(5)
$\langle t_f^2 \rangle_{t_s}\,[\mathrm{s}^2]$	0.00420(8)	0.00450(9)	0.00505(10)

Table 6.2: Results for $\langle t_f \rangle_{t_s}$ and $\langle t_f^2 \rangle_{t_s}$ using Monte Carlo distributions of flight times between wall collisions. Variation of parameters in the simulation is used to assign systematic uncertainties (in brackets).

on $\tau_{\mathrm{nn'}}$ by adding (or subtracting) them simultaneously in order for them to weaken the limit, i.e., $\langle t_f \rangle_{t_s} = 0.0548\,\mathrm{s}$, $\langle t_f^2 \rangle_{t_s} = 0.00515\,\mathrm{s}^2$ and $t_s^* = 195\,\mathrm{s}$. With a reminder of the assumptions (negligible mirror magnetic field [143], no conventional strong or electro–magnetic interactions of the mirror neutron n', and degeneracy of n and n' in the gravitational field) we obtain the final result

$$\tau_{\mathrm{nn'}} > 103\,\mathrm{s}\,(95\%\ \mathrm{C.L.})\,. \tag{6.11}$$

Figure 6.7 displays the dependence of $N_{0/\uparrow\downarrow}$ on $\tau_{\mathrm{nn'}}$ (see Eq. 6.8) with the band
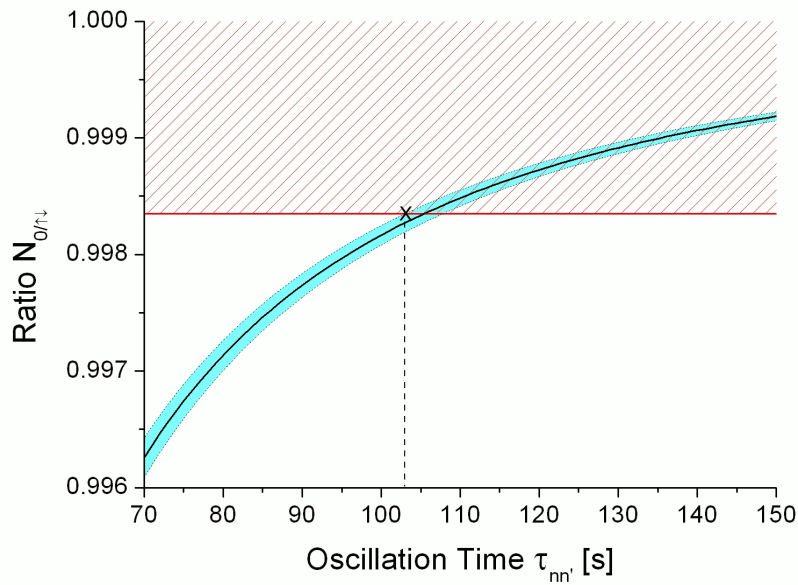
Figure 6.7: The count ratio $N_{0/\uparrow\downarrow}$ as a function of the oscillation time (see Eq. 6.8). The dashed region indicates the allowed region of Eq. 6.10. The error band of the curve displays the systematic uncertainties, see text. The X indicates the point at which the limit on $\tau_{\mathrm{nn'}}$ is evaluated.

indicating the influence of the systematic uncertainties. The 95% confidence limit of Eq. 6.10 is shown and the cross marks the point which determines the limit on the oscillation time. Only a few weeks after the result was published, a second experiment

done with a similar technique (but a 10 times larger storage chamber) reported a limit at 90% confidence level of $\tau_{nn'} > 414\,s$ (90% C.L.) [149].

The result impacts the role nn$'$ oscillations can play in the transport of ultra-high energy cosmic rays over large distances [135, 137], although, it may not completely rule out the nn$'$-explanation for events above the GZK cutoff. A time limit exceeding significantly the neutron lifetime would certainly exclude that possibility, however, it has already lost much of relevance, given the new results on UHCR with no events above the cutoff [140, 141].

Concerning the mirror matter hypothesis, the analysis presented has triggered an interesting discussion. As proposed by Berezhiani [144], the results of the measurement and especially the unexpected tendency to a linear dependency of the number of counts on the magnetic field could be also explained, if confirmed, by the presence of a sufficiently strong (0.03 – 3 G) mirror magnetic field on the Earth. The same effect could be also produced by some other spin-dependent force, distinguishing the neutron and mirror neutron states. Depending on the origin of that field, day-night or yearly variations of the B-field up/down asymmetry of the neutron counts could be expected.

To summarize, there is enough motivation for further experiments of this type. As they are at the moment limited by statistics, the next generation will have to use a more intense UCN source, like the one beeing built at PSI, larger storage volumes and better trap materials (where this work could also contribute).

Chapter 7

Conclusion

The main subject of this thesis was research and development for the neutron electric dipole moment experiment and the search of neutron – mirror neutron oscillations. The activities were mainly focused on search of new materials suitable for the storage of ultracold neutrons (UCN) in these experiments and on a study of their influence on the measurement sensitivity. The most important achievements from this work are:

- The first direct experimental limit on neutron – mirror neutron oscillations, $\tau_{\mathrm{nn'}} > 103\,\mathrm{s}$ (95% C.L.), improving by two orders of magnitude the existing indirect limit (Chapter 6). The limit can still be improved in the future using the same technique and can possibly take advantage of the new materials investigated in this thesis.

- A measurement of the Fermi potentials of deuterated polystyrene ($161\pm10\,\mathrm{neV}$) and deuterated polyethylene ($214\pm10\,\mathrm{neV}$), being the first such measurement for the latter material. The results are in agreement with theoretical predictions and the existing measurement for DPS.

- Production and succesful tests of a new DPS-coated insulator wall for the nEDM storage chamber. The $5\,\mu\mathrm{m}$ thin coating was deposited using a new technique on a suitable material selected (Rexolite). The tests performed prove that the new insulator is comparable with the existing quartz insulator in terms of high-voltage and co-magnetometer performance, but is capable of storing up to 80% more neutrons after a typical storage interval, due to its higher Fermi potential.

- Adjusting the spincoating technique for deposition of $\sim 80\,\mathrm{nm}$ thin optical quality DPE coatings on quartz windows. Such windows can be used as optical windows for the nEDM storage chamber, which are necessary for the operation of the $^{199}\mathrm{Hg}$ vapor co-magnetometer. The coating quality was examined and the final product was succesfully tested in experimental conditions.

- Development of a detailed GEANT4-UCN model of the nEDM apparatus and using it to reproduce the experimental data. The model, validated in this way, was employed to obtain UCN intensity predictions for the existing nEDM

setup located at the new UCN source at PSI. The geometry of the setup and the material selection was studied and optimized. The results indicate the possibility of getting ∼20 times more neutron counts after moving the apparatus from ILL to PSI. Another factor of about 1.5 will be gained, when a material with a Fermi potential similar to DPS is used instead of quartz (which has been used up to now). That conclusion significantly affected strategical planning of the project.

- Calculation of the electric field configuration in the storage chamber. Two and three dimensional field models produced with finite elements software, were used to investigate systematic effects related with high-voltage. The first order motional v×E effect, studied in more detail was proven not to be dangerous on the present sensitivity level.

- As a by product of our attempts to obtain highly resistive HFCVD diamond coatings for UCN storage applications, the existence of a conductive interlayer between the coating and a number of tested substrates was discovered, so far not mentioned explicitly in the literature. Although, the exact reasons for the conductance were not identified, there are some clues indicating that amorphous carbon phases built-up in the bottom part of the coating might be responsible for the observed phenomena.

The new DPS-coated insulator for the nEDM apparatus is already used on a regular basis and it is also planned to use it at least in the first physics run of the experiment at PSI. Nevertheless, the future might belong to other materials, especially to DPE, which had not been used for the UCN storage applications before this work, despite its very promising properties.

Certain parts of this thesis like the neutron – mirror neutron oscillation search [150], the measurement of the Fermi potential of DPE [151] or the simulated intensity predictions for the nEDM measurements at PSI [152] have been published or will be published in the very near future.

Appendix A

4-point resistance measurement method

The most reliable way to measure electrical resistance is to use a 4-terminal method in one of its variants. In this type of measurements, a known current I is injected by electrode 1 and collected at electrode 4, while the potential difference ΔV between
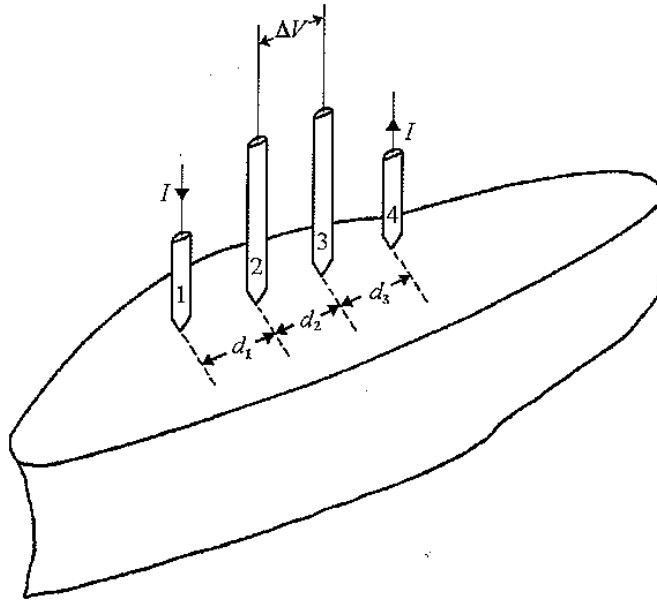
Figure A.1: A typical 4-point resistivity probe.

electrodes 2 and 3 is measured, as shown in Fig. A.1. Laplace's equation can be employed to derive a proper formula for this arrangement, since there is a strict analogy between the field equations of current flow and those of of electrostatic charges, thus

$$\frac{\partial^2 V}{\partial x^2} + \frac{\partial^2 V}{\partial y^2} + \frac{\partial^2 V}{\partial z^2} = 0, \tag{A.1}$$

where V is the electrical potential. Electrodes, which inject or drain current correspond to positive and negative charges respectively, hence a potential at a distance

r from a point electrode supplying a current I inside a material is given by

$$V = \frac{I\rho}{4\pi r}. \tag{A.2}$$

Using that solution one can obtain the net potentials at electrodes 2 and 3 due to the current electrodes on the semi-infinite block

$$\Delta V = \frac{I\rho}{2\pi} \left(\frac{1}{d_1} - \frac{1}{d_2 + d_3} - \frac{1}{d_1 + d_2} + \frac{1}{d_3} \right), \tag{A.3}$$

which can be simplified if equispaced distance d is assumed

$$\Delta V = \frac{I\rho}{2\pi d}. \tag{A.4}$$

As it can be seen from Eq. A.4, the great advantage of 4-point methods is that the result becomes independent of the electrode contact area if only the size of the contacts is much smaller than the inter-electrode spacing. What is still missing in the formula is an additional correction factor, which would take into account finite boundaries of a specimen. Fortunately, factors for different geometries are tabulated in the literature (e.g. in [153]) and for the most interesting case, where the conductive sheet thickness t is much smaller than the electrode spacing d, the expression reduces to

$$\Delta V = \frac{I\rho \ln 2}{\pi t} = \frac{I\rho_s \ln 2}{\pi}. \tag{A.5}$$

The most general of all 4-point techniques was proposed by van der Pauw [154] and allows to work with anisotropic samples of arbitrary shape and to obtain independent components of the resistivity tensor. The method utilizes a sample with electrodes attached to the corners. Measuring the voltage/current ratios for opposite pairs of electrodes,

$$R_1 = V_{12}/I_{34} \text{ and } R_2 = V_{23}/I_{41}, \tag{A.6}$$

directly gives the resistivity value

$$\rho = \frac{\pi t}{\ln 2} \frac{R_1 + R_2}{2} f \left[\frac{R_1}{R_2} \right], \tag{A.7}$$

where f is a tabulated function (see [154, 155]). If the sample is isotropic and is in the form of a square with electrodes attached in the corners, the formula simplifies to

$$\rho = \frac{\pi t}{\ln 2} \frac{R_1}{2}. \tag{A.8}$$

4-point measurements are very reliable and stable, unfortunately for highly resistive materials the point contacts become incapable of injecting currents high enough to create sufficient ΔV. To make it even worse, the necessary input resistance of the voltmeter must be greater than the resistance between the points 2 and 3, otherwise the current would simply bypass the specimen via the voltmeter.
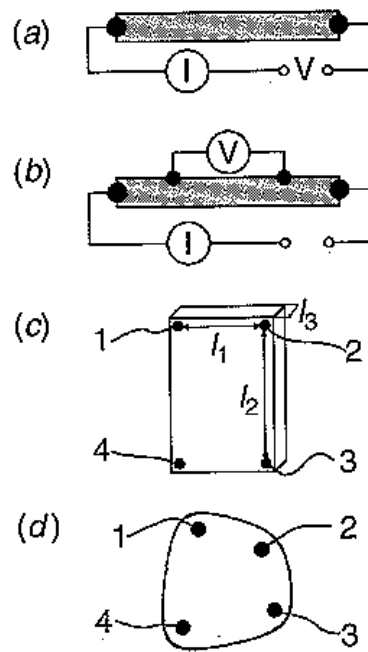
Figure A.2: Electrode configurations for resistivity measurements (c) 4-terminal Montgomery and (d) 4-terminal van der Pauw.

Bibliography

[1] UCN Homepage.
URL `http://ucn.web.psi.ch`

[2] A. Steyerl *et al.*, A new source of cold and ultracold neutrons, Phys. Lett. A 116 (1986) 347.

[3] R. Picker, I. Altarev, J. Bröcker, E. Gutsmiedl, J. Hartmann, A. Müller, S. Paul, W. Schott, U. Trinks, O. Zimmer, A superconducting magnetic UCN trap for precise neutron lifetime measurements, J. Res. Natl. Inst. Stand. Technol. 110 (2005) 357–360.

[4] nTRV Homepage.
URL `http://www.if.uj.edu.pl/ZFJ/nTRV`

[5] A. Knecht, private communication (2008).

[6] B. C. Regan, E. D. Commins, C. J. Schmidt, D. DeMille, New limit on the electron electric dipole moment, Phys. Rev. Lett. 88 (2002) 071805.

[7] R. McNabb, An improved limit on the electric dipole moment of the muon, in: Proceedings of the XXXIX Rencontres de Moriond, Electroweak Interactions and Unified Theories, 2004.
URL `http://arxiv.org/abs/hep-ex/0407008`

[8] W.-M. Yao *et al.*, J. Phys. G 33 (2006) 1.

[9] M. V. Romalis, W. C. Griffith, J. P. Jacobs, E. N. Fortson, New limit on the permanent electric dipole moment of ^{199}Hg, Phys. Rev. Lett. 86 (12) (2001) 2505.

[10] J. Schwinger, Phys. Rev. Lett. 91 (1951) 713.

[11] J. H. Christenson, J. W. Cronin, W. L. Fitch, R. Turlay, Phys. Rev. Lett 13 (1964) 138.

[12] A. D. Sakharov, Violation of CP Symmetry, C-Asymmetry and Baryon Asymmetry of the Universe, JETP Lett. 5 (1967) 24.

[13] R. D. Peccei, H. R. Quinn, CP conservation in the presence of pesudoparticles, Phys. Rev. Lett. 38 (1977) 1440.

[14] C. A. Baker *et al.*, An improved experimental limit on the electric-dipole moment of the neutron, Phys. Rev. Lett. 97 (2006) 131801.

[15] S. Dar, The neutron EDM in the SM: A review, arXiv:hep-ph/0008248v2 (2000).
URL http://arxiv.org/abs/hep-ph/0008248

[16] S. Abel, S. Khalil, O. Lebedev, Nucl. Phys. B 606 (2001) 151–182.

[17] T. Falk, K. A. Olive, M. Pospelov, R. Roiban, Nucl. Phys. B 560 (1999) 3.

[18] M. Pospelov, A. Ritz, Electric dipole moments as probes of new physics, Annals Phys. 318 (2005) 119.

[19] E. M. Purcell, N. F. Ramsey, Phys. Rev. 78 (1950) 807.

[20] J. H. Smith, E. M. Purcell, N. F. Ramsey, Phys. Rev. 108 (1957) 120.

[21] C. G. Shull, R. Nathans, Phys. Rev. Lett. 19 (1967) 384.

[22] V. V. Fedorov, I. A. Kuznetsov, E. G. Lapin, S. Yu. Semenikhin, V. V. Voronin, Neutron spin optics in a noncentrosymmetric crystals as a way for nEDM search. New experimental results., Physica B 385-386 (2) (2006) 1216–1218.

[23] W. B. Dress *et al.*, Phys. Rev. D 15 (1977) 9.

[24] F. L. Shapiro, Usp. Fiz. Nauk. 95 (1968) 145.

[25] I. S. Altarev *et al.*, New measurement of the electric dipole moment of the neutron, Phys. Lett. B 276 (1992) 242.

[26] I. S. Altarev *et al.*, Search for the neutron electric dipole moment, Physics of Atomic Nuclei 59 (7) (1996) 1152–1170.

[27] K. F. Smith *et al.*, A search for the electric dipole moment of the neutron, Phys. Lett. B 234 (1,2) (1990) 191–196.

[28] J. M. Pendelbury *et al.*, Geometric-phase-induced false electric dipole moment signals for particles in traps, Phys. Rev. A 70 (2004) 032102.

[29] Cryogenic nEDM experiment.
URL http://minostux.maps.sussex.ac.uk/~nedm/cryo/cryo1.htm

[30] SNS nEDM experiment.
URL http://p25ext.lanl.gov/edm/edm.html

[31] PNPI/ILL nEDM experiment.
URL http://nrd.pnpi.spb.ru/LabSereb/neutronedm.htm

[32] nEDM Homepage.
URL http://nedm.web.psi.ch

[33] RAL/Sussex/ILL Collaboration Homepage.
URL `http://minoserv.maps.susx.ac.uk/~nedm/index.htm`

[34] T. D. Lee, C. N. Yang, Question of parity conservation in weak interactions, Phys. Rev. 104 (1956) 254.

[35] I. Yu. Kobzarev, L. B. Okun, I. Ya. Pomeranchuk, On the possibility of experimental observation of mirror particles, Sov. J. Nucl. Phys. 3 (1966) 837.

[36] R. Foot, H. Lew, R. R. Volkas, A model with fundamental improper spacetime symmetries, Phys. Lett. B 272 (1991) 67.

[37] Z. Berezhiani, Mirror world and its cosmological consequences, Int. J. Mod. Phys. A 19 (2004) 3775.

[38] L. B. Okun, Mirror particles and mirror matter: 50 years of speculation and search, arXiv:hep-ph/0606202 (2006).

[39] S. I. Blinnikov, M. Yu. Khlopov, Possible manifestations of mirror particles, Sov. J. Nucl. Phys. 36 (1982) 472.

[40] R. Foot, Mirror matter-type dark matter, Int. J. Mod. Phys. D 13 (2004) 2161.

[41] Z. Berezhiani, P. Ciarcelluti, D. Comelli, F. L. Villante, Structure formation with mirror dark matter: Cmb and lss, Int. J. Mod. Phys. D 14 (2005) 107.

[42] R. Foot, Experimental implications of mirror matter-type dark matter, Int. J. Mod. Phys. A 19 (2004) 3807.

[43] R. Foot, Generalized mirror matter models, Phys. Lett. B 632 (2006) 467.

[44] A. Badertscher, P. Crivelli, W. Fetscher, U. Gendotti, S. N. Gninenko, V. Postoev, A. Rubbia, V. Samoylenko, D. Sillou, Improved limit on invisible decays of positronium, Phys. Rev. D 75 (2006) 032004.

[45] R. Foot, R. R. Volkas, A mirror world explanation for the pioneer spacecraft anomalies?, Phys. Lett. B 517 (2001) 13–17.

[46] R. Foot, T. L. Yoon, Exotic meteoritic phenomena: the Tunguska event and anomalous low altitude fireballs — manifestations of the mirror world?, Acta Phys. Pol. B 33 (2002) 1979–2009.

[47] R. Foot, Have mirror stars been observed?, Phys. Lett. B 452 (1999) 83–86.

[48] R. Foot, Have mirror planets been observed?, Phys. Lett. B 471 (1999) 191–194.

[49] R. N. Mohapatra, S. Nasri, S. Nussinov, Some implications of neutron mirror neutron oscillation, Phys. Lett. B 627 (2005) 124.

[50] CODATA recommended values, http://physics.nist.gov/cuu/Constants/index.html (2006).

[51] R. Golub, D. J. Richardson, S. K. Lamoreaux, Ultra Cold Neutrons, Adam Hilger, 1991.

[52] P. Fierlinger, Losses and depolarization of stored ultracold neutrons on diamond-like carbon, Ph.D. thesis, Universität Zürich (2005).

[53] E. Korobkina, R. Golub, J. Butterworth, P. Geltenbort, S. Arzumanov, Temperature dependence of ultracold neutron loss rates, Phys. Rev. B 70 (2004) 035409.

[54] K. Green, P. G. Harris, P. Iaydjiev, D. J. R. May, J. M. Pendlebury, K. F. Smith, M. van der Grinten, P. Geltenbort, S. Ivanov, Performance of an atomic mercury magnetometer in the neutron EDM experiment, Nucl. Instr. Meth. A 404 (1998) 381.

[55] D. J. R. May, A high precision comparison of the gyromagnetic ratios of the ^{199}Hg atom and the neutron, Ph.D. thesis, The University of Sussex (September 1998).

[56] M. Meier, private communication (2008).

[57] D. Dubbers, Simple formula for multiple mu-metal shields, Nucl. Instr. Meth. A 243 (1986) 511.

[58] K. Kirch, private communication (2007).

[59] P. G. Harris, The neutron EDM experiment, arXiv:0709.3100 [hep-ex] (2007). URL http://arxiv.org/abs/0709.3100

[60] Y. Chibane, A new magnetometer for the neutron EDM experiment, Ph.D. thesis, The University of Sussex (September 1990).

[61] K. Green, P. G. Harris, P. Iaydjiev, D. J. R. May, J. M. Pendlebury, K. F. Smith, M. van der Grinten, P. Geltenbort, S. Ivanov, Performance of an atomic mercury magnetometer in the neutron EDM experiment, Nucl. Instr. Meth. A 404 (1998) 381.

[62] S. Agostinelli *et al.*, Geant4 – a simulation toolkit, Nucl. Instr. and Meth. A 506 (2003) 250–303.

[63] F. Atchison, T. Bryś, M. Daum, P. Fierlinger, A. Fomin, R. Henneck, K. Kirch, M. Kuźniak, A. Pichlmaier, The simulation of ultracold neutron experiments using GEANT4, Nucl. Instr. and Meth. A 552 (2005) 513–521.

[64] Merlin Cluster Homepage. URL http://ait.web.psi.ch/services/linux/hpc/merlin/

[65] G. Rogel, Ph.D. thesis, in preparation.

[66] G. Zsigmond *et al.*, Numerical studies of the ucn-flux from the spallation ultra-cold neutron source at psi and phase space transformation of ultra-cold neutrons, in: ICANS-XVII, 2006, p. 168, lA-UR-06-3904.

[67] A. Serebrov, M. Lasakov, A. Fomin, P. Geltenbort, A. Murashkin, I. Krasnoshekova, Yu. Rudnev, A. Vasiliev, Superconducting UCN polarizer for a new EDM spectrometer, Nucl. Instr. and Meth. A 545 (2005) 490.

[68] I. B. Kriplovich, S. K. Lamoreaux, CP Violation Without Strangeness, Springer, 1997.

[69] E. Aleksandrov *et al.*, Proposal for an experimental program at psi: A new precision measurement of the neutron electric dipole moment (EDM), PSI proposal, r-00.05.2 (2002).

[70] R. Golub, Model high-voltage system for apparatus to search for the electric dipole moment of the neutron with the aid of ultracold neutrons, Zh. Tekh. Fiz. 56 (1986) 1592.

[71] V. Y. Ushakov, Insulation of High-Voltage Equipment, Springer, 2004.

[72] A. S. Pillai, R. Hackam, Influence of metal-insulator junction on surface flashover in vacuum, J. Appl. Phys. 61 (11) (1987) 4992–4999.

[73] M. Herrmann, private communication.
URL http://www.ikts.fraunhofer.de

[74] R. E. LaPointe, Physical and electrical properties of plastics, available online.
URL http://members.tm.net/lapointe/Main.html

[75] A. R. Blythe, D. Bloor, Electrical Properties of Polymers, 2nd Edition, Cambridge University Press, 2005.

[76] Low level measurements handbook, Keithley Instruments, Inc. (2004).

[77] Keithley Instruments, Inc., Cleveland, Ohio, USA, Model 6487 Picoammeter/Voltage Source Reference Manual, a Edition (November 2002).
URL http://www.keithley.ch/data?asset=11843

[78] L. Alston (Ed.), High-voltage technology, Oxford University Press, 1968.

[79] R. Henneck, private communication (2006).

[80] E. Boettger, A. Bluhm, X. Jiang, L. Schäfer, C.-P. Klages, Investigation of the high-field conductivity and dielectric strength of nitrogen containing polycrystalline diamond layers, J. Appl. Phys. 77 (12) (1995) 6332.

[81] T. Matthée, L. Schäfer, A. Schmidt, C.-P. Klages, Insulating diamond coatings on tungsten electrodes, Diamond Relat. Mater. 6 (1997) 293.

[82] H. O. Pierson, Handbook of Carbon, graphite and fullerenes - properties, processing and applications, William Andrew Publishing/Noyes, 2004.

[83] Q. Zhang, S. F. Yoon, J. Ahn, Rusli, Y.-P. Guo, A. T. S. Wee, A. C. H. Huan, The role of nitrogen in the deposition of polycrystalline diamond films, Diamond Relat. Mater. 8 (1998) 215–219.

[84] P. W. May, Diamond thin films: a 21st-century material, Phil. Trans. R. Soc. Lond. A 358 (2000) 473.

[85] H. Liu, D. S. Dandy, Studies on nucleation process in diamond CVD: an overview of recent development, Diamond Relat. Mater. 4 (1995) 1173.

[86] B. Lux, R. Haubner, Nucleation and growth of low pressure diamond, in: R. Clausing, L. Horton, J. Angus, P. Koidl (Eds.), Diamond and diamond-like films and coatings, Plenum Press, New York, 1991, p. 579.

[87] P. Mehta Menon, A. Edwards, C. S. Feigerle, R. W. Shaw, D. W. Coffey, L. Heatherly, R. E. Clausing, L. Robinson, D. C. Glasgow, Filament metal contamination and Raman spectra of hot filament chemical vapour deposited diamond films, Diamond Relat. Mater. 8 (1998) 101.

[88] W. Piekarczyk, S. Prawer, Role of atomic hydrogen in preventing surface reconstruction and sp^2 bond formation during chemical vapour deposition of diamond, Diamond Relat. Mater. 2 (1993) 41.

[89] J. Mort, D. Kuhman, M. Machonkin, M. Morgan, F. Jensen, K. Okumura, Y. M. LeGrice, R. J. Nemanich, Boron doping of diamond thin films, Appl. Phys. Lett. 55 (11) (1989) 1121–1123.

[90] T. H. Borst, O. Weis, Boron-doped homoepitaxial diamond layers: Fabrication, characterization and electronic applications, Phys. Stat. Sol. 154 (1996) 423–444.

[91] K. L. Ma, W. J. Zhang, Y. S. Zou, Y. M. Chong, K. M. Leung, I. Bello, S. T. Lee, Electrical properties of nitrogen incorporated nanocrystalline diamond films, Diamond Relat. Mater. 15 (2005) 626.

[92] J. Zimmer, K. V. Ravi, Aspects of scaling CVD diamond reactors, Diamond. Relat. Mater. 15 (2006) 229.

[93] B. Lunn, D. A. Wright, L. Y. Zhang, Growth of diamond films on spherical surfaces by hot filament CVD, Diamond Relat. Mater. 7 (1998) 129.

[94] M. Höfer, L. Schäfer, private communication.
URL http://www.ist.fraunhofer.de/

[95] H. Buchkremer-Hermanns, H. Ren, G. Kohlschein, H. Weiß, Nucleation and early growth of CVD diamond on silicon nitride, Surf. Coat. Technol. 98 (1998) 1038.

[96] I. Endler, A. Leonhardt, H.-J. Scheibe, R. Born, Interlayer for diamond deposition on tool materials, Diamond Relat. Mater. 5 (1996) 299–303.

[97] K. Mallika, R. Komanduri, Low pressure microwave plasma assisted chemical vapor deposition (MPCVD) of diamond coatings on silicon nitride cutting tools, Thin Solid Films 396 (2001) 145.

[98] R. T. Rozbicki, V. K. Sarin, Nucleation and growth of combustion flame deposited diamond on silicon nitride, Int. J. Refract. Met. Hard Mater. 16 (1998) 377.

[99] A. Afzal, C. A. Rego, W. Ahmed, R. I. Cherry, HFCVD diamond grown with nitrogen added: film characterization and gas-phase composition studies, Diamond Relat. Mater. 7 (1998) 1033–1038.

[100] A. J. Eccles, T. A. Steele, A. Afzal, C. A. Rego, W. Ahmed, P. W. May, S. M. Leeds, Influence of B- and N-doping levels on the quality and morphology of CVD diamond, Thin Solid Films 343-344 (1999) 627–631.

[101] M. Hermann, A. Bales, Herstellen von Substraten füer Diamantbeschichtung der Werkstoffe $MgAl_2O_4$, $Y_3Al_5O_{12}$, Y_2SiO_5, angebot-Nr.: 64/621/06/01, unpublished (2005).

[102] C. W. Bale, P. Chartrand, S. A. Degterov, G. Eriksson, K. Hack, R. Ben Mahfoud, J. Melançon, A. D. Pelton, S. Petersen, FactSage thermochemical software and databases, Calphad 26 (2) (2002) 189.

[103] K. Kimura, K. Nakajima, S. Yamanaka, M. Hasegawa, H. Okushi, Hydrogen depth-profiling in chemical-vapor-deposited diamond films by high-resolution elastic recoil detection, Appl. Phys. Lett. 78 (12) (2001) 1679.

[104] F. Atchison, B. Blau, M. Daum, P. Fierlinger, P. Geltenbort, R. Henneck, S. Heule, M. Kasprzak, K. Kirch, K. Kohlik, M. Kuźniak, M. Meier, C.-F. Meyer, A. Pichlmaier, C. Plonka, P. Schmidt-Wellenburg, B. Schultrich, T. Stucky, V. Weihnacht, O. Zimmer, Storage of ultracold neutrons in a volume coated with diamond-like carbon, Phys. Rev. C 74 (2006) 055501.

[105] M. Suter, private communication (2005).

[106] G. Chase, Ohms per square what!, ESD Journal.
URL http://www.esdjournal.com/techpapr/ohms.htm

[107] S. Fowler, Ohms per square what?, ESD Journal.
URL http://www.esdjournal.com/techpapr/ohmmtr/ohm.htm

[108] W. Klein, Surface resistance, ESD Journal.
URL http://www.esdjournal.com/techpapr/surface/surface.htm

[109] M. I. Landstrass, K. V. Ravi, Resistivity of chemical vapor deposited diamond films, Appl. Phys. Lett. 55 (10) (1989) 975.

[110] K. Hayashi, S. Yamanaka, H. Okushi, K. Kajimura, Study of the effect of hydrogen on transport properties in chemical vapor deposited diamond films by hall measurements, Appl. Phys. Lett. 68 (3) (1996) 376.

[111] S.-G. Ri, C. Nebel, D. Takeuchi, B. Rezek, N. Tokuda, S. Yamasaki, H. Okushi, Surface conductive layers on (111) diamonds after oxygen treatments, Diamond Relat. Mater. 15 (4-8) (2006) 692–697.

[112] H. Ye, P. Hing, Dielectric behavior of diamond films, Int. J. Thermophys. 22 (4) (2001) 1285.

[113] B. Koslowski, S. Strobel, P. Ziemann, Comment on origin of surface conductivity in diamond, Phys. Rev. Lett. 87 (20) (2001) 209751.

[114] E. Müller, First TEM results (low resolution TEM/STEM), private communication (Oct 2006).

[115] F. Atchison, B. Blau, M. Daum, P. Fierlinger, A. Foelske, P. Geltenbort, M. Gupta, R. Henneck, S. Heule, M. Kasprzak, M. Kuźniak, K. Kirch, M. Meier, A. Pichlmaier, C. Plonka, R. Reiser, B. Theiler, O. Zimmer, G. Zsigmond, Diamondlike carbon can replace beryllium in physics with ultracold neutrons, Phys. Lett. B 642 (2006) 24–27.

[116] M. G. D. van der Grinten, J. M. Pendlebury, D. Shiers, C. A. Baker, Characterization and development pf diamond-like carbon coatings for storing ultracold neutrons, Nucl. Instr. and Meth. A 423 (1999) 421.

[117] E. Findeisen, Hydrogen concentration and mass density of diamondlike carbon films obtained by x-ray and neutron reflectivity, J. Appl. Phys. 76 (1994) 4636.

[118] F. Atchison, B. Blau, M. Daum, P. Fierlinger, P. Geltenbort, M. Gupta, R. Henneck, S. Heule, M. Kasprzak, A. Knecht, M. Kuźniak, K. Kirch, M. Meier, A. Pichlmaier, R. Reiser, B. Theiler, O. Zimmer, G. Zsigmond, Measurement of the Fermi potential of diamond-like carbon and other materials, Nucl. Instr. and Meth. B 260 (2007) 647.

[119] F. Atchison, T. Bryś, M. Daum, P. Fierlinger, A. Foelske, M. Gupta, R. Henneck, S. Heule, M. Kasprzak, K. Kirch, R. Kötz, M. Kuźniak, T. Lippert, C. F. Meyer, F. Nolting, A. Pichlmaier, D. Schneider, B. Schultrich, P. Siemroth, U. Straumann, Structural characterization of diamond-like carbon films for ultracold neutron applications, Diamond Relat. Mater. 16 (2007) 334.

[120] Narziss, http://kur.web.psi.ch/narziss, SINQ (PSI).

[121] L. Parrat, Surface studies of solids by total reflection of x-rays, Phys. Rev. 95 (1954) 359.

[122] P. A. Kienzle, K. V. O'Donovan, J. F. Ankner, N. F. Berk, C. F. Majkrzak, http://www.ncnr.nist.gov/reflpak (2002-2006).

[123] MIDAS Homepage.
URL https://midas.psi.ch/

[124] K. Sławińska, private communication.

[125] B. Gross, private communication (2007).

[126] R. Henneck, M. Kuźniak, nEDM 'polystyrene' insulator: preparation and quality assurance, 2nd try (Nov 2007).

[127] S. K. Lamoreaux, Deuterated polystyrene - synthesis and uses for ultracold neutron bottles and the neutron EDM experiment, ILL Experimental Report, iLL88LA1T (1988).

[128] D. N. McKinsey, Time dependence of liquid-helium fluorescence, Phys. Rev. A 67 (2003) 062716.

[129] C. J. Lawrence, The mechanics of spin coating of polymer films, Phys. Fluids 31 (10) (1988) 2786.

[130] O. Mellbring, S. K. Øiseth, A. Krozer, J. Lausmaa, T. Hjertberg, Spin coating and characterization of thin high-density polyethylene films, Macromolecules 34 (7496-7503).

[131] A. C. Wirtz, M. Dokter, C. Hofmann, E. J. J. Groenen, Spincoated polyethylene films for single-molecule optics, Chem. Phys. Lett. 417 (2006) 383–388.

[132] F. A. Bettelheim, R. S. Stein, On the birefringence of polyethylene films, J. Polym. Sci. 27 (1958) 7496–7503.

[133] S. Heule, Production, characterization and reflectivity measurements of diamond-like carbon and other ultracold neutron guide materials, Ph.D. thesis, Universität Zürich (2008).

[134] J. M. Pendlebury, private communication (2005).

[135] Z. Berezhiani, L. Bento, Neutron-mirror-neutron oscillations: How fast might they be?, Phys. Rev. Lett. 96 (2006) 081801.

[136] M. Baldo-Ceolin et al., A new experimental limit on neutron-antineutron oscillations, Z. Phys. C 63 (1994) 409.

[137] Z. Berezhiani, L. Bento, Fast neutron-mirror neutron oscillation and ultra high energy cosmic rays, Phys. Lett. B 635 (2006) 253.

[138] K. Greisen, Phys. Rev. Lett. 16 (1966) 748.

[139] G. T. Zatsepin, V. A. Kuzmin, JETP Lett. 4 (1966) 78.

[140] T. Yamamoto et al., The UHECR spectrum measured at the Pierre Auger Observatory and its astrophysical implications, arXiv:0707.2638 (2007).

[141] D. R. Bergmann *et al.*, Observation of the GZK cutoff using the HiRes detector, Nucl. Phys. B Proc. Suppl. 165 (2007) 19.

[142] Yu. N. Pokotilovski, On the experimental search for neutron → mirror neutron oscillations, Phys. Lett. B 639 (2006) 214.

[143] A. Yu. Ignatiev, R. R. Volkas, Geophysical constraints on mirror matter within the earth, Phys. Rev. D 62 (2000) 023508.

[144] Z. Berezhiani, More about neutron - mirror neutron oscillation, arXiv:0804.2088 (2008).

[145] C. Cohen-Tannoudji, B. Diu, F. Laloë, Quantum mechanics (1977).

[146] R. N. Mohapatra, R. E. Marshak, Phenomenology of neutron oscillations, Phys. Lett. B 94 (1980) 183.

[147] V. K. Ignatovich, The Physics of Ultracold Neutrons, Clarendon Press, Oxford, 1990.

[148] P. G. Harris *et al.*, New experimental limit on the electric dipole moment of the neutron, Phys. Rev. Lett. 82 (1999) 904.

[149] A. P. Serebrov *et al.*, Experimental search for neutron–mirror neutron oscillations using storage of ultracold neutrons, Phys. Lett. B 663 (3) (2008) 181–185, arXiv:0706.3600.

[150] G. Ban, K. Bodek, M. Daum, R. Henneck, S. Heule, M. Kasprzak, N. Khomutov, K. Kirch, S. Kistryn, A. Knecht, P. Knowles, M. Kuźniak, T. Lefort, A. Mtschedlishvili, O. Navillat-Cuncic, C. Plonka, G. Quéméner, M. Rebetez, D. Rebreyend, S. Roccia, G. Rogel, M. Tur, A. Weis, J. Zejma, G. Zsigmond, Direct experimental limit on neutron – mirror neutron oscillations, Phys. Rev. Lett. 99 (2007) 161603.

[151] K. Bodek, M. Daum, R. Henneck, S. Heule, M. Kasprzak, K. Kirch, A. Knecht, M. Kuźniak, B. Lauss, M. Meier, G. Petzoldt, M. Schneider, G. Zsigmond, Storage of ultracold neutrons in high-resistivity, non-magnetic materials with high Fermi potential, Nucl. Instr. and Meth. A, doi:10.1016/j.nima.2008.09.018 (2008).

[152] M. Kuźniak *et al.*, An improved neutron electric dipole experiment, in: Flavor Physics and CP Violation Conference, Taipei, 2008, arXiv:0806.4837.

[153] F. M. Smiths, Measurement of sheet resistivities with the four-point probe, The Bell System Technical Journal (1958) 711.

[154] L. J. van der Pauw, A method of measuring the resistivity and Hall coefficient on lamellae of arbitrary shape, Philips Technical Review 20 (8) (1958/59) 220–224.

[155] L. J. van der Pauw, Philips Res. Repts. 16 (1961) 187.

Index

Acknowledgements